Towards strong coupling of strontium to a miniature ring cavity

Torben Pöpplau

Thèse de Doctorat
de la Sorbonne Université

réalisée au

Laboratoire Kastler Brossel
de l'École Normale Supérieure

Spécialité : Physique quantique
École doctorale : «Physique en Île-de-France »

Présentée par
Torben Hendrik Johann PÖPPLAU
né à *Berlin-Neukölln*

Pour obtenir le grade de docteur de la Sorbonne Université

Towards strong coupling of strontium to a miniature ring cavity

Soutenue le 12 décembre 2019
devant le jury composé de:

M.	Philippe Wilhelm Courteille	Rapporteur
M.	Jan Westenkær Thomsen	Rapporteur
M.	Sébastien Bize	Examinateur
M^{me}	Isabelle Bouchoule	Examinatrice
M.	Marc Cheneau	Examinateur
M.	Jakob Reichel	Directeur de thèse

Contents

Prologue IV

1 Introduction to strontium in the context of cavity QED 1
1.1 Brief introduction to the atom-cavity interaction 1
1.1.1 Coupling of a single atom to a cavity mode 1
1.1.2 An open atom-cavity system 3
1.2 Coupling an atomic ensemble to a cavity 4
1.2.1 Joint measurement of the internal state of atoms in a cavity . . 8
1.3 Ultra-cold strontium for precision measurements 11
1.3.1 Physical-chemical properties 11
1.3.2 Stark effect and light-shift 13
1.3.3 On the interest of using strontium for cQED 14
1.4 Guidelines for a new cQED experiment with strontium 17

2 A new strontium apparatus for cavity QED in a ring cavity 19
2.1 The vacuum system 19
2.2 The strontium effusive source 22
2.2.1 Basic kinetic gas theory 23
2.2.2 Terminology of effusive sources 25
2.2.3 Design of a new strontium oven 26
2.3 Optical access and magnetic quadrupole fields 30
2.3.1 Magnetic coil design 30
2.3.2 Zeeman slowing 32
2.4 The strontium laser system 35
2.4.1 The first MOT stage 35
2.4.2 The second MOT stage and clock laser system 37
2.5 RAM suppression by 3ω PDH demodulation 39
2.5.1 Pound-Drever-Hall stabilization 40
2.5.2 Residual Amplitude Modulation (RAM) 43
2.5.3 Third-harmonic demodulation technique 44
2.6 Conclusion 47

3 Fabrication of CO_2 machined cavities for cold atom experiments . . 51
3.1 Interaction principles of CO_2 lasers with fused silica 52

3.2 Experimental setup for laser beam machining . . . 54
3.2.1 Single-shot dot milling on fused silica . . . 54
3.2.2 Multi-shot fabrication . . . 55
3.2.3 The substrate holders . . . 57
3.3 Laser polishing of fused silica surfaces . . . 59
3.3.1 Substrate preparation . . . 59
3.3.2 Polishing procedure . . . 60
3.4 Machining large spherical structures via laser dot milling . . . 63
3.4.1 Technical challenges of the dot milling technique . . . 63
3.4.2 Fiber results . . . 65
3.5 Potential estimation of convolutional neural networks for a faster pattern optimization in the context of CO_2 mirror fabrication . . . 67
3.5.1 Designing a convolutional neural network . . . 69
3.5.2 Learning with CO_2-machined structures . . . 72
3.6 Integrated mode-matching for open fiber cavities . . . 75
3.6.1 Graded index fibers . . . 76
3.6.2 Experimental test . . . 78
3.6.3 CO_2 machining of large mirror structures on GRIN fibers . . . 81
3.6.4 Conclusion . . . 82

4 An open, compact ring cavity . . . 85
4.1 Linear optical resonators . . . 86
4.2 The traveling wave (ring) resonator . . . 88
4.2.1 Compensation of astigmatism . . . 89
4.2.2 Frequency spectrum . . . 91
4.3 Requirements on the mirror quality . . . 92
4.3.1 Back-propagating scattered mode . . . 96
4.4 Conception of the upcoming high-finesse ring cavity . . . 98
4.4.1 Design . . . 98
4.4.2 Coating . . . 100
4.5 Estimating the *dc*-Stark shift induced by the piezo electric field . . . 100
4.5.1 Calculation of the electric potential . . . 101
4.5.2 The *dc*-Stark shift of Strontium . . . 103
4.6 Cavity assembly and alignment . . . 103
4.7 First prototype of the ring cavity . . . 105
4.7.1 Results . . . 106
4.8 Conclusion and outlook . . . 109

Conclusion . . . 114

A Gaußian beams and transfer matrices 117
A.1 Gaußian beams 117
A.2 ABCD matrix formalism 118

B Test on blue light induced finesse degradation 121

Personal statement: On the relevance of project management in academic research 126

Bibliography 129

List of Figures

1.1.1 Illustration of an atom-cavity system interacting with its environment. The system's coupling constant is g. The spontaneous emission of the atom in the excited state is defined by the constant Γ and the cavity losses by κ. η represents the effective amplitude of a pump field injected into the cavity mode. . 3

1.2.1 (a) shows a schematic representation of the commonly used rubidium-87 level scheme for CQED. The empty cavity is resonant with the transition $|1\rangle \rightarrow |2\rangle$, the state $|0\rangle$ is not coupled to the cavity. (b) depicts the Vacuum Rabi splitting. The system resonances are displaced by the factor $\sqrt{N}g$ with respect to the resonance of the empty cavity. The width of the peaks is $(\kappa + \Gamma)/2$. (c) shows illustration of the corresponding atom-cavity system with a probe at frequency ω_p. 9

1.2.2 Visualization of the $\chi \hat{J}_z$ term, known as the one-axis-twisting. a) shows an illustration of a coherent and b) of spin-squeezed state on the Bloch sphere (blue). The red blurred ellipse at the atomic state vector's tip indicates the uncertainty region of the transversal spin components. 10

1.3.1 Excerpt from the level scheme of ^{87}Sr 11

1.3.2 Calculated polarizabilities of the $^1S_0$ and a) the $^3P_1$ and b) $^3P_0$ states in atomic units. The dipole matrix elements are derived from [66, 71–81]. 15

1.3.3 Relevant levels of ^{87}Sr for cavity QED. This scheme allows a QND probe of the clock transition $|0\rangle \rightarrow |1\rangle$ by exploiting a far-detuned probe on $|0\rangle \rightarrow |2\rangle$. 16

2.1.1 a) 3D CAD drawing of the vacuum system with the magnetic coils. b) Beampath. c) Photo of the glass cell after the bake-out. . 20

2.2.1 a) Calculated vapor pressure for several elements often used in cold atom experiments. b) Temperature dependent mean free path of strontium. The dashed lines indicate the temperatures at which the mean free path of strontium is on the same order than the first orifice diameter and the orifice length. 24

2.2.2 Calculated strontium velocity distributions at 450 °C for a thermal gas, thermal beam and opaque capillary [101, 102]. The shaded region indicates the fraction of the thermal beam distribution trapped by the Zeeman slower. 25

2.2.3 a) Illustration of the atomic beam trajectory through the three apertures. The six-way cross is removed from the view. Due to some manufacturing problems, aperture 1 is not aligned with the atomic beam axis. b) Detailed CAD illustration of the oven assembly. The thermocouple is not shown in this picture. 27

2.2.4 a) FEM thermal simulation of the oven assembly at an electrical power of 15 W. b) Measurement of the electrical power consumption vs. the oven temperature. The dashed lines show the different heat loss contributions. 29

2.3.1 Shown is the magnetic field for $I = 25\,\mathrm{A}$ per coil. *Top*: Contour plot of the magnetic field in the x-z-plane. Gray circle: MOT trapping region; Green dashed line: atomic jet; Green dots: position of the two apertures. *Bottom:* Cut through the B-field x-axis. 32

2.3.2 a) Ideal shape of a Zeeman slower and calculated magnetic field of the MOT coils for $I = 25\,\mathrm{A}$, $\epsilon = 0.38$ and $\Delta = -2\pi \times 17\gamma$. b) Comparison between the slope of the ideal Zeeman slower and slope of the calculated magnetic field. 34

2.4.1 Simplified scheme of the blue MOT laser system. PM - polarization maintaining fiber; DM - dichroic mirror; ZS - Zeeman slower. 36

2.4.2 Dual-sideband locking scheme. 37

2.5.1 a) Schematic of the Pound-Drever-Hall system for generating an error signal. b) Calculation of the 1ω and 3ω PDH error signals for the ULE cavity specifications presented in section 2.4.2. The curves are offset for visual clarity. 40

2.5.2 a) shows the offset-effect of the RAM on the error signal for 1ω (top) and 3ω (bottom) demodulation for a cavity with $\mathcal{T} = 50\,\mathrm{ppm}$ and $\mathcal{L} = 50\,\mathrm{ppm}$. The dashed lines indicate the in-phase (μ) contribution and the dotted lines the out-of-phase (ν) contribution. b) Suppression of the RAM-induced error signal offset for different mirror losses. 45

2.5.3 The 3ω locking scheme. 46

2.5.4 a) shows the recorded error signal of the $1f$ PDH (*top*) and the $3f$ PDH method (*bottom*) over 14 h, where each data point is an average over 30 s and b) shows the corresponding FN-PSD used for the linewidth measurement of both techniques. 47

2.6.1 Shown are absorption imaging pictures of strontium atoms in a) the blue MOT and b) a early-stage red MOT. 48

3.1.1 a) Absorption coefficient of fused silica (reproduced from [137]). The red dashed lines indicate the common CO_2 laser wavelength at 9.3 µm and 10.6 µm. b) Photodiode signal of the SYNRAD *firestar v20* output power at 70 % duty cycle. The observed power modulation has a frequency of 20 kHz. 52

3.2.1 The CO_2-laser machining setup as described in section 3.2. 55

3.2.2 a) shows a CAD drawing of the fiber holder assembly. b) Photo of the fiber clambs pushing a fiber array into the grooves (after coating) and c) a close-up view of a single v-groove supporting an optical fiber substrate (taken from [149]). 57

3.2.3 The substrate holder. a) shows a photo of the assembled mirror holder with the substrates before sending it for coating. b) is a CAD illustration of the holder assembly. 58

3.3.1 a) Photo of the cut wafer covered with PMMA, taken under an optical microscope. b) Illustration of the basic operational principle of laser polishing. w_L is the beam spot diameter, v_{scan} the scan speed, l_{L} the length and d_{L} the line separation. 60

3.3.2 a) AFM scans of the unpolished wafer (left), a polished substrate with a scan speed of 200 µm s^{-1} (center) and 100 µm s^{-1} (right). b) The azimuthally-averaged PSD of the AFM for v_{scan} =100 µm s^{-1}. The maximum spatial frequency is limited by the Nyquist sampling theorem, $f_{\mathrm{max}} = (2 \times N_{\mathrm{samp}})^{-1} = 4.26\,\mu\mathrm{m}^{-1}$, where $N_{\mathrm{samp}} = 30\,\mu\mathrm{m}/256$ is the spatial resolution of the AFM. 61

3.3.3 Shown are the subtracted profiles of the substrates before and after polishing, a) at too low speed and b) at the optimum speed. The global waviness does not occur anymore. 62

3.4.1 a) The rose-colored arrows represent the pulses of the CO_2 dot milling setup, which deposit heat into the substrate (cyan). The head dissipation (illustrated by the red arrows) is disturbed by presence of first depression which leads to a deeper second structure. If the two consecutive shots are close enough, melted glass flows into the first structure (blue region), which decreases its structure depth by Δd. b) The blue dots are experimental data averaged over five measurement and the dashed line is a $a/x^2 + b/x^6$ fit for visualization purposes. 63

3.4.2 Profilometry pictures for a) low power/long pulse length (1480 mW/25 ms) and b) high power/short pulse length (1830 mW/8 ms). 65

3.4.3 a) The grey circle illustrates the surface of a cleaved fiber and the red dots illustrate the positions of each laser pulse. R is the radius of the ring, α is the angle of the first pulse (green dot) of the ring and JO stands for the jump-over. b) Illustration of the large-diameter annealing shot. 66

3.4.4 a) shows a machined fiber with the corresponding shoot pattern (red dots) and the effective mirror diameter (green circle) and b) depicts the final, optimized shoot pattern. 67

3.4.5 a) Cuts along the x- (blue) and y-axis (orange) of a fiber structure with $\mathrm{ROC_{x/y}} = 269/344\,\mu$m from a single profilometer with the corresponding 2D spherical fit over a circular region with a diameter of 90 µm. The lower plot shows the fit residuals along the cuts. b) Mirror map of the 2D fit residuals. The profile deviations are $\sigma_{\mathrm{mean/RMS}} = 7.7/10.4$ nm. c) Shown is the surface fit residual for different fit diameters. Grey region corresponds to the beam radius on the mirror. 68

3.5.1 Working principle of a CNN algorithm. 69

3.5.2 a) Shown is the training history of the CNN with a R^2-score of nearly 0.7. b) Fabrication results of the fused silica structures. The blue dots represent the initial random dataset that has been used for training. c) Fabrication results of the elliptical fiber structures as used in chapter 4. 73

3.6.1 a) Trajectory of a ray and refractive index distribution of a GI fiber with parabolic index distribution. b) The dashed blue line shows the calculated waist for $p/4 = 1050\,\mu$m and MFD $= 6\,\mu$m of the SM fiber. 77

3.6.2 a) Photo of two CU800/200 SM fibers with a 1100 µm long GRIN pieces (blue squares). b) Corresponding measurement of the excess loss depending on the fiber separation. The red dashed line represents the maximally achievable fiber-to-fiber coupling considering 0.4 dB of reflection at the air-fiber interface and 0.3 dB of splice losses. 79
3.6.3 a) Profilometry picture of a machined GI fiber tip. b) Cuts through the machined structure and the corresponding residuals of a 2D spherical fit. 80
3.6.4 a) The plot shows the mode coupling for different GRIN lenses to a fiber cavity of length $L = 6\,\mathrm{mm}$. The lens with a pitch length of $p = 4 \cdot 1150\,\mu\mathrm{m}$ can realize couplings close to $\eta = 1$. The dashed lines show the same GRIN lenses but taking the lensing effect of the concave structure (ROC = 6 mm) into account. It can be seen that the structure lensing can be compensated by a different lens length. b) Clipping losses for a cavity with $L = R = 6\,\mathrm{mm}$ and a coating transmission of 1000 ppm. The losses are shown for different effective mirror diameters. 81

4.1.1 a) Schematic representation of a Fabry-Perot cavity. b) Stability diagram of optical resonators. 87
4.2.1 a) shows the schematic representation of a ring cavity with equilateral triangle optical path. M_1 is the incoupling mirror. b) Cavity mode waist for a equilateral ring cavity with a branch length $a = 200\,\mu\mathrm{m}$. The red dashed line indicates the design cavity waist of 3.5 µm. 89
4.2.2 Illustration of the astigmatism caused by an off-axis mirror with the ROC R_0, decomposed into tangential and sagittal components represented by cylindrical mirrors. *Left:* The vertical lines represent the contour lines of the mirror's height profile seen by the tangential component of the incident beam. The contour lines of the same height profile are denser in the case of a smaller incident angle α, leading to a smaller ROC. *Right:* Shown is the mirror seen by the sagittal component of the incident beam. The effective area and thus the ROC seen by the beam increases under non-normal incidence. 90
4.2.3 Illustration of the odd-parity phase shift of π. 91
4.3.1 a) clipping losses. b) Local mirror map of the structure presented in subsection 3.4.2. The height residual is averaged over five pixel, corresponding to 1 µm in order to reduce the profilometry noise. . 93

4.3.2 Illustration of the light scattering of the fiber mirror into the back-propagating mode. The scattering hemisphere has s radius of half the cavity length L and spans by unfolding the cavity around the left plane mirror. dA represents the mode waist cross-section on the scattering hemisphere and the color gradient illustrates the cosine scattering distribution. 97

4.4.1 a) CAD draft of the high-finesse cavity assembly. The plane mirrors and the fiber are colored in cyan. Also shown are the piezo (yellow) and the mode-matching aspheric lenses (red). b) True to scale illustration of the ring cavity with the corresponding losses and transmissions of each mirror. 99

4.5.1 Shown are the FEM simulations with a) the top electrode set to 1 V and b) the bottom electrode set to 1 V. The red dot indicates the approximate atom's position. c) Total electric field position of the atoms. 102

4.6.1 a) Gluing guide made from Teflon in order to precisely glue the plane mirrors under an angle of 60°. b) The Alignment setup used to acquire the results presented in this section. 103

4.6.2 Illustration of the pre-alignment procedure as described in the text. 104

4.7.1 a) Photo of the preliminary gold cavity in comparison to a penny. The small, bright red reflection on the substrate is the incoupling beam. b) Zoom onto the cavity via a microscope. 106

4.7.2 Mode spectrum measured of a 570 µm long cavity. The vertical orange lines correspond to the calculated mode spectrum. The cavity was intentionally misaligned to show the higher-order modes. 107

4.7.3 a) Shown are the reconstructed cavity waists in the tangential and sagittal plane based on the measured divergence angles of the output beam for different cavity lengths. The dashed lines indicate the theoretical waists based on the ROCs $R_{\parallel}/R_{\perp} = 351\,\mu\text{m}/260\,\mu\text{m}$. The gray vertical line indicates the concentric limit of the cavity. b) The difference of a well-aligned, non-astigmatic cavity and a misaligned cavity becomes apparent observing the degeneracy of the $\text{TEM}_{02,20}$ modes. 108

4.7.4 a) Polarization shift of a 575 µm long cavity. The polarization-dependent phase shift amounts to 200° and is in good agreement with the theory. b) Measurement of the finesse vs. cavity length for both polarizations. The gray vertical line indicates the concentric limit of the cavity. 109

4.8.1 CAD-illustration of an advanced ring-cavity assembly. The fibers and the penta-prisms are shown in blue and the incoupling-fiber with GRIN-endcaps are colored in red. The photodiode depicted in top-right corner. 110

A.1.1 a) Intensity profile of a Gaußian beam. b) Transverse modes. . . . 117

B.0.1 a) shows the finesse evolving over time with different incident laser powers and b) shows the measurement setup. 121

List of Tables

1.1 Key properties of strontium MOTs. 13

2.1 Oven properties for the calculation of its electrical power intake. A – surface area; L – length; σ – cross section; k – thermal conductivity; ϵ – emissivity. 29
2.2 Characteristics of the *Stable Laser Systems* ULE cavity. 39

4.1 Summary of the intended parameters of the ring cavity. 101

Résumé

L'étude expérimentale d'états intriqués avec un grand nombre d'atomes et de leurs applications constitue l'un des domaines les plus dynamiques de la physique atomique, moléculaire et optique moderne. De nombreuses techniques expérimentales ont émergé au cours des dernières décennies pour étudier des systèmes intriqués. Des atomes froids piégés dans le vide se sont avérés être une technique puissante pour la manipulation de ces systèmes. Parmi la grande variété de dispositifs expérimentaux dans le domaine des atomes froids, le champ de l'électrodynamique quantique en cavité (cQED) permet de produire et contrôler des interactions à longue portée, ainsi que de tomographier des états quantiques via des mesures non-destructives.

Cette thèse rend compte de la conception et de la construction d'un nouveau dispositif expérimental d'atomes froids permettant le refroidissement optique du strontium pour le chargement rapide et fiable d'une cavité miniaturisée. Dans ce but, un système à vide compact comprenant une source d'un jet atomique efficace a été conçu et mis en place. La caractéristique principale de cette nouvelle expérience sera l'intégration d'une cavité en anneau qui permet d'intriquer des ensembles atomiques.

Outre le montage de la nouvelle expérience, un prototype d'une nouvelle génération de résonateurs en anneau a été conçu et étudié expérimentalement au cours de cette thèse. C'est la cavité en anneau la plus compacte et courte à ce jour. En outre, afin de compenser l'astigmatisme intrinsèque des cavités en anneau, une structure de miroir elliptique a été fabriquée sur une pointe de fibre, à l'aide une procédure d'usinage par tirs multiples d'un laser CO_2 focalisé.

Abstract

The exploration of entangled states with large atom numbers and their application represents one of the most dynamic fields of research of contemporary atomic, molecular, and optical physics. Many different experimental techniques have emerged over the past decades to study entangled system. Cold atoms trapped in vacuum have proven to be a powerful venue for the manipulation of such systems. Among the plethora of different experimental platforms, the field of cavity quantum electrodynamics (cQED) provides versatile tools to engineer long-range interactions as well as the possibility to perform tomography of atomic quantum states via non-destructive measurements.

More specifically, this thesis reports on the conception and construction of a new ultracold alkaline-earth atom experiment for the fast and reliable loading of a miniaturized cavity. For this purpose, a compact vacuum system including an efficient atomic beam source were designed and set up. The key feature of this new apparatus will be the integration of an optical ring resonator, which enables the generation of entangled atomic states via atom-light interactions and nondestructive detection of the atomic state.

In addition to the set-up of the new experiment, a prototype of the final ring cavity was studied, demonstrating the shortest open ring cavity to date. Besides its compactness, the cavity compensates for the intrinsic astigmatism of ring cavities. For this purpose, an elliptical mirror structure has been fabricated on a fiber tip using a focused CO_2-laser.

Prologue

One of the most fundamental and important phenomena in physics is the interaction of electromagnetic fields with matter. As the movement of electrons and nuclei, thus the elementary building blocks of atoms, is determined by electromagnetic interactions, it is of great interest to gain a deeper understanding of its mechanism. The electromagnetic interaction also gives rise to atom-atom interactions and to light emission and absorption of atoms and molecules. The light emitted or absorbed by atoms carries information about atomic structure and dynamics, providing a toolkit to investigate a large spectrum of phenomena in atomic and molecular physics.

Over the past decades, the research in atomic, molecular and optical (AMO) physics has led to an elaborate toolkit to control the internal and external degrees of freedom of atoms. Proceeding with the progress of laser cooling- and trapping techniques for dilute gases of neutral atoms [1, 2], cold atoms experiments have evolved into a powerful platform for the study of quantum mechanics. The first proposals for laser cooling have been published by A. Ashkin [3], T. Hänsch and A. Schawlow [4] and D. Wineland an H. G. Dehmelt [5] and after one decade, cooling [6] and trapping [7–9] of neutral atoms was realized experimentally, followed by the first realization of Bose-Einstein condensates [10, 11].

Since these scientific breakthroughs, the field of cold atom research has evolved drastically and expanded its variety of investigation and manipulation tools to an impressive extend. One part of this ever-increasing toolbox is the controlled and robust interaction of atomic systems with an intra-cavity electromagnetic radiation field [12–14]. This field is known as cavity quantum electrodynamics (cQED) and deals with the mutual coupling of an electromagnetic cavity field with the electronic degrees of freedom of an atom. It involves the coupling enhancement between light and atoms by confining the photons in a very small mode volume around the atoms. It is possible to find a regime, called strong coupling, in which the exchange of energy between light and matter is coherent and dominates the energy losses of the system caused by its interaction with the environment.

The cQED domain has undergone incredible growth since its early days regarding the myriad of different experimental platforms enabling its implementation. Besides neutral atoms, Rydberg atoms in microwave cavities [15] and ions in optical cavities [16] play an important role. In the field of condensed matter, superconducting qubits [17–19] and spin quantum dots [20–22] in circuit QED devices have shown remarkable progress and are a strong candidate for future quantum devices. However, one of their bigger challenges remains the short coherence times.

The large distribution of transitions frequencies of solid state leads to an inhomogenous broadening, which affects the systems' coherence and limits their performance compared to atomic systems [23].

As different as these experimental platforms are, as different can be their scientific goals – and studying *entanglement* is of them. After almost a century since its foundation, quantum mechanics has proven an unprecedented accuracy for the time being when it comes to predict the outcome of experimental measurements on the microscopic scale. However, quantum mechanics also comes up with some intriguing effects that have no equivalent in classical physics. Probably one of the most counterintuitive and fascinating phenomena is entanglement. This term was first introduced by Schrödinger in 1935 [24] to describe the fact that the global state of two initially independent subsystems cannot be described by a product state of the subsystems after having interacted [25].

This key concept of quantum mechanics was experimentally demonstrated in 1982 in Alain Aspect's group for a bipartite system in the field of quantum optics [26, 27]. A pair of unique entangled photons has indeed made it possible to measure the violation of the so-called Bell inequality, thus demonstrating the non-locality of the quantum world. But still, some fundamental unease surrounds this topic. It has its roots in the strong separation of the microscopic scale of quantum mechanics and the macroscopic classical world. A still open question is how the classical world emerges from the microscopic rules of quantum mechanics and why fundamental quantum effects such as entanglement and non-local correlations are not observable in our macroscopic framework. An approach to find potential answers to these questions is to study quantum mechanical systems at the microscopic scale and to understand why even at this scale entanglement and non-local correlations are difficult to generate and preserve.

Nowadays, the concept of entanglement quickens also the creativity when it comes to new quantum technologies and has led to many proposed and realized implementations for quantum computation [28, 29], simulation [30, 31] and communication [32, 33]. They define contemporary hot topics and are briefly motivated in the following.

Quantum computing and simulation: Quantum computers exploit the superposition principle and quantum entanglement to form a new resource to overcome performance limitations of classical computers. For the time being, many proposals for applications aim on calculating the time evolution of wave functions in order to simulate complex quantum mechanical system. But the realization of quantum computers and simulators entails extraordinary challenges, as entangled states are quite sensitive to dissipative processes. Therefore, scalability is still a big concern. Another core component of the roadmap towards quantum computers is

the development of new quantum algorithms. Depending on the type of problem, certain quantum algorithms are supposed to outperform conventional algorithms on classical computers. So only new algorithms can exploit the full potential of quantum computation in order to implement a powerful and symbiotic architecture of classical and quantum computers.

Quantum cryptography: Quantum cryptography applies fundamental laws of quantum mechanics to perform cryptographic tasks in communication. The probably best known example is the quantum key distribution, which was first proposed in the 1970s. It uses encoding based on photon polarization and by virtue of the no-cloning theorem, eavesdropping cannot go unnoticed as signals cannot be detected directly without disturbing them.

Enabling technologies for quantum systems: Not only the successful realization of these quantum technologies itself is of great relevance for scientific, political and economic actors, but also the so-called *enabling technologies*. The transition from laboratory setups to robust, reliable and cost-effective devices is important for the scalability of quantum technologies. It is therefore to be expected that breakthroughs in quantum technologies will potentially have great impact on many other high-tech domains, leading to new emerging technology markets.

Quantum metrology: While the fragility of quantum states makes the development of quantum computers and quantum communication technologies challenging, it opens up enormous potential in metrology. As the coupling to environmental influences is nothing more than a high level of technical measurement sensitivity, well designed quantum systems are likely to measure physical parameters such as time, electric and magnetic fields or gravity with an unprecedented precision. Atomic clocks are based on atomic states and have been used as a precision time reference over many decades. Gravimeters based on the cold-matter interferometry can detect small variations in the earth's gravitational field, as caused by different material compositions of the earth's crust. Even though numerous devices have been developed and commercialized over the last decades, none of these applications has successfully made use of entanglement to overcome the *standard quantum limit* (SQL) on a metrologically relevant level. New quantum sensors that overcome the SQL have the potential for outstanding ultra-precision measurements and also pave the way for miniaturization and significant cost reduction.

To date, the most promising entangled states for quantum metrology are the squeezed states, that have been introduced in 1993 by Kitagawa and Ueda [34], along with the one-axis-twisting Hamiltonian. Applied in gravitational wave detectors, squeezed light allows to overcome the shot noise limit and thus enables

the measurement of weaker gravitational wave signals. But beyond spin squeezing, the field of cQED is rich of schemes that allow to create and study entangled states. In the hosting group, the generation of entangled W-states [35] and the creation of entanglement by quantum Zeno dynamics [36] have been successfully demonstrated. Encouraged by these experimental prospects, a new experimental apparatus dedicated to the exploration of multi-particle entanglement has been developed throughout this thesis. This new experiment will provide a strong collective atomic interaction by a high-finesse ring cavity.

Scope of this thesis

Following this prologue, this thesis is divided into four chapters. Chapter 1 will recall the most relevant theory basics by describing the light-matter interaction in an optical resonator. It further introduces the strong coupling formalism of an atomic ensemble in a cavity. In addition, it provides a short introduction to the atomic properties of the alkaline-earth like metal strontium and concludes on the interest on combining strontium with cavities in the strong coupling regime. Chapter 2 then continues with the presentation of the new compact strontium apparatus to study multi-particle entanglement. Chapter 3 is devoted to the CO_2 laser dot milling method that has been used to fabricate a micro mirror-structure for compensating the intrinsic astigmatism of ring cavities. Chapter 4 is dedicated to the compact ring cavity and a low-finesse prototype that was used to confirm the design principles. This chapters includes design, assemblage and characterization measurements. Eventually, this work is concluded with an outlook on future experimental schemes.

Chapter 1

Introduction to strontium in the context of cavity QED

The interaction of atoms with an electromagnetic radiation field is one of the most fundamental processes of quantum mechanics. Not only is it an exquisite tool for cooling and trapping of atoms and the preparation and control of them, but it is also interesting to study the light-matter interaction at the fundamental level.

Among the great number of different experimental techniques, cavities are an excellent method to exploit the physics of light-matter interactions as they strongly enhance them. The parameter space of interest is the so-called *strong coupling regime*. The associated long-range photon-mediated interactions provide a powerful toolkit to implement quantum non-destructive (QND) measurements of the atomic states and, beyond that, to create multi-particle entanglement.

The underlying model is the Jaynes-Cummings Hamiltonian, which will be introduced in the following. The model will then be extended to an open system, accounting for dissipative loss processes, before being generalized to a N atom system. An observable phenomena of this system is the shift of the system's resonance frequency which occurs when the relevant atomic transitions are strongly coupled to the cavity field. This approach has been used to successively create more and more sophisticated techniques to manipulate and determine the state of the atomic ensemble and as an example, a non-demolition measurement technique of the atomic quantum state will be reviewed.

A very detailed derivation of most of the content and many references for further details are given in [37].

1.1 Brief introduction to the atom-cavity interaction

1.1.1 Coupling of a single atom to a cavity mode

Let's first consider the simple case of a two-level atom with the ground state $|g\rangle$ and the excited state $|e\rangle$, which couples to the mode of an electromagnetic cavity field. The entire quantum system is described by the Rabi Hamiltonian [38]:

$$\begin{aligned}\hat{H}_{\mathrm{R}} &= \hat{H}_{\mathrm{at}} + \hat{H}_{\mathrm{c}} + \hat{H}_{int} \\ &= \hbar\omega_{\mathrm{at}}\hat{\sigma}^{+}\hat{\sigma}^{-} + \hbar\omega_{\mathrm{c}}\hat{a}^{\dagger}\hat{a} + \hbar g(\mathbf{r})\left(\hat{a}^{\dagger} + \hat{a}\right)\left(\hat{\sigma}^{+} + \hat{\sigma}^{-}\right) .\end{aligned} \tag{1.1.1}$$

The term $\hat{H}_{\mathrm{at}}$ denotes the atomic Hamiltonian, with $\hat{\sigma}^{+} = |e\rangle\langle g|$ and $\hat{\sigma}^{-} = |g\rangle\langle e|$ the atomic raising and lowering operators which excite and de-excite the atom. ω_{at} denotes the angular frequency difference between the two states. The cavity mode Hamiltonian $\hat{H}_{\mathrm{c}}$ involves the photon creation and annihilation operators $\hat{a}$ and $\hat{a}^{\dagger}$, as well as the angular frequency ω_{c} of the mode.

The last term $\hat{H}_{\mathrm{int}}$ describes the coherent energy exchange between the radiation field and the atom. The strength of this interaction is described by the coupling parameter $g(\mathbf{r})$ which can be expressed as the product of the dipole moment and the cavity mode of amplitude E_0 at the position of the atom:

$$g(\mathbf{r}) = -\mathbf{d}_{ge} \cdot E_0 \mathbf{u}_0(\mathbf{r})/\hbar \,. \tag{1.1.2}$$

Here, the electric dipole of the neutral atom $\hat{\mathbf{d}} = \sum_{g,e} \mathbf{d}_{eg} |g\rangle\langle e|$ has been used, which connects the atomic energy levels $|g\rangle$ and $\langle e|$. Furthermore, $\mathbf{u}_0$ describes the normalized spatial dependence of the mode and includes its polarization.

The maximum attainable coupling is given by

$$g = \sqrt{\frac{\omega_c}{2\hbar\epsilon_0 V}} d_{ge} \,, \tag{1.1.3}$$

where ϵ_0 is the dielectric vacuum permittivity and V the mode volume of the cavity. The light-matter coupling therefore increases if the mode volume is smaller.

The expanded interaction term $\hat{H}_{\mathrm{int}}$ of the Rabi Hamiltonian can be further simplified by applying the *Rotating Wave Approximation* [38, 39]. The Hamiltonian then contains only two terms which correspond to the relaxation of the atom in the ground state with simultaneous emission of a photon, $\hat{a}^{\dagger}\hat{\sigma}^{-}$, and vice versa the destruction of a photon with simultaneous excitation of the atom from the ground to the excited state, $\hat{a}\hat{\sigma}^{+}$. The resulting Hamiltonian of the entire system is known as the *Jaynes-Cummings Hamiltonian* $\hat{H}_{\mathrm{JC}}$ [40]:

$$\hat{H}_{\mathrm{JC}} = \hbar\omega_{\mathrm{at}}\hat{\sigma}^{+}\hat{\sigma}^{-} + \hbar\omega_c\hat{a}^{\dagger}\hat{a} + \hbar g\left(\hat{a}^{\dagger}\hat{\sigma}^{-} + \hat{a}\hat{\sigma}^{+}\right) . \tag{1.1.4}$$

This Hamiltonian can be diagonalized and the eigenvalue problem yields to the eigenfrequencies, which correspond to the eigenstates called *dressed states* [38]. They are the linear superposition of states in which the energy of one photon has either been absorbed by the atom ($|e, n-1\rangle$) or remains in the cavity mode ($|g, n\rangle$):

$$\begin{aligned} |n, +\rangle &= \cos\theta_n |e, n-1\rangle + \sin\theta_n |g, n\rangle \\ |n, -\rangle &= \sin\theta_n |e, n-1\rangle + \cos\theta_n |g, n\rangle \end{aligned} \tag{1.1.5}$$

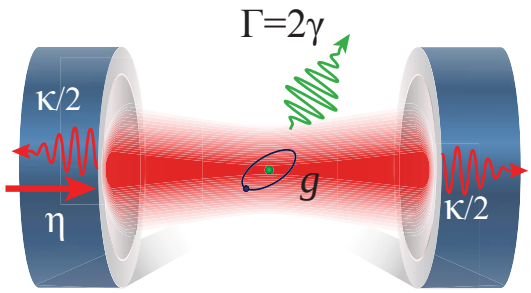

Figure 1.1.1: Illustration of an atom-cavity system interacting with its environment. The system's coupling constant is g. The spontaneous emission of the atom in the excited state is defined by the constant Γ and the cavity losses by κ. η represents the effective amplitude of a pump field injected into the cavity mode.

with θ_n defined by

$$\begin{aligned} \sin(2\theta_n) &= \frac{\sqrt{n}g}{\sqrt{\frac{(\omega_{\mathrm{at}}-\omega_c)^2}{4}+g^2n}}\,, \\ \cos(2\theta_n) &= \frac{(\omega_{\mathrm{at}}-\omega_c)/2}{\sqrt{\frac{(\omega_{\mathrm{at}}-\omega_c)^2}{4}+g^2n}}\,. \end{aligned} \tag{1.1.6}$$

Here, $|n\rangle$ are the Fock states of the cavity field. The eigenfrequencies are

$$\omega_{\pm}^{(n)} = n\omega_c + \frac{1}{2}\left((\omega_{\mathrm{at}}-\omega_c) \pm \sqrt{(\omega_{\mathrm{at}}-\omega_c)^2+4g^2n}\right)\,. \tag{1.1.7}$$

The energy separation between the two dressed states of the system scales with the square root of the photon number n. While the 'bare' states $|g,n\rangle$ and $|e,n-1\rangle$ cross each other for $\omega_c = \omega_{\mathrm{at}}$, the dressed states repel each other and an anti-crossing of the energy levels can be observed. This results in two resonant frequencies, this phenomenon is called the *vacuum Rabi splitting* [38].

1.1.2 An open atom-cavity system

So far, only a closed system with unitary dynamics has been considered. It neglects several important dissipative processes that occur in an optical cavity coupled to its environment. The atom can spontaneously (and incoherently) emit photons into free space modes with a decay rate of Γ (FWHM)[1] and the photons present in the cavity can escape with a decay rate κ if the mirror's transmission is not strictly nil. Additionally, the system can be pumped by injecting photons directly into the cavity mode with a photon flux η or by exciting the atom with a transverse beam. The figure 1.1.1 shows these different interaction channels with the environment.

[1] In compliance to the spin squeezing community [41, 42], the atomic decay rate is defined as the FWHM ($\Gamma = 2\gamma$).

By comparing the coupling strengths between the cavity mode and the atom with the system's coupling to its environment, two regimes can be distinguished: the *weak coupling* and the *strong coupling* regime.

If the losses of the system are much greater than the coupling between the atom and the mode, then the coupling is called weak, this means that a photon will be lost of the cavity mode before having interacted several times with the atom. In this weak coupling regime, the rate, at which spontaneous emission of the atom trapped inside the cavity occurs, is elevated.

In the case where coherent atom-cavity interactions dominate over dissipative processes, i. e. $g \gg \kappa, \Gamma$, the Vacuum Rabi splitting is observable and the system can be described by the Jaynes-Cummings Hamiltonian. The system is in the strong coupling regime. This results in a coherent energy exchange between the atom and the cavity field, in other words, a photon of the cavity mode interacts many times with the atom before leaving the cavity.

Other characteristic properties for describing the atom-cavity system are the *critical photon number* $n_0 = \frac{\Gamma^2}{g_0^2}$, which indicates at which photon number the coherent interaction begins to saturate, and the *critical atom number* $N_0 = \frac{\kappa\Gamma}{4g_0^2}$; this is the mean number of atoms in the cavity at which a coherent exchange begins to dominate. Its reciprocal value is called the single-atom cooperativity C_0 of the system and reads [41]

$$C_0 = \frac{1}{N_0} = \frac{4g_0^2}{\kappa\Gamma} = \frac{3\lambda^2}{\pi^3}\frac{\mathcal{F}}{w_0^2}\,, \tag{1.1.8}$$

where λ is the transition optical wavelength and $\mathcal{F}$ the cavity finesse. It is important to state that the single atom cooperativity does not depend on the cavity length [43].

If a resonator fulfills the conditions $C_0 > 1$ and $\kappa \gg \Gamma$, the cavity is further associated with the *bad cavity regime*. In this particular strong coupling regime, an excited atom in a cavity mode is more likely to decay by emitting a photon into the cavity mode rather than emitting a photon into free space. This effect is known as the Purcell effect [44].

1.2 Coupling an atomic ensemble to a cavity

In the previous section, only the case of a single atom coupled to a cavity mode field has been taken into account. In many experimental situations, however, a more complex situation is present where an atomic ensemble interacts collectively with the cavity. Therefore, a brief generalization of the theoretical framework to a N atom system is introduced in the following.

Collective spin formalism: The physical system of interest is an ensemble of N identical atoms each of which has two distinct states labeled $\{|0\rangle, |1\rangle\}$ and the ensemble can be therefore conveniently modeled by the collective (pseudo) spin, where each particle k has the spin $\left|\hat{\mathbf{j}}^{(k)}\right| = 1/2$. The collective spin vector reads as sum of the individual spins

$$\hat{\mathbf{J}} = \sum_{k=1}^{N} \hat{\mathbf{j}}^{(p)} . \tag{1.2.1}$$

This description puts some constraints on the control and the information of the collective state. First of all, the state needs to be symmetric under particle exchange. Furthermore, the operations on the ensemble affects all atoms in the same way and the measurable quantities are usually the occupation distributions of N_1, N_2 in $|0\rangle, |1\rangle$.

Dicke states: Considering a system composed of N two-level atoms described by its total spin vector $\hat{\mathbf{J}}$, then the eigenstates $\{|J, J_z\rangle\}$ of the operators

$$\hat{J}^2 = \hat{J}_x^2 + \hat{J}_y^2 + \hat{J}_z^2 \quad \text{and} \quad \hat{J}_z = \sum_{k=1}^{N} \hat{J}_z^{(k)} \tag{1.2.2}$$

are a convenient basis. As states of this subspace have the maximum angular momentum $J = N/2$, a basis can be formed where

$$|n_N\rangle = |J = \frac{N}{2}, J_z = -\frac{N}{2} + n\rangle \quad \text{with} \quad n = 0, 1, \ldots, N . \tag{1.2.3}$$

In these states precisely $J_z = N/2 + n$ atoms will be found in the $|1\rangle$ state and are known as the *Dicke states*.

Coherent Spin States (CSS) and the Bloch sphere: When it comes to collective atomic states of classical nature, one can define the class of coherent spin states (CSS) [45]. These states are fully defined by two angles θ, ϕ:

$$|\theta, \phi\rangle = \left[\sin(\theta/2)e^{i\phi/2}\,|0\rangle + \cos(\theta/2)e^{-i\phi/2}\,|1\rangle\right]^{\bigotimes N} . \tag{1.2.4}$$

They are classical in a two-fold sense: first, a CSS represents a coherent superposition where the individual atoms are in a well-defined pure state and totally independent of other particles of the ensemble. Secondly, the CSS can also be understood as the result of operating a collective rotation operator applied to the state $|0_N\rangle$ of zero excitations:

$$|\theta, \phi\rangle = \mathbf{R}(\theta, \phi)\,|0_N\rangle . \tag{1.2.5}$$

One can therefore interpret $|\theta, \phi\rangle$ as a collective spin pointing in a certain direction. This provides a simple pictorial representation of a state on the multiparticle Bloch sphere. Furthermore, the CSS shows an equally distributed uncertainty along the coordinates transversal to the direction of J and is depicted in figure 1.2.2a.

An instance of a CSS is an atomic ensemble prepared in the $|0\rangle$ state which is then excited with a $\pi/2$-pulse, by rotating the collective spin around e. g. the x-axis:

$$R_{\mathbf{x}}(\phi) = \exp(-i\phi \mathbf{x} \cdot \mathbf{J}) \,. \tag{1.2.6}$$

The resulting CSS along the y-axis then reads

$$|\mathrm{CSS}_y\rangle = \left(\frac{|0\rangle + |1\rangle}{\sqrt{2}}\right)^{\bigotimes N} . \tag{1.2.7}$$

Tavis-Cummings model: The previously introducded Jaynes-Cummings Hamiltonian describes the coherent exchange of energy between a single atom and a cavity mode. However, if one wants to study the collective coupling of an atomic ensemble consisting of N two-level atoms to a cavity mode, an extension of this model has to be studied: it is known as the *Tavis Cummings model* [46]. Starting point for this model are N atoms, which all couple equally to the cavity mode. With the collective spin operators

$$\hat{J}_z = \sum_{k=i}^{N} \hat{\sigma}_k^+ \hat{\sigma}_k^- \quad \text{and} \quad \hat{J}_\pm = \sum_{k=i}^{N} \hat{\sigma}_k^\pm \,, \tag{1.2.8}$$

the system's Hamiltonian, also known as Dicke model, takes then the form [47]

$$\hat{H}_\mathrm{D} = \hbar\omega_\mathrm{at} \hat{J}_z + \hbar\omega_c \hat{a}^\dagger \hat{a} + \hbar g \left(\hat{a}^\dagger + \hat{a}\right)\left(\hat{J}_+ + \hat{J}_-\right) . \tag{1.2.9}$$

As in the previous case of the Jaynes-Cummings Hamiltonian, rewriting the Hamiltonian in a rotating frame at the atomic transition frequency ω_at leads to simplified Hamiltonian, known as the Tavis-Cummings Hamiltonian:

$$\hat{H}_\mathrm{TC} = \hbar\omega_\mathrm{at} \hat{J}_z + \hbar\omega_c \hat{a}^\dagger \hat{a} + \hbar g \left(\hat{a}^\dagger \hat{J}_+ + \hat{a} \hat{J}_-\right) . \tag{1.2.10}$$

***N* atoms in a two mode ring cavity:** As a ring cavity can host two counterpropagating running wave modes, the Tavis Cummings model expanded to include this very aspect. Each cavity mode is assumed to be driven with a field of frequency η_1, η_2. Following equation 1.1.1, the Hamiltonian can be split into three parts:

$$\hat{H}_\mathrm{TC} = \hat{H}_\mathrm{at} + \hat{H}_\mathrm{c} + \hat{H}_{int} \tag{1.2.11}$$

where

$$\begin{aligned}\hat{H}_{\mathrm{at}} &= \hbar\omega_{\mathrm{at}}\hat{J}_z\,,\\ \hat{H}_{\mathrm{c}} &= \hbar\omega_c\left(\hat{a}_1^\dagger\hat{a}_1+\hat{a}_2^\dagger\hat{a}_2\right)\,,\\ \hat{H}_{\mathrm{int}} &= \hbar g\sum_{j=1}^{N}\left(\hat{a}_1^\dagger\hat{\sigma}_j^+e^{-2ikz_j}+\hat{a}_1\hat{\sigma}_j^-e^{2ikz_j}\right)+\hbar g\sum_{j=1}^{N}\left(\hat{a}_2^\dagger\hat{\sigma}_j^+e^{-2ikz_j}+\hat{a}_2\hat{\sigma}_j^-e^{2ikz_j}\right)\,,\end{aligned} \tag{1.2.12}$$

with z_j and p_j the particles' center-of-mass positions and momentum operators, respectively. The coupling coupling parameter g is assumed to be equal for both modes and $\hat{a}_{1,2}$ denote the photon creation operators for both cavity modes [48]. Due to scattering of photons on the atomic cloud (or on the cavity mirrors), a redistribution of photons between the two cavity modes can occur. Furthermore, linear momentum is a conserved quantity in a ring cavity and each scattering event transfers an impulse to the atoms of mass m. Therefore, photon scattering in a ring cavity corresponds to a phonon exchange between the light field and the atomic center-of-mass along the cavity axis. Under the assumption that the cavity field is far detuned from the atomic resonance ($\Delta=\omega_{\mathrm{at}}-\omega_{\mathrm{c}}$) and the atomic excited states are thus only weakly saturated, $\hat{H}_{\mathrm{int}}$ in equation 1.2.12 can be approximated by [49, 50]

$$\hat{H}_{\mathrm{int}}=\frac{1}{2m}\sum_{j=1}^{N}p_j^2+\hbar\frac{g^2}{\Delta}\left(\sum_{j=1}^{N}\hat{a}_2^\dagger\hat{a}_1e^{-2ikz_j}+\hat{a}_1^\dagger\hat{a}_2e^{2ikz_j}\right)\,. \tag{1.2.13}$$

The dynamics of the atom-cavity system ρ is described by the master equation

$$\dot{\hat{\rho}}=-\frac{i}{\hbar}\left[\hat{H}_{\mathrm{TC}},\hat{\rho}\right]+\mathcal{L}\hat{\rho}\,, \tag{1.2.14}$$

where $\mathcal{L}=\mathcal{L}_{\mathrm{at}}+\mathcal{L}_{\mathrm{cav},1}+\mathcal{L}_{\mathrm{cav},2}$ represents different dissipation processes with [48]

$$\begin{aligned}\mathcal{L}_{\mathrm{at}}\,\rho &= -\Gamma\left(\hat{J}_-\hat{J}_+\rho(t)-2\hat{J}_-\rho(t)\hat{J}_++\rho(t)\hat{J}_-\hat{J}_+\right)\,,\\ \mathcal{L}_{\mathrm{cav},12}\,\rho &= -\kappa\left(\hat{a}_{12}^\dagger\hat{a}_{12}\rho(t)-2\hat{a}_{12}\rho(t)\hat{a}_{12}^\dagger+\rho(t)\hat{a}_{12}^\dagger\hat{a}_{12}\right)\,.\end{aligned} \tag{1.2.15}$$

The total momentum of particles and fields including pump and losses is conserved, in contrast to a linear cavity where the mirrors can absorb momentum. This principle has been also proposed to create a quantum logic gate [51]. In the proposed scheme by Hemmerich, atoms are loaded into the motional ground state of an optical lattice constituted by the standing wave of a symmetrically pumped ring cavity. By focusing lasers on a one of these atoms, it experiences a kick which corresponds to a photon rescattered between the cavity modes and, since momen-

tum is conserved in a ring cavity, to a phonon shared by all atoms. This technique is similiar to the quantum logic gates in ion trap systems [28].

The case of a single side pumped ring cavity has been widely studied and is known as *Collective Atomic Recoil Lasing* (CARL) [52, 53]. It is a collective process that is observed when ultracold atoms are loaded into the mode of a ring cavity, where they are illuminated with photons from a single resonator mode. By scattering at inhomogeneities in the atomic cloud, light enters the opposite resonator mode. The two light fields interfere with each other and form a standing wave. This standing wave represents a dipole potential for the atoms, which causes them to be pulled into the antinodes to atomic resonance when they are red tuned. So within the cloud, areas of high and low density alternate. At this periodic structure, further pump photons are scattered in the opposite direction by Bragg scattering, which increases the standing wave contrast and strengthens the density modulation of the cloud. CARL is thus a self-reinforcing process. Due to the scattering process of the photons in the opposite direction, an impulse $p = 2\hbar k_{\mathrm{ph}}$ is transferred to the atoms. The atoms are thus accelerated in the pumping direction. The scattered light undergoes a Doppler shift, so that the optical standing wave also begins to shift spatially synchronously with the accelerated atoms.

1.2.1 Joint measurement of the internal state of atoms in a cavity

Considering the atomic energy levels shown in figure 1.2.1a, the vacuum Rabi splitting can be observed experimentally in the strong coupling regime by varying the frequency of the probe beam injected into the cavity and by measuring the power of the transmitted beam. The transmission signal shows intensity peaks with a frequencies offset of $\pm g$ with respect to the resonance frequency of the empty cavity, as shown schematically in figure 1.2.1.

One can take advantage of this effect to perform a non-destructive quantum measurement of the atomic state in order to determine how many atoms are in state $|0\rangle$ or $|1\rangle$ [54, 55]. For this purpose, the detection is carried out while keeping the probe frequency on resonance with the empty cavity. Let's first consider the case where a single atom sits in the cavity. If it is in the resonant state $|1\rangle$, the resonance of the cavity is shifted and no photon by the probe can enter the cavity, therefore the transmission is almost zero. If the atom is not in state $|1\rangle$ but in $|0\rangle$, then the transmission is non-zero. In addition, the presence of photons in the cavity induces very low decoherence of the atomic state since the probe light is far off-resonant. The measurement of the cavity transmission thus makes it possible to determine the atomic state.

To be more quantitative, the presence of a single atom in state $|1\rangle$ reduces the

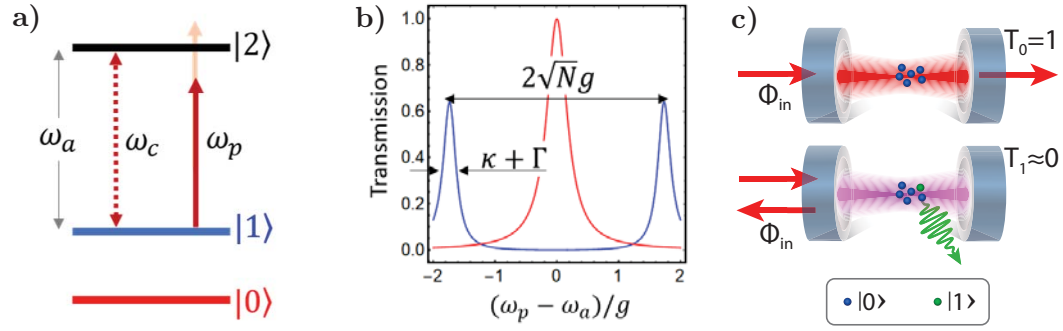

Figure 1.2.1: (a) shows a schematic representation of the commonly used rubidium-87 level scheme for CQED. The empty cavity is resonant with the transition $|1\rangle \rightarrow |2\rangle$, the state $|0\rangle$ is not coupled to the cavity. (b) depicts the Vacuum Rabi splitting. The system resonances are displaced by the factor $\sqrt{N}g$ with respect to the resonance of the empty cavity. The width of the peaks is $(\kappa+\Gamma)/2$. (c) shows illustration of the corresponding atom-cavity system with a probe at frequency ω_p.

transmission of a probe resonant with the empty cavity:

$$\frac{T_1}{T_0} = \frac{1}{(1+2C_0)^2}\,, \tag{1.2.16}$$

where T_0 is the transmission of the empty cavity [35]. If now not only one but an atomic ensemble is placed in the cavity, the phenomenological description of the system is similar: when at least one atom is resonant with the cavity, the transmission is almost zero whereas when all the atoms are in the state $|0\rangle$, a significant amount of the probe light passes through the cavity. The equation 1.2.16 can be then rewritten by replacing the single atom cooperativity C_0 with collective cooperativity C_N as

$$C_N = \frac{4g_N^2}{\kappa\Gamma} = N \cdot C_0\,. \tag{1.2.17}$$

In conclusion, by fixing the probe to the resonant frequency of the empty cavity, it is possible to determine if at least one atom is coupled thereto. Indeed, as shown in figure 1.2.1b, the transmission of the cavity reflects the state of the atoms trapped therein. The higher the cooperativity, the greater is transmission suppression factor. The measurement thus makes it possible to distinguish the state $|0000\ldots0\rangle$ from any other state where one or more atoms are resonant with the cavity, without the exchange of energy between the probe and the system. Therefore, the measurement is called as *non-destructive*.

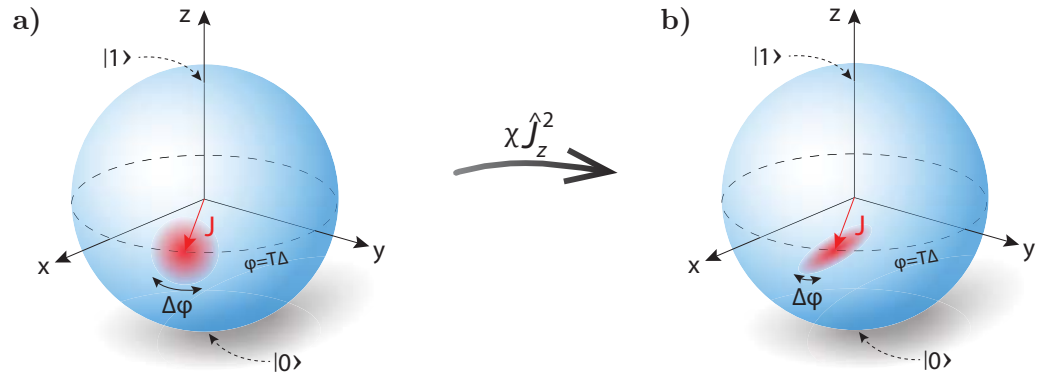

Figure 1.2.2: Visualization of the $\chi \hat{J}_z$ term, known as the one-axis-twisting. a) shows an illustration of a coherent and b) of spin-squeezed state on the Bloch sphere (blue). The red blurred ellipse at the atomic state vector's tip indicates the uncertainty region of the transversal spin components.

Spin Squeezed States (SSS): One class of entangled quantum states are the spin-squeezed states. If one considers an atomic ensemble created in the CSS at the equator of the Bloch sphere, interesting dynamics arise when the cavity is detuned from the atomic resonance. The CSS is brought into an entangled state and is known as *one-axis twisting* (OAT) Hamiltonian [34]. This effect is depicted in figure 1.2.2b

These dynamics can be described as cavity-mediated interactions between the effective spins formed by the states $|0\rangle$ and $|1\rangle$. The frequency shift, that both transitions levels experience, gives rise to atom-atom correlations and scales with the atomic inversion. The system's Hamiltonian can be written in terms of the collective spin operators $\hat{J}_{x;y;z}$, with $\hat{J}_z$ corresponding to the atomic inversion:

$$\hat{H}_{\text{eff}} = \hbar\chi \hat{J}^+ \hat{J}^- \approx \hbar\chi \left(\hat{J}^2 - \hat{J}_z^2 \right) . \tag{1.2.18}$$

Here, $\hat{J}^{\pm} = \hat{J}_x \pm i\hat{J}_y$ and $\chi = C_N \Gamma \frac{\Delta/\kappa}{1+(2\Delta/\kappa)^2}$, where Δ denotes the detuning of the cavity resonance from the atomic transition. Illustratively, the $\chi \hat{J}_z^2$ term leads to a shearing effect, which is shown in figure 1.2.2b for CSS. The noise distribution, depicted by a blurred circle, becomes narrower along one direction but wider along the other.

Another way to generate SSS is by means of joint measurements. In order to produce a SSS from a CSS, the collective spin operator $\hat{J}_z$ needs to be measured. It is important that the measurement does not provide any single-particle information as the particle would otherwise not stay in the CSS [56, 57]. In the case of a

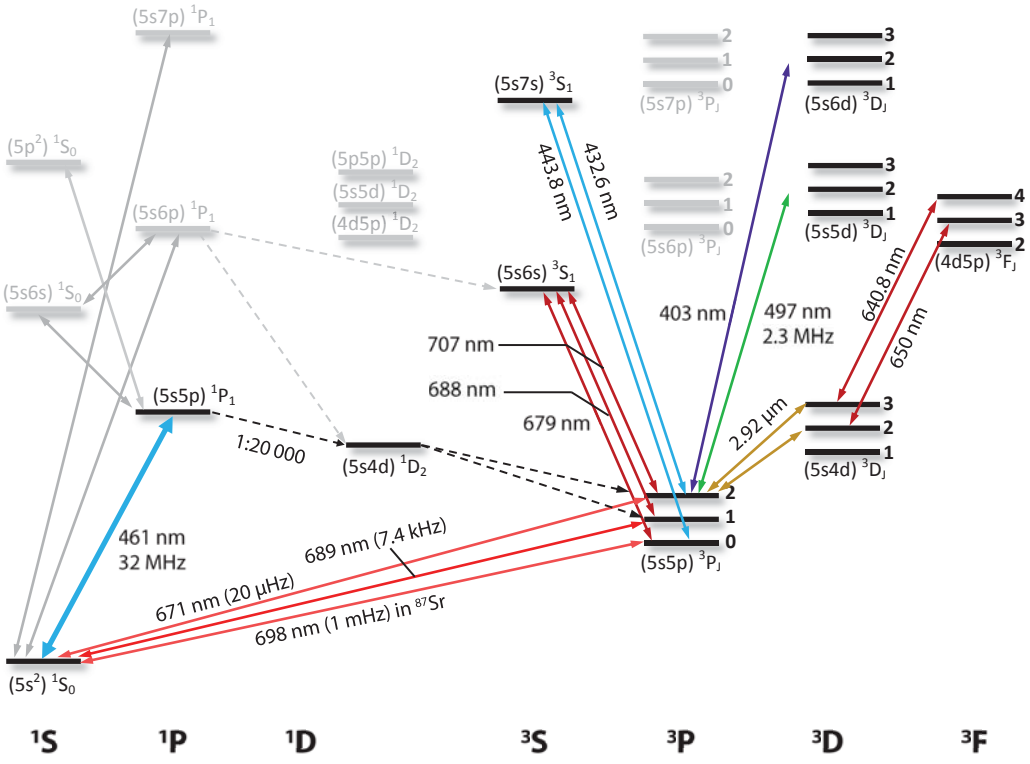

Figure 1.3.1: Excerpt from the level scheme of ^{87}Sr

cavity, the atomic ensemble is probed optically and the information about $\hat{J}_z$ is imprint onto the light field, entangling the spin and field states. The measurement performed on the light reduces then the uncertainty in $\hat{J}_z$ [58].

1.3 Ultra-cold strontium for precision measurements

The choice of strontium for the new experiment relies in the properties of its different atomic transitions, which are easily accessible with standard diode lasers. For the sake of completeness, the main atomic properties are revised in the following.

1.3.1 Physical-chemical properties

The increasing popularity of strontium in all kinds of cold-atom experiments makes it the new work horse besides rubidium-87. Its initial boost in popularity is traceable to the optical clock domain, as all of its relevant transitions are easily accessible with diode laser systems and as it features the so-called *clock transition*. Strontium is part of the alkaline-earth (like) metal or *lanthanoid* family. It has

the atomic number $Z = 38$ and has four stable isotopes, three of them are bosonic (^{84}Sr, 0.5 % – ^{86}Sr, 9.9 % – ^{88}Sr, 82.6 %) and one fermionic (^{87}Sr, 7 %) with the nuclear spin $I = 9/2$. The nuclear spin of the latter is the reason for several important spectroscopic properties.

With its two valence electrons in the closed s subshell, strontium has a level scheme similar to that of alkaline atoms but with separated singlet (anti-parallel electron spins) and triplet states (parallel electron spins). While transitions between singlet and triplet states are nominally forbidden by selection rules, spin-orbit and electron-nuclear spin coupling effects lead to a small but finite decay linewidth for certain transitions. As a result, strontium has several narrow transitions that can be used for cooling in the µK range and as a clock transition (see figure 1.3.1).

Two transitions are favorable to laser cool elemental strontium. For the Zeeman slowing and the first cooling stage, the $^1S_0 \rightarrow {}^1P_1$ transition with a linewidth of $2\pi \times 30.2\,\mathrm{MHz}$ is used. The large linewidth allows for fast cooling, but the Doppler temperature of 0.7 mK is still to high for most cold atom experiments. Although this temperature can be reduced by polarization gradient cooling down to the µK range [59, 60], this only applies to fermions and small atom numbers.

Furthermore, the excited state $^1P_1$ of the blue MOT provides a loss channel via the $^3D_2$ into the ^3P_J with a branching ratio of 1 : 20 000 [61], so that repumpers are required in order to increase the number of trapped atoms and the lifetime of the MOT. In the case of strontium, a large number of different repump schemes are available, as shown in figure 1.3.1. Lately, even repumping on the $(5s4d)\,^3D_J$ transitions has been achieved [62, 63].

The second cooling stage on the $^1S_0 \rightarrow {}^3P_1$ transition (also called *red MOT*) further reduces the temperature of the atomic ensemble thanks to a rather narrow linewidth of $2\pi \times 7.5\,\mathrm{kHz}$ and a associated Doppler limit of 0.2 µK. After this stage, atomic temperatures in the range of $1 - 10\,\mu\mathrm{K}$ are oftentimes obtained, which is enough to load efficiently the atoms into an optical lattice.

The probably most interesting transition for many state-of-the-art experiments is the doubly-forbidden clock transition $^1S_0 \rightarrow {}^3P_0$. It can be directly probed in the fermionic isotope with a natural linewidth of $\approx 1\,\mathrm{mHz}$. This transition is therefore well suited to realize not only optical lattice clock but also quantum simulation and computation. Lacking nuclear spin-induced state mixing, this transition is entirely forbidden for the bosonic strontium isotopes. Nervertheless, the required state admixture to reach the finite transition probability can be achieved by an external magnetic field [64] or circularly polarized light of the magic wavelength [65].

quantity	expression	blue MOT	red MOT
transition	–	$^1S_0 \rightarrow {}^1P_1$	$^1S_0 \rightarrow {}^3P_1$
wavelength (vacuum)	λ	460.86 nm	689.45 nm
linewidth	$\delta\nu = \frac{\Gamma}{2\pi}$	30.2 MHz [66]	7.5 kHz [67]
recoil temperature	$T_r = \frac{\hbar^2 k^2}{k_B m}$	–	460 nK
Doppler temperature	$T_D = \frac{\hbar\Gamma}{2k_B}$	725.7 µK	187 nK
saturation intensity	$I_{\text{sat}} = \frac{\pi hc\Gamma}{3\lambda^3}$	40.4 mW/cm^2	2.98 µW/cm^2

Table 1.1: Key properties of strontium MOTs.

1.3.2 Stark effect and light-shift

Optical dipole traps offer many advantages in suppressing residual displacement effects and is often the technique of choice when it comes to trapping atoms. However, when atom are exposed to a trapping light field, some parasitic light-induced energy displacement effects need to be taken into account. Dominant contributions are the polarizability, the hyperpolarizability and the blackbody radiation shift. Especially when working with the dipole forbidden transition of alkaline earth-like atoms, the narrow linewidths of their transitions require precise control over these effects.

The AC Stark effect, which allows to create a dipole potential to trap atoms, causes a frequency shift on atomic transitions. When an atom is exposed to an alternating electromagnetic field, the energies of its electronic states experience a perturbation. The energy shift of a state a is given by [68]:

$$\delta E_a^{\text{Stark}} \simeq -\alpha_a(\nu_L)E^2 - \alpha'_a(\nu_L)E^4 + \mathcal{O}\left(E^6\right) , \tag{1.3.1}$$

where $\alpha_a(\nu)$ and $\alpha'_a(\nu)$ is the (scalar) polarizability and hyperpolarizability respectively of state a and E the electric field amplitude at the frequency ν_L. For the sake of completeness: the polarizability consists of the electric dipole polarizability α_{E1}, the magnetic polarizability α_{M1} and the electric quadrupole polarizability α_{E2}.

The polarizability of the state a reads

$$\alpha_a(\nu_L) = \frac{2}{h}|d|^2 \frac{\nu_0}{\nu_0^2 - \nu_L^2} , \tag{1.3.2}$$

where ν_0 is the transition frequency of the state a, ν_L is the frequency of the applied light field and $|d|$ is the transition dipole matrix element. Up to now,

however, only a simple two-level system had been considered, which describes barely a real atomic system. Therefore, one needs to sum over all states k, which can be reached from state a via an allowed transition and contribute therefore to the polarizability [69]:

$$\alpha_a(\nu_L) = \frac{2}{h}\sum_k |d_{ak}|^2 \frac{\nu_{ak}}{\nu_{ak}^2 - \nu_L^2}\,. \tag{1.3.3}$$

The dipole matrix element $|d_{ak}|$ relates to the transition rate Γ_{ak} via [70]

$$\Gamma_{ak} = \frac{4\pi\nu_{ak}^3}{3\epsilon_0 hc^3}|d_{ak}|^2\,. \tag{1.3.4}$$

Based on these equations, the effective frequency shift of a specific transition from state a to b can be worked out by means of calculating the difference between the scalar polarizabilities of the ground and excited state:

$$\Delta\nu_{ab}^{Stark} \simeq -\frac{1}{2h}\Delta\alpha(\nu_L)\left\langle E^2\right\rangle \quad \text{with} \quad \Delta\alpha(\nu_L) = \alpha_b(\nu_L) - \alpha_a(\nu_L)\,. \tag{1.3.5}$$

If the ground and excited states have the same polarizability, i. e. $\Delta\alpha = 0$, the first order Stark effect disappears and thus also the frequency shift. This occurs at specific wavelength of the light, which are typically called *magic wavelength* and decouples the frequency of the transition of interest from inhomogeneous trap perturbations. In figure 1.3.2, the calculated polarizabilities of the $^1S_0$ ground state and $^3P_0$, $^3P_1$ excited states are shown. These calculations include also the hyperfine structure and the light field polarization, which can be taken into account via the dipole matrix elements [70]. It can be seen that the clock transition has red-detuned magic wavelengths around 500 nm and 813 nm, while the magic wavelengths of the $^1S_0 \rightarrow {}^3P_1$ transition lie around 500 nm and 913 nm.

1.3.3 On the interest of using strontium for cQED

Quantum correlations are difficult to create and intrinsically fragile to decoherence, and therefore the design and implementation of robust methods for entanglement generation is topic of many research projects. Demonstrating strong collective coupling in the new strontium system is of particular interest, as strontium atoms have proven to be very useful for metrology. But before talking about the advantages of strontium from the cQED perspective, two dissipative processes counteracting the creation of entangled states need to be mentioned first:

- **Rayleigh scattering** is an elastic scattering process which leaves the atomic

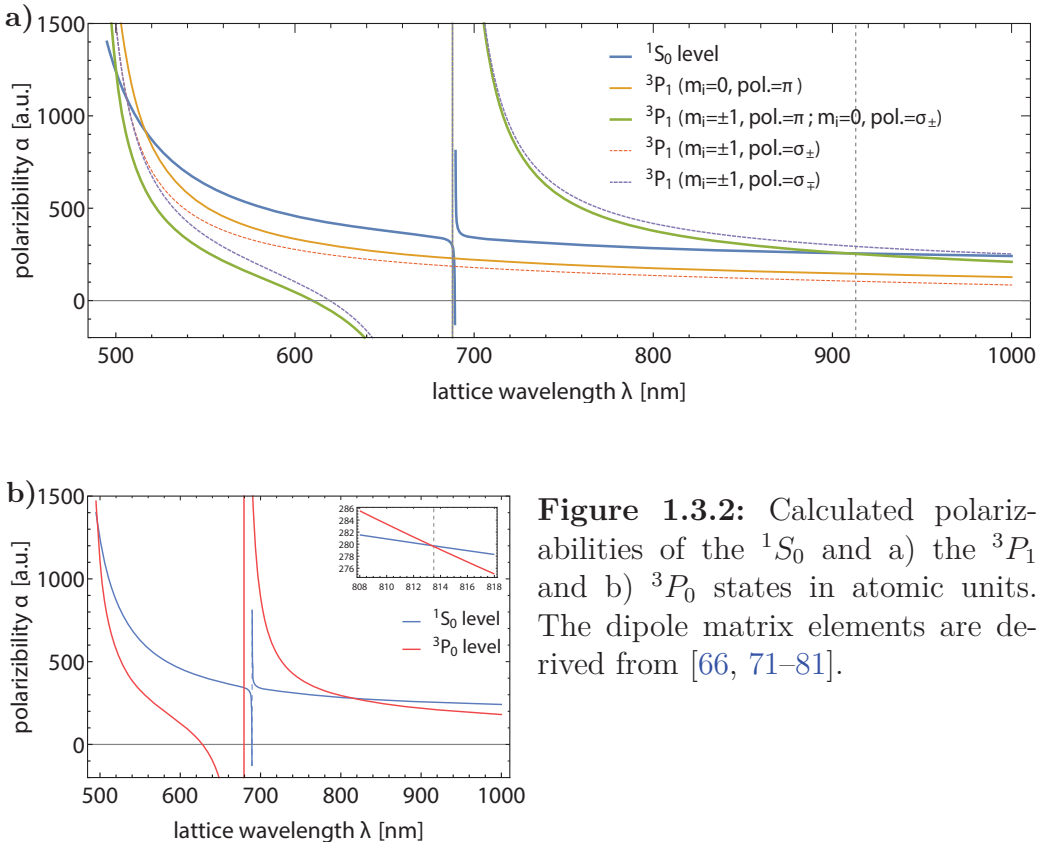

Figure 1.3.2: Calculated polarizabilities of the $^1S_0$ and a) the $^3P_1$ and b) $^3P_0$ states in atomic units. The dipole matrix elements are derived from [66, 71–81].

spin state and the light's polarization unchanged [82]. The scattered photon leaves the cavity through a mode other than the cavity mode.

- **Raman scattering** is associated with inelastic scattering where a spin flip of the atom and a corresponding polarization change of the photon occurs. This leads to entanglement of the internal states of atom and photon, which reduces the correlation of measurement outcome and the actual J_z state ([83] and references therein) and thus a diffusion of the spin projection $\hat{J}_z$.

Both processes contribute to decoherence of the collective state [83]. At this point, the energy-level structure of alkaline-earth like metal atoms comes into play. The intercombination lines of strontium highly suppress Raman spontaneous emission due to the long lifetime of the exited state. This removes e. g. a spin squeezing limit attained in alkaline atoms [84, 85].

This becomes particularly interesting for the realization of optical qubits. Considering the scheme as shown in figure 1.3.3, an optical qubit can be encoded on the

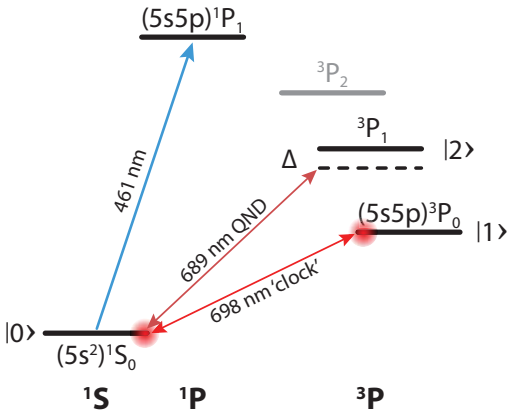

Figure 1.3.3: Relevant levels of ^{87}Sr for cavity QED. This scheme allows a QND probe of the clock transition $|0\rangle \rightarrow |1\rangle$ by exploiting a far-detuned probe on $|0\rangle \rightarrow |2\rangle$.

$^1S_0\,(|0\rangle) \rightarrow {}^3P_0\,(|1\rangle)$ transition and the collective QND readout performed on the closed optical $^1S_0\,(|0\rangle) \rightarrow {}^3P_1\,(|2\rangle)$ transition using a far-detuned probe. Not only does the long-lived qubit on the clock transition allow to store information over a long time scale or to perform many operations on the qubit, but the far-detuned QND readout also avoids any parasitic scattering events. This indeed protects the clock states from any redistribution [86] so that the population inversion $\hat{J}_z$ is conserved.

Furthermore, the fact that the condition $g \gg \kappa \gg \Gamma$ can be reached much more easily with the narrow linewidth transition of strontium makes it more likely to work in the bad-cavity regime. This is desirable for many applications as they provide a collective information about the atomic ensemble and can be easily detected, whereas emitted photons into free space lead to decoherence. This gives access to a new parameter space that is unavailable in alkaline atoms. Recent progress has been achieved on studying superradiance [87] or using cavity-feedback to generate spin squeezing of an atomic ensemble [88]. The latter achieved spin squeezing on fermionic ytterbium, which has the advantage that s-wave scattering due to the Pauli blockade is suppressed and collisional frequency shifts reduced.

But as so often, any advantage of a new method entails also new challenges that needs to be countered. Other sources of atomic broadening, such as the inhomogeneous Doppler broadening $\Delta\omega_D$ of the atomic transition suddenly dominate the coherent atom-photon interactions. Assuming that one wants to keep the ratio of coupling strength to Doppler broadening comparable to alkaline atoms ($g/\Delta\omega_D$), the temperature of the atomic ensembles needs to scale proportionally to Γ as the Doppler effect is independent from the linewidth of atomic transitions.

1.4 Guidelines for a new cQED experiment with strontium

Encouraged by the prospect and possibilities that cQED with strontium can bring for the exploration of multi-particle entangled states, a new setup has been developed. First, a compact experiment with a large optical access has been designed. The compactness is not only a way to reduce the distance between the atomic beam source and the trapping region and thus to make MOT loading much more efficient, but is also a way to improve the stability against mechanical vibrations and optics misalignment. The experiment further features an efficient effusive oven source and a 'virtual' Zeeman slower based on the on-axis field of the MOT coils. This measure reduces the thermal impact on the experiment.

This experiment in its final stage will host a miniaturized ring cavity to achieve spatially uniform strong coupling. A homogeneous strong coupling is prerequisite in many entanglement schemes that are based on atom-light interactions in cavity. Miniaturized fiber Fabry-Perot cavities were an innovative way to go if the coupling strength should be increased by reducing the cavity length and thus the cavity waist. However, the fiber-based incoupling restricts this technique to only linear two-mirror cavities. The cavity configuration of choice for the new experiment was a ring cavity. The principle advantage of this system is its traveling wave that ensures a homogeneous coupling of the atomic ensemble to the cavity field.

As previously pointed out, the single atom cooperativity does not depend on the mode volume but on the cavity waist. Therefore, a relatively long ($L \approx 600\,\mu$m) cavity in a near-concentric regime was designed to maintain maximum optical access but to reduce the waist to $w_0 \approx 3.5\,\mu$m. That, combined with a finesse of up to $\mathcal{F} \approx 5 \cdot 10^4$ should result in a single-atom cooperativity of $C_0 \approx 90$.

The design of this new strontium apparatus, the challenging fabrication of the mirrors for a miniaturized, astigmastim-compensated ring cavity as well as the conception and realization of a prototype ring cavity will be presented in the following three chapters.

Chapter 2

A new strontium apparatus for cavity QED in a ring cavity

One part of the work of this thesis was the conception of a new experimental apparatus for cooling and trapping of ultracold strontium. Its design and the current status is presented in this chapter. First, the design of a compact ultra-high vacuum chamber, in which strontium atoms are cooled and trapped, will be discussed in detail. Second, the atomic beam source is presented which stands out by its compactness and low power consumption. Furthermore, various laser systems and magnetic coil assemblies are needed to slow and cool the atomic beam and were worked out in during this thesis. Following the idea of low footprint system, a *virtual* Zeeman slower design was implemented. The Zeeman slowing process is guaranteed by the on-axis field of the MOT coils and no dedicated Zeeman slowing coils are required.

Likewise, the last section presents a test on locking a narrow-linewidth laser on a high finesse cavity by means of a 3ω demodulation technique.

2.1 The vacuum system

Since the earliest days of neutral atom trapping it has been known that trapped atoms are extraordinarily susceptible to collisions with the background gas[1] which entail immediate loss of atoms from their traps. Unlike most Bose-Einstein condensation experiments, where atoms often need to be held for minutes, the trap life time is not as demanding in optical clocks and cavity QED experiments. Values of a few seconds in the optical lattice are usually sufficient. The reason for this is that the duration of the clock laser pulse in today's experiments is limited by the quality of the clock laser to less than a second.

However, future optical clock laser systems or the application of non-destructive detection methods can increase the demands on the vacuum quality. In addition, collisions of the background gas with strontium atoms lead to a frequency shift of the clock transition [89] whose error contribution is relatively in-significant to the overall error budget in state-of-the-art optical clocks. Still, reducing the experimental sequence time and increasing vacuum quality avoids any experimental

[1] Mostly molecular hydrogen outgassing from the walls of the vacuum system

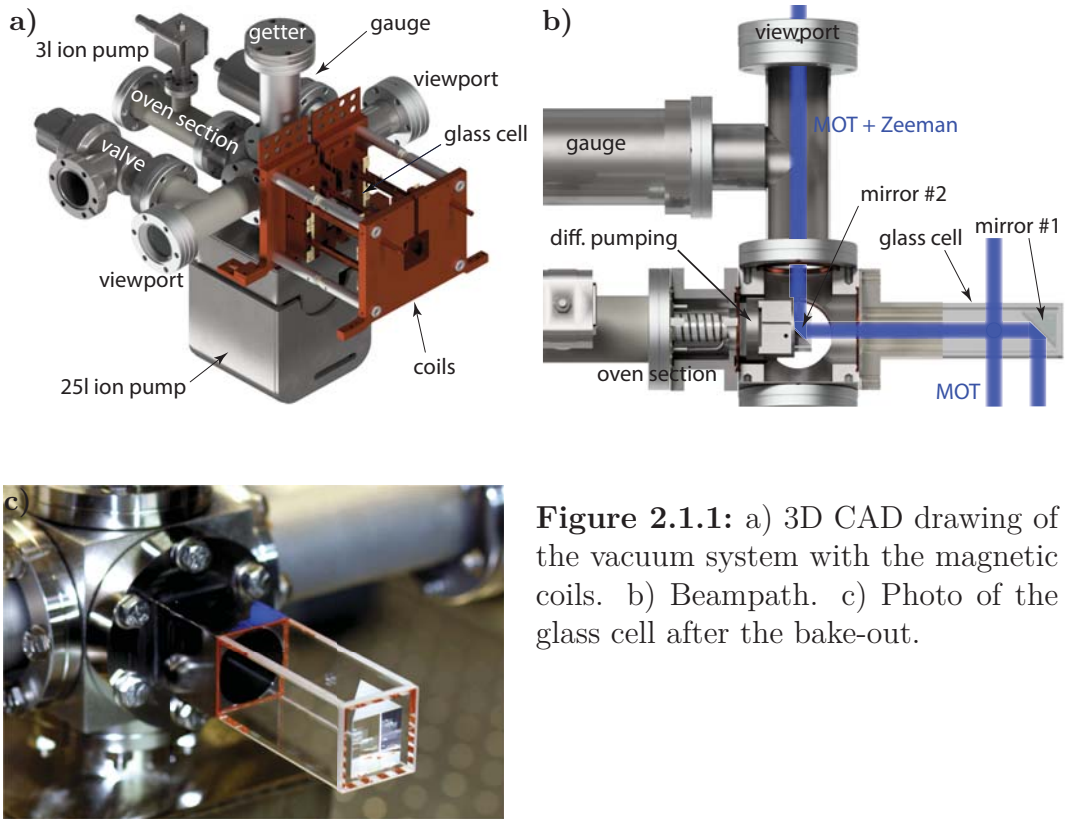

Figure 2.1.1: a) 3D CAD drawing of the vacuum system with the magnetic coils. b) Beampath. c) Photo of the glass cell after the bake-out.

limitations *a priori*, providing a safety margin as well as flexibility in view of potential future improvements of the laser system.

A CAD drawing of the vacuum assembly is given in figure 2.1.1a. It comprises two sections: The source region of elevated vapor pressure in which the atomic beam of strontium is generated (see section 2.2 for more details), the science section with increased optical access and the coil assembly to slow down and trap the atoms in a magneto optical trap (MOT).

Besides a glass cell, the science section features two in-vacuum dielectric right-angle prism mirrors (see figure 2.1.1b). The first one sits inside of the glass cell and the second is mounted on an extension of the oven section right underneath the collimation aperture of the oven. As the strontium jet is directed at the glass cell that will host the miniature ring cavity, the mirror inside of the cell is mounted under the assumption that the reflectance of its dielectric coatings suffers less from a potential strontium deposit than the transmission of plain optical glass i. e. the science cell. This measure should thus increase the lifetime of the science cell as the injection of a Zeeman and MOT beams do not encounter any strontium deposit.

Furthermore, the second mirror allows to send a MOT beam towards the viewport (see figure 2.1.1b), where it is retro-reflected.

The rectangular glass cell[2] is made of uncoated SCHOTT™ type UK 5 glass, and has external dimensions of 70 mm × 30 mm × 30 mm with a wall thickness of 2.5 mm. The cell should be replaced by a anti-reflection coated glass cell of same dimensions once the ring cavity is inserted. The cell is glued[3] on a titanium flange[4] in order to match the thermal expansion coefficient. The prism mirror inside the glass cell is glued[5] via three quartz glass plates[6] of dimension 2.5 mm × 2.5 mm × 1 mm onto the bottom of the glass cell (see figure 2.1.1c).

In the present setup, the differential pumping between the oven and science section is realized by a tube of length $L = 13\,\mathrm{mm}$ and diameter $2R = 1.5\,\mathrm{mm}$. As described in the following section, this drilled hole primarily serves as a collimation tube for the atomic jet but it also functions as differential pumping stage, which can be described as

$$Q = c\Delta P\,, \tag{2.1.1}$$

where c is the conductance between the two pressure regions reading

$$c = \left(1 + \frac{3L}{8R}\right)^{-1} \cdot \frac{\pi}{4} v R^2 \approx 0.027\,\mathrm{l/s}\,, \tag{2.1.2}$$

with v the average speed of gas inside the system[7]. The jet of Strontium atoms can also be considered as getter material that sticks to the walls after colliding with them.

The maximum achievable pressure can be estimated by taking into account the surfaces and outgassing rates of the glass cell ($73\,\mathrm{cm}^2$; $5 \times 10^{-12}\,\frac{\mathrm{mbar}}{\mathrm{cm}^2}\frac{\mathrm{l}}{\mathrm{s}}$) [90], titanium flange ($38\,\mathrm{cm}^2$; $7 \times 10^{-12}\,\frac{\mathrm{mbar}}{\mathrm{cm}^2}\frac{\mathrm{l}}{\mathrm{s}}$) and 316L austenitic stainless steel after low temperature bakeout ($680\,\mathrm{cm}^2$; $< 8 \times 10^{-13}\,\frac{\mathrm{mbar}}{\mathrm{cm}^2}\frac{\mathrm{l}}{\mathrm{s}}$) [91]. The achievable pressure

[2] Hellma, 402.013-OG
[3] Epoxy Technology, EPO-TEK H77T
[4] Grade 5, 6Al-4V
[5] Epoxy Technology, EPO-TEK, 353ND
[6] UGQ optics, FQP-25
[7] Typically around 465 m/s for air at room temperature.

P can be estimated by the ratio of gas load Q[8] to pumping speed S [92]:

$$P = \frac{Q}{S} = \frac{\overbrace{2.9\times10^{-9}}^{Q_{\text{diff.pumping}}} + \overbrace{1.9\times10^{-7}}^{Q_{316\text{L}}} + \overbrace{3.7\times10^{-8}}^{Q_{\text{glass cell}}} + \overbrace{2.7\times10^{-8}}^{Q_{\text{titanium}}}}{\underbrace{25}_{S_{25\text{l}}}} \text{ mbar} \approx 1{\times}10^{-10}\,\text{mbar}\,. \tag{2.1.3}$$

Furthermore, some parts of the vacuum components had been pre-baked at 250 °C in a vacuum oven for 48 h before the actual assemblage of the vacuum system as the bakeout temperature of the vacuum system is limited to 150 °C by the glued cell if one wants to avoid big temperature gradients during the bakeout.

The pressure in the oven section reaches 1×10^{-7} mbar at room temperature and typically 2×10^{-7} mbar at oven temperature of 430 °C whereas the science chamber stays at 1.3×10^{-10} mbar at room temperature and goes up to 5×10^{-10} mbar with a running oven and matches well with the theoretical estimation. The pressure in the science chamber is maintained by an ion pump as well as by non-evaporable getter materials[9] (not operating yet) which, once activated, begin to absorb gases that are otherwise hard to remove with ion pumps (e.g. H_2).

2.2 The strontium effusive source

Atomic, molecular and ion beam sources are of great importance in modern atomic physics. Only through efficient production of the particles of interest, precision experiments can be carried out with the smallest amounts of atoms and molecules. In order to be able to work on atoms or molecules in a free and completely isolated environment, suitable beam-based sources are necessary. For this purpose, atomic or molecular beams are used which, after leaving the source chamber, have basically no interaction with external matter and also have few intra-beam collisions.

Apart from rubidium and potassium experiments using atomic dispensers, the majority of cold atom experiments rely on effusive sources. Such ovens are fairly simple in terms of overall design and represent a comparatively efficient class of atomic sources. [93]. They consist of an evacuated chamber containing a solid sample of the specific atomic species to be investigated. This reservoir has a small orifice towards the experiment's main chamber through which the vapor diffuses. The flux of atoms leaving the oven can be controlled by changing the oven temperature and thus the vapor pressure inside the reservoir, until the temperature

[8] The gas load is the rate at which molecules from a specific source enter into the chamber's gas phase.

[9] SAES Getters, CapaciTorr D 200

reaches the boiling point. Alternatively, beams of Strontium can also be generated using laser ablation at 405 nm as was recently demonstrated in [94]

The following section will briefly discuss the theoretical principles of operation of effusive ovens and present the source developed for the new Strontium experiment.

2.2.1 Basic kinetic gas theory

As hinted on above, the generation of an atomic beam from an effusive source relies on the principle of vaporization of a solid (or liquid) substance. In a closed system, a solid will evaporate until its vapor phase reaches a thermodynamic equilibrium with the condensed component and the walls of the surrounding enclosure. The pressure that the vapor exerts in this equilibrium is called the vapor pressure. The resulting vapor pressure p can be estimated with the Antoine equation as a function of the source temperature T using [95]:

$$\log_{10}\left(\frac{p(T)}{\mathrm{Pa}}\right) = 5.006 + A + BT^{-1} + C\log T\,, \tag{2.2.1}$$

where $A = 9.226$, $B = -8572$ and $C = -1.1926$ for strontium (see figure 2.2.1a).

Gaseous strontium atoms in the source experience collisions with each other. The average distance a particle travels between two of these events is called the interatomic collisional mean free path $\tilde{\lambda}$. Assuming an ideal gas of identical particles with a Maxwell-Boltzmann velocity distribution, $\tilde{\lambda}$ is then given by [96]

$$\tilde{\lambda}(T) = \frac{k_B\,T}{\sqrt{2}\sigma\,p(T)}\,, \tag{2.2.2}$$

where T is the temperature and σ the inter-species elastic collisional cross-section $\sigma = 3 \cdot 10^{-}13\,\mathrm{cm}^2$ [97]. Many authors refer to the *Van-der-Waals* diameter $\sigma = \pi d_{\mathrm{VdW}}^2$ or even to the atomic radius, which are typically used in the context of bonding and inter-atomic interaction potentials. However, dimensions from kinetic gas theory usually differ from these [98].

An enclosed volume of thermalized gas as inside of effusive sources, the velocity distribution is given by the 3D Maxwell-Boltzmann distribution function:

$$\rho_{th}(v,T) = 4\pi\left(\frac{m}{2\pi k_{\mathrm{B}}T}\right)^{3/2} v^2 \exp\left(-\frac{mv^2}{2k_{\mathrm{B}}T}\right)\,. \tag{2.2.3}$$

Any statistical property of the gas can be determined by taking the appropriate

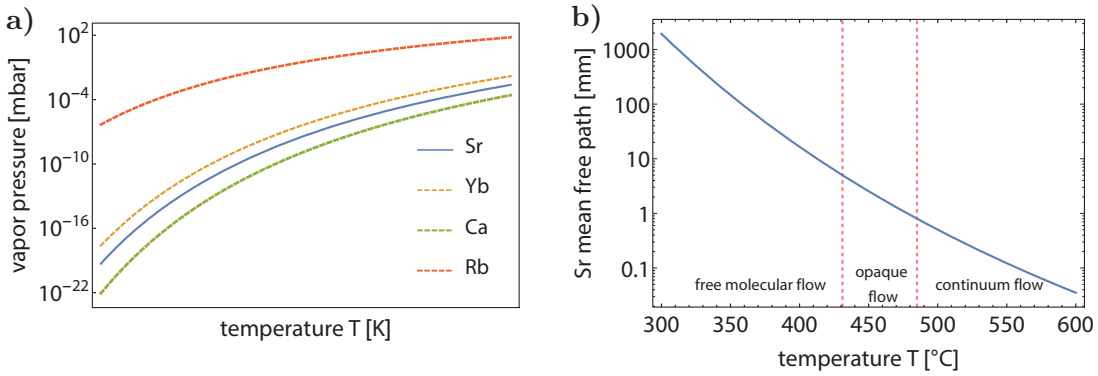

Figure 2.2.1: a) Calculated vapor pressure for several elements often used in cold atom experiments. b) Temperature dependent mean free path of strontium. The dashed lines indicate the temperatures at which the mean free path of strontium is on the same order than the first orifice diameter and the orifice length.

moment of the distribution, as for example the mean velocity:

$$\overline{v}(T) = \sqrt{\frac{8k_{\mathrm{B}}T}{\pi m}}\,. \tag{2.2.4}$$

However, the velocity distribution function naturally changes for a directed thermal beam as generated by an effusive source, for example. For a directed thermal beam, the longitudinal velocity distribution is skewed to be higher than the distribution of the corresponding gas in a reservoir [99, 100] and reads

$$\rho_{beam}(v,T) = \frac{1}{2}\left(\frac{m}{k_{\mathrm{B}}T}\right)^{2} v^{3} \exp\left(-\frac{mv^{2}}{2k_{\mathrm{B}}T}\right)\,. \tag{2.2.5}$$

The most probable velocity is thus:

$$\overline{v}'(T) = \frac{3}{4}\sqrt{\frac{2\pi k_{\mathrm{B}}T}{m}}\,. \tag{2.2.6}$$

An intuitive explanation for the additional dependence on v in equation 2.2.5 compared to the standard 3D Maxwell-Boltzmann distribution is that a particle at a higher velocity has a higher chance of finding an escape trajectory during a given time interval.

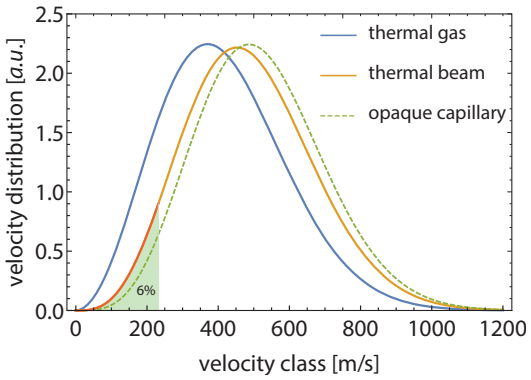

Figure 2.2.2: Calculated strontium velocity distributions at 450 °C for a thermal gas, thermal beam and opaque capillary [101, 102]. The shaded region indicates the fraction of the thermal beam distribution trapped by the Zeeman slower.

2.2.2 Terminology of effusive sources

The creation of gaseous flow from a small orifice of a heated cell has been first investigated by Martin Knudsen [103, 104]. His early pioneering works on this subject have lead to that almost all sorts of isotherm beam sources based on an effusive gas flux, e. g. the molecular beam epitaxy, are called *Knudsen cell*.

The underlying assumption of the Knudsen theory is that the ratio between the reservoir surface and the oven orifice is large, i. e. that the system can be treated as almost closed. There is a dynamic equilibrium at the surface of the granulate between diffusion and evaporation. Thus, the atomic flux exiting the orifice depends only on the oven temperature and the gas pressure. The angular distribution is described by an intensity function $I(\theta)$ which has units of atom per steradian per second. The angle θ is the angle from the normal of the exit orifice. By assuming that the opening is circular and the angular distribution is rotationally symmetric, then the intensity function is separable:

$$I(\theta, T) = I_0(T) j(\theta) \ , \tag{2.2.7}$$

where $I_0(T)$ is the particle flow along the beam axis and $j(\theta)$ the normalized angle distribution function. The different flow regimes described in the following mainly manifest themselves in the form of different angular distribution functions $j(\theta)$.

Flow regimes

When planning a new oven, one has to be aware of the different flow regimes as they play a key role in the formation of the atomic beam. Many authors refer to the so-called *Knudsen number* in order to distinguish the regimes. This classification, however, introduces unnecessary complexity in the case a flow through a tube ,i. e. a typical effusive source. The different regimes are therefore better classified by

comparing the mean free path to the collimation tube length L and diameter d:

$$\begin{aligned} \tilde{\lambda} > L: &\quad \text{transparent/free molecular flow} \\ L > \tilde{\lambda} > d: &\quad \text{opaque/transitional flow} \\ \tilde{\lambda} < d: &\quad \text{viscous/continuum flow} \end{aligned} \tag{2.2.8}$$

Transparent, free molecular or Knudsen flow occurs when the mean free path is much larger than the orifice size, such that collisions between atoms are virtually absent – therefore, the gas can be treated as non-interacting. Due to the geometry of a tube orifice, direct escape trajectories are increasingly constrained with decreasing aspect ratio d/L. Furthermore, only diffuse and non-reflective scattering with the walls is assumed [102, 105, 106], which allows to describe a tube orifice as a cosine-emitter so that $j(\theta) = \pi^{-1} \cos\theta$. A long channel in the free molecular flow leads to a collimated atomic beam without diminishing the axial beam intensity.

If the pressure increases and the mean free path is less than the length of the tube, the beam degenerates to an opaque (or turbulent) flow. This regime occurs as atom-atom collisions inside the channel are more frequent, resulting in beam shape broadening with a larger FWHM than the free molecular flow [102, 107–109]. Phenomenologically, the beam shape is composed of three contributions: First, the fraction of atoms passing the channel without any collision; second, the contribution from atoms scattered by gas-gas collisions increases with increasing θ; third, at large angles, gas-wall collisions near the tube's outlet dominate, which can be then described by the cosine-emmiter theory of a transparent flow. However, the opaque flow is theoretically hard to describe. Even when the source pressure implies an opaque flow, the mean free path along the tube increases as the number density decreases and the free molecular flow condition will satisfied at some point along the tube. It should also be mentioned that the boundaries between the flux regimes presented here are not sharp, but gradual.

Finally, if the mean free path drops below the tube diameter d, the so-called viscous flow occurs which is characterized by an ordered flow of gas. This has the consequence that the total beam flux has a stronger dependence on the reservoir's pressure and thus grows at a faster rate [110]. Moreover, a depletion of the low velocity fraction of the Maxwell-Boltzmann distribution [111] can be observed.

2.2.3 Design of a new strontium oven

The major design principles of the oven in the following are on based the ones presented in [112] but have been modified in order to yield a more efficient and less complex oven assembly. Besides the goal of a compact effusive source, the design guideline was to reduce the distance between the source and the MOT

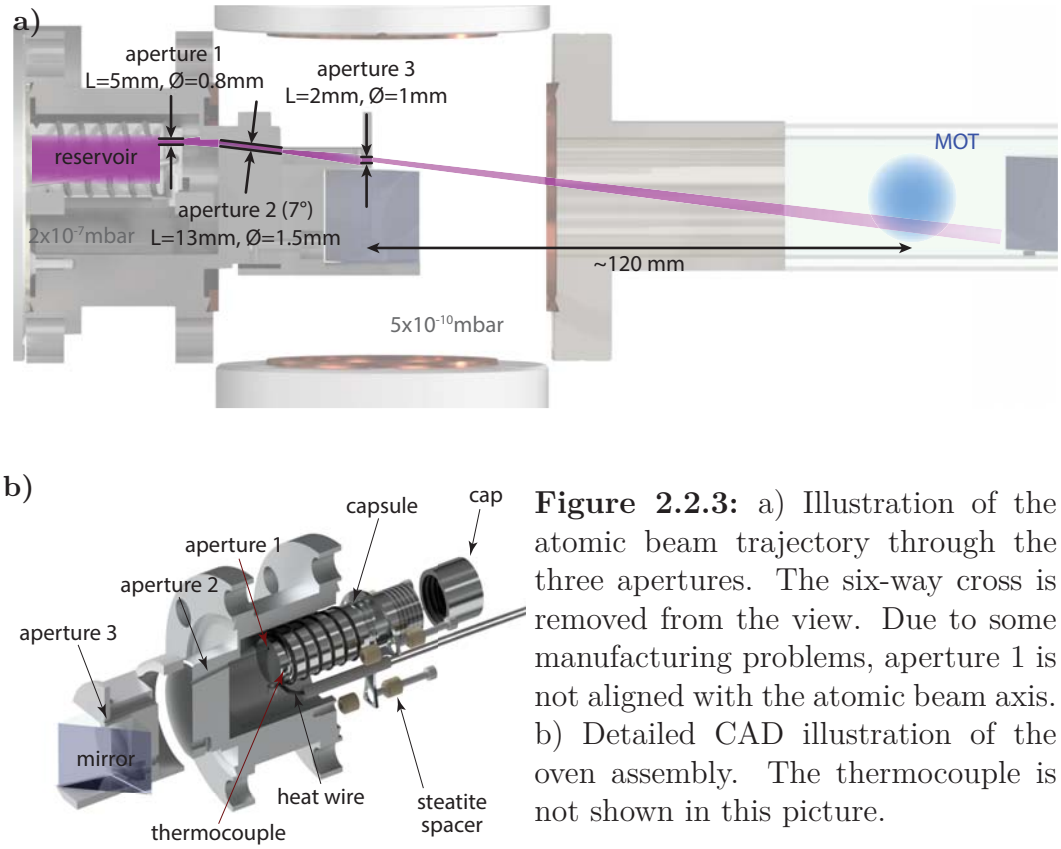

Figure 2.2.3: a) Illustration of the atomic beam trajectory through the three apertures. The six-way cross is removed from the view. Due to some manufacturing problems, aperture 1 is not aligned with the atomic beam axis. b) Detailed CAD illustration of the oven assembly. The thermocouple is not shown in this picture.

region. This is important if one aims to maximize the MOT loading efficiency as otherwise the atomic beam size diameter can exceed MOT trapping radius. A schematic overview of the concept can be found in figure 2.2.3b. The reservoir is a stainless steel capsule containing up to 2.5 g of solid strontium[10]. After loading the capsule under a protective argon atmosphere, it can be closed by screwing a cap onto its end. The capsule's filling quantity should allow a non-stop operation of the oven at 450 °C for about 5 years.

A thermocouple is attached close to the oven's outlet and allows to measure the temperature. The heating wire [11] is welded into small grooves that were milled in the capsule in order to improve the thermal contact. The capsule is attached to the stainless steel flange via insulating steatite spacers.

The directionality of the atomic beam is set by a combination of several aper-

[10]Sigma Aldrich, 441899-5G
[11]ThermoExpert Deutschland GmbH; 2-wire mineral insulated heatingwire

tures. The first orifice is the capsule outlet itself which has a diameter of 0.8 mm and a length of 5 mm, whereas the second orifice, which also serves as the differential pumping tube, has a diameter of 1.5 mm and a length of 12 mm. The second aperture is also tilted by 7° towards the bottom. This angle has the advantage that atomic beam does not hit the entire mirror surface inside the glass cell, but rather just its bottom if not even the spacing between the mirror and glass cell. However, as can be seen in figure 2.2.3a, the first orifice and the tilted second aperture are not aligned so that only an off-axis fraction of the angle distribution after the capsule outlet passes onto the second aperture.

A third aperture is introduced by a steel mount that mainly holds the second in-vacuum prism mirror, and is located right above the mirror. The oven had been assembled in a glove box under an inert argon atmosphere in order to avoid the oxidation of the strontium granulate before it has been attached to main vacuum system.

It should be mentioned at this point that the capsule outlet's dimensions might lead to an opaque instead of a free molecular flow, as indicated in figure 2.2.1b. This assumption is based on the calculation of the mean free path with the molecular elastic collisional cross-section [97] instead of the using the Van-der-Waals diameter as done in [112]. The latter also states that the overall beam intensity and the divergence angle does not match with free molecular flow theory, what the authors explain by a misalignment of the their microtubes. Another possible way of explaining this discrepancy is that their effusive source works in the opaque regime. As a result, the oven design presented in this section might work in the opaque regime for a typical working temperature of 450 °C and could even transition into a viscous flow if the experiment works with fermionic strontium.

Thermal budget

The figure 2.2.4b shows the measurement of the electrical power consumption of the oven for different steady-state temperatures. A simple model based on losses by heat conduction and thermal radiation can be applied in order to be able to understand the outcome of the measurement in a quantitative fashion. The heat conduction of a metallic rod obeys the following equation:

$$\mathrm{d}_t Q_c = P_c = \frac{k\sigma\,(T_1 - T_{amb})}{L}\,, \tag{2.2.9}$$

where k is the thermal conductivity, σ is the cross section, T_{amb} is the ambient room temperature (25 °C) and L the length of the rod. The radiation heat transfer

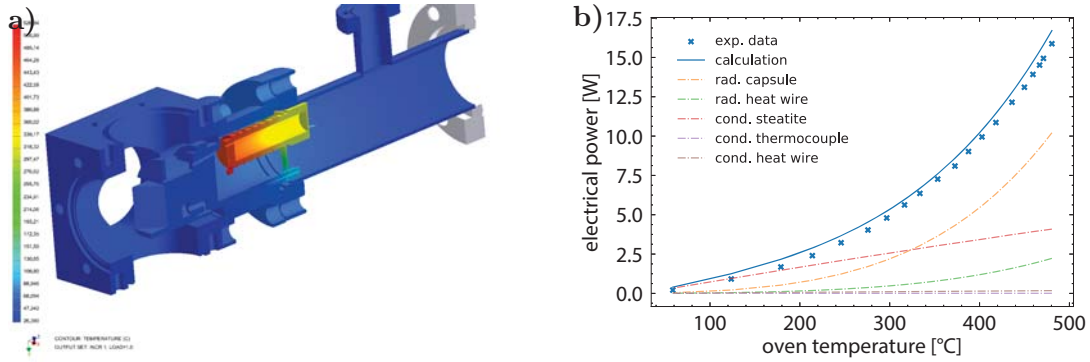

Figure 2.2.4: a) FEM thermal simulation of the oven assembly at an electrical power of 15 W. b) Measurement of the electrical power consumption vs. the oven temperature. The dashed lines show the different heat loss contributions.

component	A [mm^2]	L [mm]	σ [mm^2]	k [W/(m · K)]	ϵ (149–816 °C)
capsule	3000	–	–	–	0.15 – 0.49
heat wire	$^2/_3 \cdot 1000$	200	0.79	391.1	0.15 – 0.49
thermocouple	–	200	0.07	20	–
steatite	–	5	5.4	3	–
heat shield	5000	–	–	–	0.15 – 0.49

Table 2.1: Oven properties for the calculation of its electrical power intake. A – surface area; L – length; σ – cross section; k – thermal conductivity; ϵ – emissivity.

between two concentric cylinders with radii r_1 and r_2 reads as

$$P_r = \frac{A_1 \sigma \left(T_1^4 - T_2^4\right)}{\frac{1}{\epsilon_1} + \frac{1-\epsilon_2}{\epsilon_2}\left(\frac{r_1}{r_2}\right)} \tag{2.2.10}$$

with A_1 and ϵ_1 being the surface and the emissivity of the inner cylinder and ϵ_2 the emissivity of the outer cylinder.

In a simplified model, the different loss contributions from the thermal conductance of the heat wire, thermocouple and the steatite spacer are summed, as well as the losses via thermal radiation of the capsule and heat wire. The values used for the calculation can be found in table 2.1. The figure 2.2.4b shows the electrical power consumption depending on the measured equilibrium temperature. The simplified calculation is in good agreement with the experimental results. If one

wants to improve the electrical power intake of the oven, a way to go about it would be to reduce the contact cross-section of the steatite spacers and to coat the inside of the flange/heat shield with a thin layer of gold, which can be realized with the available equipment at the physics department of the École Normale Supérieure.

From the FEM heat simulation in figure 2.2.4a it can be also seen that the capsule shows an increasing temperature towards the capsule's outlet which potentially prevents its clogging.

2.3 Optical access and magnetic quadrupole fields

The realization of a magneto-optical trap requires, as its name suggests, a magnetic gradient in addition to optical beams. In order to create this gradient and additional bias fields in along all spatial directions, four pairs of coils are placed around the science cell. One of these pairs is intended to generate a gradient by having the current flow in opposite directions in each coil. In the other three pairs, the currents are parallel and thus create a magnetic field bias field at the position of the atoms. This offset bias field has several uses: it makes it possible to eliminate any residual (permanent) stray DC fields and to set quantization axis.

In order to obtain a high gradient while keeping the current as low as possible, it is necessary to position the coils as close as possible to the area of interest, that is to say to the location where the atomic cloud is located. This constraint places strong restrictions on the size and shape of the coils since it is is necessary to preserve the optical access to the cell and the cavity and to accommodate other elements of the assembly.

The optimal configuration to generate a field with a homogeneous magnetic gradient is the anti-Helmholtz configuration[12].

2.3.1 Magnetic coil design

Besides six offset coils, the coil assembly consists of a pair of copper MOT coils, each having 60 turns. As the glass cell and its titanium flange have to be passed through one of the coils, a rectangular shape of the coils were chosen with inner and outer dimensions of $40 \times 40\,\mathrm{mm}$ and $70 \times 70\,\mathrm{mm}$, respectively. All coils are mounted on a massive copper support structure which is slotted to reduce Foucault currents. Since each coil produces approximately 35 W of heat during operation at $I = 25\,\mathrm{A}$, the copper mount incorporates water circulation to cool the assembly with an external chiller.

[12] In the anti-Helmholtz configuration, two identical coils are placed parallel to a distance from each other equal to their radius.

As the magnetic field of a rectangular coil is different from the field of standard circular coil, the modified equations are summarized below. For the case of a square current loop of side length L, the exact magnetic field can be derived by integrating the *Biot-Savart* law. The result for the on-axis field in the x-z-plane reads ([113] and references therein):

$$\begin{aligned} B_x &= \frac{\mu_0 I}{4\pi} \sum_{a=1}^{4} \left[\frac{(-1)^{a+1} z}{r_a [r_a + d_a]} \right] \\ B_z &= \frac{\mu_0 I}{4\pi} \sum_{a=1}^{4} \left[\frac{(-1)^{a} d_a}{r_a [r_a + (-1)^{a+1} C_a]} - \frac{C_a}{r_a [r_a + d_a]} \right] \end{aligned} \tag{2.3.1}$$

with

$$\begin{aligned} C_1 &= -C_4 = L + x & \qquad d_1 &= -d_2 = L \\ C_2 &= -C_3 = L - x & \qquad d_3 &= -d_4 = -L \end{aligned}$$

and

$$\begin{aligned} r_1 &= r_4 = \sqrt{(L+x)^2 + L^2 + z^2} \\ r_2 &= r_3 = \sqrt{(L-x)^2 + L^2 + z^2}\,. \end{aligned}$$

The MOT coil configuration and the resulting magnetic field is shown in figure 2.3.1 for a typical current of $I = 25\,\mathrm{A}$. The magnetic field gradient at the MOT position is on the order of $35\,{}^{\mathrm{G}}/_{\mathrm{cm}}$. For a saturation parameter $s_0 = {}^{I_{\mathrm{beam}}}/_{I_{\mathrm{sat}}} \approx 0.25$ and a laser beam diameter of $2w_{\mathrm{L}} \approx 1\,\mathrm{cm}$, the resulting MOT capture velocity [13] can be calculated, yielding [114]

$$v_{\mathrm{MOT}} = \sqrt{2w_{\mathrm{L}} \frac{\hbar k \Gamma}{2m} \frac{s_0}{1+s_0}} \approx 48\,{}^{\mathrm{m}}/_{\mathrm{s}}\,. \tag{2.3.2}$$

As the blue transition in strontium has a relatively broad linewidth, a large magnetic field gradient is desirable to load the trap at high rate. However, due to the MOT capture velocity and the maximum declaration of the molasses (equation 2.3.5), a maximum field gradient can be estimate. The upper bound can be calculated via

$$\frac{\partial B}{\partial r} \ll \frac{\hbar k}{\mu_{\mathrm{B}}} \frac{a_{\max}}{v_{\mathrm{MOT}}}\,, \tag{2.3.3}$$

yielding a value of $60\,{}^{\mathrm{G}}/_{\mathrm{cm}}$ for the coil configuration presented here.

[13] i. e. the velocity where the energy dissipated by a trapping beam matches the atom's kinetic energy

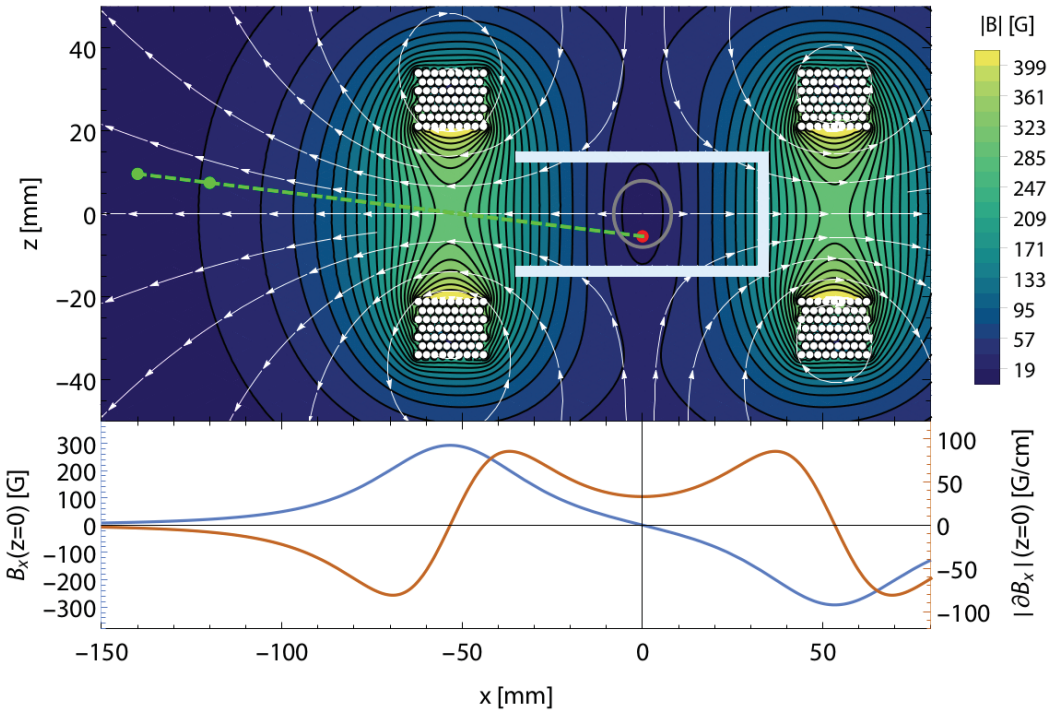

Figure 2.3.1: Shown is the magnetic field for $I = 25\,\mathrm{A}$ per coil. *Top*: Contour plot of the magnetic field in the x-z-plane. Gray circle: MOT trapping region; Green dashed line: atomic jet; Green dots: position of the two apertures. *Bottom:* Cut through the B-field x-axis.

Finally, as the MOT coils also serve as Zeeman slower and a large magnetic field amplitude is required to have sufficiently high cooling efficiency, the coils are not in a perfect Helmholtz-configuration but separated by $100\,\mathrm{mm} > 2R \approx 60\,\mathrm{mm}$. This allows to increase the B-flied amplitude while having a sufficiently small MOT field gradient.

2.3.2 Zeeman slowing

A weakly collimated atomic jet emitted from the oven can be slowed down by spontaneous or radiation pressure force of a contra-propagating laser. Due to the Doppler effect, the radiation pressure force is only efficient to capture atoms with velocities of a few tens of meters per second. The velocity distribution of the jet, by contrast, extends over several hundreds of meters per second, thus the radiation pressure force is not able to efficiently slow down a large part of the atoms of the jet.

Brief résumé on Zeeman slowing

The limited capture velocity makes the loading from background gas quiet inefficient. At room temperature, the mean velocity of rubidium gas is about 280m/s.

As the elevated temperature of the effusive oven leads to an atomic velocity distribution that lies mainly above the MOT capture velocity, a velocity matching element is required. A common method for increasing the capturing range of MOT makes use of the change of the atomic level spacing experienced by an atom in a magnetic field, B. In the Zeeman regime, the resulting detuning for an atom of speed $v(x)$ reads

$$\delta(x) = \Delta - \mathbf{k} \cdot \mathbf{v(x)} - \frac{\mu' \mathbf{B(x)}}{\hbar}\,, \tag{2.3.4}$$

where $\mu' = (g_e M_e - g_g M_g)\mu_B$ is the transition's magnetic moment, $g_{g,e}$ the Landé g-factors of the ground and excited states and $M_{g,e}$ the magnetic quantum number.

The apparatus to accomplish, known as a Zeeman slower, was first proposed and demonstrated [6] by Phillips and co-workers and consists of coil configuration that creates a tapered B-field. Any atoms entering the Zeeman slower below a maximum capture velocity v_i will eventually be in resonance with a counter-propagating laser (*Zeeman laser*) beam, depending on their initial velocity, and picked up in the slowing process. By appropriate tuning of the B-field, and hence of the Zeeman shift, the Doppler shift may be continuously compensated while the atoms travel against the laser beam, resulting in a constant detuning Δ.

Based on the resonance condition in equation 2.3.4, the key parameters of a Zeeman slower can be derived. First, the deceleration a reads as

$$a = \epsilon a_{max} = \epsilon \cdot \frac{2\pi\hbar}{m\Delta}\frac{\Gamma}{2}\,, \tag{2.3.5}$$

where $\epsilon \in [0, 1)$ denotes a stability factor, which scales with $s_0/(1 + s_0)$ and is constrained by the available slowing beam power. Now, the expression for the deceleration length can be derived, which is the required distance to slow down the atoms to the desired MOT capture velocity

$$L(a) = \frac{v_i^2 - v_{\mathrm{MOT}}^2}{2 \cdot a}\,. \tag{2.3.6}$$

the velocity at position x is given by

$$v(x) = \sqrt{v_i^2 - 2a \cdot x}\,. \tag{2.3.7}$$

Combining equation 2.3.4 and equation 2.3.7 gives the ideal field profile to con-

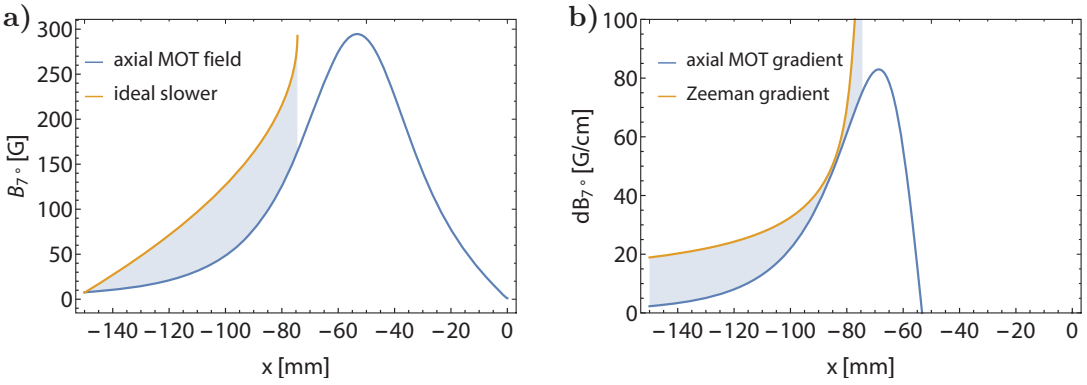

Figure 2.3.2: a) Ideal shape of a Zeeman slower and calculated magnetic field of the MOT coils for $I = 25\,\mathrm{A}$, $\epsilon = 0.38$ and $\Delta = -2\pi \times 17\gamma$. b) Comparison between the slope of the ideal Zeeman slower and slope of the calculated magnetic field.

stantly compensate for the Doppler shift:

$$\begin{aligned} B(x) &= \frac{\hbar}{\mu'}\Delta + \frac{\hbar}{\mu'}kv_i\sqrt{1-\left(1-\frac{v_{\mathrm{MOT}}^2}{v_i^2}\right)\frac{x}{L}} \\ &= B_{\mathrm{bias}} + B_0\sqrt{1-\left(1-\frac{v_{\mathrm{MOT}}^2}{v_i^2}\right)\frac{x}{L}} \end{aligned} \tag{2.3.8}$$

From this equation it becomes clear that a large ϵ leads to a short Zeeman slower. As the slower becomes shorter with the exit speed of the oven remaining constant, the slower's tolerance with respect to detuning due to field imperfections becomes smaller.

MOT-integrated *(virtual)* Zeeman slower

Similiar to experiment presented in [114], the MOT coils in this design are a multipurpose tool. As their symmetry axis is quasi-parallel to the atomic beam axis up to the 7° angle, the strong magnetic field outside the coil pair can be used as a virtual Zeeman slower without adding any dedicated coils, hence reducing the complexity and heat intake of the experiment.

Behind the last oven aperture, the atoms are slowed similarly to an ideal 'increasing field' Zeeman slower, where the velocity follows $v(z) = \mu_{\mathrm{B}}B(z)/(\hbar k)$. Atoms with initial velocities $v_0 < v_{\mathrm{c}} = \mu_{\mathrm{B}}B_0/(\hbar k) + v_{\mathrm{MOT}}$ should be therefore slowed. figure 2.3.2a shows the calculated magnetic field along the 7° trajectory. At a coil current of $I = 25\,\mathrm{A}$ the magnetic field amplitude between the entrance

and exit of the Zeeman slower is 285 G, which results in a maximum capture velocity of $v_c = 232^{\mathrm{m}}/\mathrm{s}$. The magnetic field at the slower entrance has an offset of 7.7 G, leading to a required laser detuning of $\Delta = -2\pi \times 17\gamma$ (equation 2.3.8).

For stable operation of the Zeeman slower, it is furthermore important to find the minimum stability parameter ϵ via the condition

$$|\partial_x B_{\mathrm{exp}}(x)| \leq |\partial_x B_{\mathrm{ideal}}(x)| \ . \tag{2.3.9}$$

From figure 2.3.2b, it can be seen that this holds for $\epsilon \geq 0.38$ or $s_0 \geq 0.61$.

This Zeeman slower configuration should be capable trap up to 6 % of the atomic jet's velocity distribution at 450 °C. Nevertheless, it needs to be mentioned that, due to the ${}^3P_1 \rightarrow {}^1D_2$ decay channel with a branching ratio of 1 : 20 000 [61], atom losses of up to 60 % from the Zeeman slowing process can be expected [115]. In addition, the beam divergence is going to increase during the slowing process.

2.4 The strontium laser system

In order to perform laser cooling, optical trapping and imaging of the atoms using the transitions mentioned earlier, coherent beams of light of appropriate frequencies and optical intensities need to be generated in a controllable and tunable way. The essential components are presented on the following pages.

2.4.1 The first MOT stage

The blue laser system

A commercial master diode laser[14] in Littrow-configuration is stabilized a Doppler-free absorption signal of the ${}^1\mathrm{S}_0 \rightarrow {}^1\mathrm{P}_1$ transition, amplified by injection locking two slave diodes[15] and then further used as probe. Instead of a heated spectroscopy cell, a hollow cathode discharge cell[16] is used which is powered by a low-noise high-voltage DC-DC converter[17]. The slave laser frequencies are shifted to the required detunings by means of single pass acousto-optical modulators (AOM) which also serve as fast switches that will eventually be complemented by mechanical shutters to ensure the total suppression of stray light in the optical fibers leading to the atoms.

The first slave laser is shifted by −30 MHz and delivers the optical power for the

[14] MOGLabs LDL; Nichia NDBA116T diode
[15] Nichia NDB4216E
[16] Hamamatsu L2783-38NE-SR
[17] ISEG CPp 05 206 24 05 module

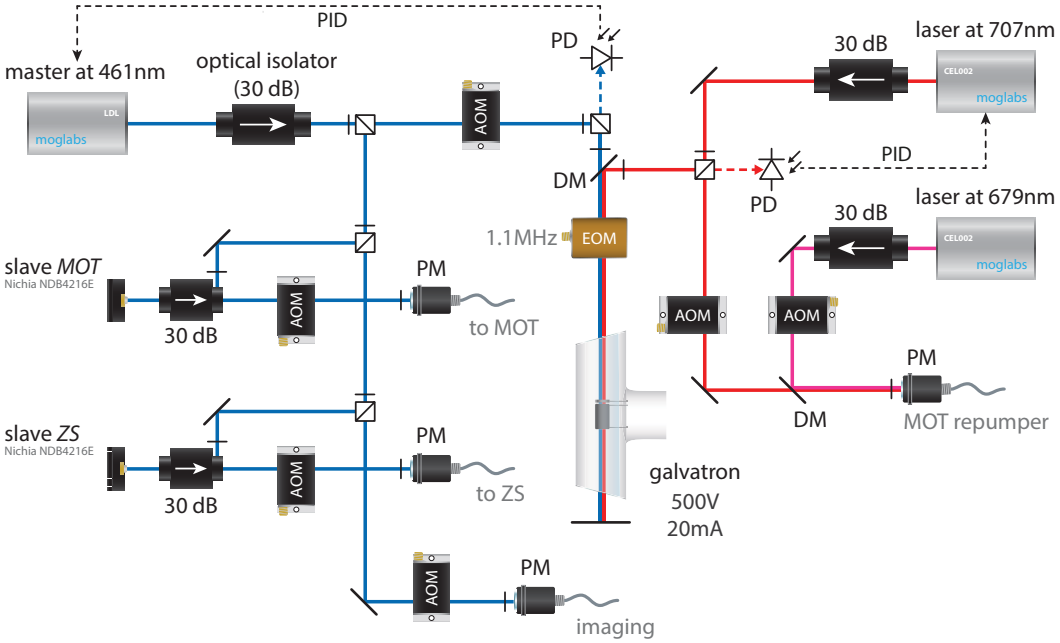

Figure 2.4.1: Simplified scheme of the blue MOT laser system. PM - polarization maintaining fiber; DM - dichroic mirror; ZS - Zeeman slower.

3D MOT. The beam is divided by a commercial fiber splitter[18] before the light is being sent to the main optical table. The second slave laser serves as cooling laser for the Zeeman slower and is shifted by $-550\,\mathrm{MHz}$. Over the course of this thesis, it turned out that the optical power of the MOT laser is not sufficient to exploit the full potential of the MOT cooling and trapping. Alternatively, injection locking a low-cost multi-mode and high-power laser diode (so as published in [116]) has been tested, but no appropriate model compatible with the 5.6 mm laser diode socket setup had been found as their emission spectrum merely touched the required wavelength of 461 nm.

Repumpers

Even though several repumping transitions of distinct wavelengths are available and accessible with standard diode lasers, the usual repumping scheme on the $(5s5p)\,^3P_J \rightarrow (5s6s)^3S_1$ transitions was chosen. Not only can both wavelengths be easily generated with ample power, but these lasers could be also useful tools for advanced cQED schemes as in the case of the 'atomic drain' [117]. The repump transitions at 679 nm and 707 nm have natural linewidths $\gamma = 1.4\,\mathrm{MHz}$ and

[18] Evanescent Optics; spliceless PM coupler 1x3 array

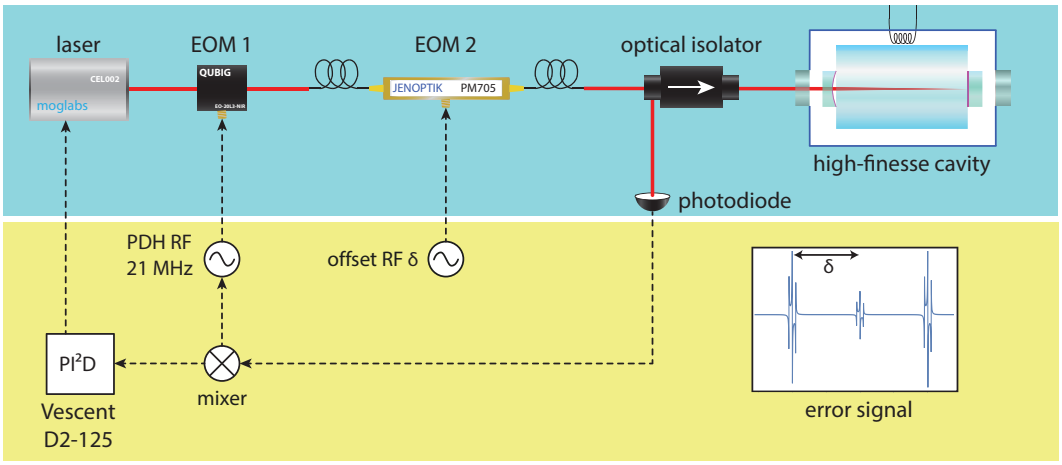

Figure 2.4.2: Dual-sideband locking scheme.

$\gamma = 6.4\,\mathrm{MHz}$, respectively. Both the 679 nm and 707 nm consist of commercial diode laser[19]. While the 679 nm laser is used in free-running mode, the second repumper is stabilized on the same hollow cathode lamp as the 461 nm laser [118].

2.4.2 The second MOT stage and clock laser system

A diode laser in cateye configuration[20] at 689 nm and a diode laser in Littrow-type configuration with an extended cavity[21] at 698 nm had been purchased, both mounted on the same breadboard as the commercial high-finesse cavity[22]. Each laser is protected with a 60 dB optical isolator. At the time of writing of this thesis, the 689 nm system had already been finished and work on the other setup was underway.

As external cavity diode lasers in general have broad emission spectral linewidths on the order of a few MHz, it is required to further reduce their linewidths for some demanding applications. One of these applications is to perform cooling on the $^1S_0 \rightarrow^3 P_1$ transition with a narrow linewidth of $\gamma \approx 7\,\mathrm{kHz}$ and potentially also spectroscopy of the $^1S_0 \rightarrow^3 P_0$ clock transition. Both require laser linewidth on the sub-kHz level. The prevalent technique is the stabilization to an external high-finesse Fabry-Perot cavity with a resonance linewidth significantly narrower than the laser linewidth. This method has led to outstanding laser linewidth reduction down to the mHz-level [119].

[19] MOGLabs CEL002
[20] MOGLabs CEL002
[21] Toptica DLpro, narrow linewidth option
[22] Stable Laser Systems

For that purpose, both lasers are locked on a cavity and the beams are superimposed and split by dichroic mirrors. After coupling into the cavity, the back-reflection is picked up at a Faraday isolator and made incident on a photodiode. The error-signal extracted from the resulting signal is fed back to the laser's piezo- and current-modulation ports. To provide proper locking, a double integrator servo controller is used[23] and the optical isolators between the EOM and cavity should reduce any etalon effect. As the cavity finesse is relatively low, a laser setup including a pre-stabilization cavity was not considered and was found to be unnecessary.

It is common practice in cold atom experiments that the frequency of a laser locked to the fundamental mode of an optical resonator is tuned with an AOM to reach a specific frequency, like for example the atomic transition frequency. The drawback of this scheme is the small modulation bandwidth of the AOM, which ultimately limits the tuning range of the AOM of the lock.

A powerful alternative is the dual-sideband locking method. It incorporates a high bandwidth electro-optical modulator (EOM) to generate offset sidebands and a second EOM to generate the locking sidebands on each offset sideband. The working principle of this technique is shown in figure 2.4.2. This method benefits from the high RF bandwidth of fiber-based EOMs reaching a few GHz, which have several advantages over free-space bulk EOMs for performant locks [120]. Even though this technique can be realized with a single EOM, using two frequency generators at different frequency and combining them with a tee, the offset- and PDH-frequencies are applied to two different EOMs on the present experiment.

The first EOM generating the PDH signal is a bulk EOM[24] modulated at 21 MHz. The offset sidebands are then created by a fiber-based EOM[25]. Before being coupled into a PM fiber splitter[26], the beam passes a double-pass AOM, which allows to scan the laser frequency for realizing the SWAP-MOT method [121].

The ultra stable reference cavity

The resonator is a commercial design provided by Stable Laser Systems and consists of a 10 cm long ultralow-expansion glass spacer[27] and optically bonded mirrors. It's finesse was found to be $\sim 3.4 \times 10^4$ using cavity ring-down spectroscopy. This translates into a linewidth (FWHM) of around 44 kHz. The cavity is mounted in a thermally controlled vacuum chamber with a pressure below 1×10^{-6}mbar.

[23] Vescent D2-125 Laser Servo
[24] QUBIG, EO-20L3-NIR
[25] Jenoptik, PM705
[26] Evanescent Optics; spliceless PM coupler 1x3 array
[27] Corning ULE, thermal expansion coefficient $|\alpha| < 10^{-8}\,\mathrm{K}^{-1}$

quantity	expression	SLS cavity
mirror spacing	L	10 cm
mirror reflectivity	$\mathcal{R}$	99.99 %
radius of curvature	r	50 cm / ∞
finesse	$\mathcal{F} = \frac{\pi\sqrt{R-2\alpha L}}{1-R+2\alpha L}$	$\sim 3.4 \times 10^4$
FSR	$\Delta\nu_{\mathrm{FSR}} = \frac{c}{2L}$	1.49 GHz
linewidth (FWHM)	$\delta\nu = \frac{\Delta\nu_{\mathrm{FSR}}}{\mathcal{F}}$	44 kHz

Table 2.2: Characteristics of the *Stable Laser Systems* ULE cavity.

A thermal heat shield, proper isolation stage against vibrations or an acoustic isolation box, however, have not been installed yet.

In order to keep the intra-cavity power below 1 W to avoid any optically induced damage of the mirror coatings, the power of the incident beam is kept below $\sim$ 50 µW [122]. The coupling efficiency α of the laser beam to the resonator's fundamental mode can be estimated by measuring the intensity of the higher order transverse modes and relating it to the former. Even though this technique is not precise for a high-finesse cavity due to its slow build-up time, one can nevertheless estimate a coupling efficiency of $\alpha > 0.75$.

By means of the Pound-Drever-Hall method (more details in section 2.5), the linewidth of the red MOT laser can be reduced to $\approx$ 300 Hz. As typical PDH control loops are able to lock within $\sim 10^3$ of the cavity linewidth, there is still room for improvement, what might be especially necessary for the clock laser.

2.5 RAM suppression by 3ω PDH demodulation

For the laser stabilization on a cold atom experiment, the requirement on the frequency stabilization system is to provide the very best long term stability combined with a linewidth reduction of the laser frequency. Recent developments towards ultranarrow-linewidth laser[28] could potentially allow to build more compact and all-fibered narrow-linewidth laser system, enabling even more compact strontium experiments.

Even though the PDH stabilization is widely used in many different technical environments, a more detailed instruction to PDH locking will be given in the following as an extension of this technique by means of 3ω demodulation was tested.

[28] OEwaves; <300 Hz

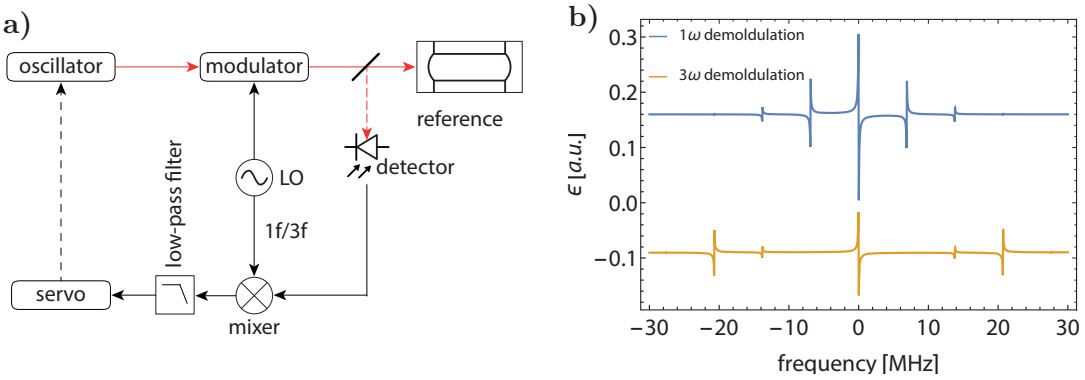

Figure 2.5.1: a) Schematic of the Pound-Drever-Hall system for generating an error signal. b) Calculation of the 1ω and 3ω PDH error signals for the ULE cavity specifications presented in section 2.4.2. The curves are offset for visual clarity.

2.5.1 Pound-Drever-Hall stabilization

For stabilizing a laser of frequency ω_{L} to a resonance of a cavity at ω_{cav} using the PDH method [123] (figure 2.5.1a), the laser beam is first phase-modulated (PM) at an angular frequency Ω with a modulation index β. It is then coupled to the resonator and the reflected signal is detected on a photodiode. Due to the dispersive properties of the cavity near ω_{cav}, the PM is converted into amplitude modulation (AM) components at multiples of Ω. This signal is then multiplied with the local oscillator (LO) Ω having a relative phase ϕ in a double-balanced mixer (DBM), which generates the final demodulated error signal.

The mathematical expression for an electromagnetic field $E_0 e^{i\omega_L t}$ after undergoing a phase modulation at a frequency Ω is given by

$$E = E_0 e^{i(\omega_{\mathrm{L}} t + \beta \cos \Omega t)} = E_0 e^{i\omega_{\mathrm{L}} t} \sum_{m=-\infty}^{\infty} i^m J_m(\beta) e^{im\Omega t}, \tag{2.5.1}$$

where β is the modulation depth and J_m the Bessel function of m^{th} order. This signal is transferred to the resonator and partially reflected. Using the optical transfer function $A(\omega)$ of the resonator [124], the reflected signal is computed yielding

$$E_r = E_0 \sum_{m=-\infty}^{\infty} i^m J_m(\beta) A(\omega_{\mathrm{L}} + m\Omega) e^{i(\omega_{\mathrm{L}} + m\Omega)t}, \tag{2.5.2}$$

where

$$A(\omega) = \sqrt{1-\mathcal{T}_1-\mathcal{L}_1} - \frac{\mathcal{T}_1\sqrt{1-\mathcal{T}_2-\mathcal{L}_2}e^{i2L\omega/c}}{1-\sqrt{1-\mathcal{T}_1-\mathcal{L}_1}\sqrt{1-\mathcal{T}_2-\mathcal{L}_2}e^{i2L\omega/c}}\,. \tag{2.5.3}$$

is the resonator's transfer function. After some algebra, the generalized form of the reflected signal can be deduced to (refer to [125] for more details)

$$\begin{aligned}|E_r(\omega_\mathrm{L})|^2 = |E_0|^2 \Bigg[&\sum_{n=-\infty}^{\infty} J_n^2(\beta)|A(\omega_\mathrm{L}+m\Omega)|^2 \\ &+ \sum_{m=-\infty}^{\infty}\sum_{p=1}^{\infty}(-1)^p[\Re(X^+_{m,2p})\cos(2p\Omega t) - \mathfrak{F}(X^-_{m,2p})\sin(2p\Omega t) \\ &+\Re(X^+_{m,2p-1})\sin((2p-1)\Omega t) + \mathfrak{F}(X^-_{m,2p-1})\cos((2p-1)\Omega t)]\Bigg]\,.\end{aligned} \tag{2.5.4}$$

Here, the following abbreviation has been introduced:

$$\begin{aligned}X^\pm_{m,p} = &J_m(\beta)A(\omega_\mathrm{L}+m\Omega) \\ &\times\left[J^*_{m-p}A^*(\omega_\mathrm{L}+(m-p)\Omega) \pm J^*_{m+p}A^*(\omega_\mathrm{L}+(m+p)\Omega)\right].\end{aligned} \tag{2.5.5}$$

From this, the PHD error signal is generated as the amplitude of the sine and cosine Fourier components at $p\Omega$ of equation 2.5.4) by multiplying with the LO signal $\cos(p\Omega t+\phi)$ with a proper phase-shift ϕ. The PDH error signal is then given by

$$U_\mathrm{err}(\omega_\mathrm{L},\phi) = \frac{1}{T}\int_0^T |E_r|^2\cos(p\Omega t+\phi)\,\mathrm{d}t\,. \tag{2.5.6}$$

For odd p and $\phi = 0$, an error signal as shown in figure 2.5.1b is produced which has has a steep zero-crossing in the resonance case. It has also a linear behavior near the zero-crossing and linear scaling around it, making it ideal for use with standard PID regulators.

Estimation of the in-loop frequency stability

Besides the delayed self-heterodyne interferometry, a common way to estimate the linewidth of a laser locked to a reference cavity is to beat it with another laser of similar frequency and similar or narrower linewidth. As a second laser was not available, the frequency stability was estimated by analyzing the in-loop error signal. As the optical frequency fluctuation is converted to a voltage error signal, knowing the discriminator slope of error signal allows estimate the noise based on the in-loop RMS noise. For a modulation frequency much larger than the cavity

linewidth, the slope at the center of a PDH error signal ϵ is given by

$$\mathcal{D} = \left|\frac{\mathrm{d}\epsilon}{\mathrm{d}\nu}\right| = \frac{V_{\mathrm{pp}}}{\nu_{\mathrm{cav}}} \tag{2.5.7}$$

where V_{pp} is the peak-to-peak amplitude of the dispersive error signal before the servo controller and ν_{cav} is the cavity linewidth (FWHM). However, measuring V_{pp} of a recorded error signal is relatively imprecise in the case of a high-finesse cavity as the linewidth of the probe laser is (usually) much larger. Alternatively, the laser can be locked on maximum transmission and the error signal offset tuned to half of the transmission.

The measurement of the closed loop error signal RMS ϵ_{rms} can be then converted into a RMS frequency fluctuation. Assuming Gaussian (white) noise, the laser frequency noise ν_{rms} can be estimated by using the relation [126]:

$$\nu_{\mathrm{rms}} = 2\sqrt{2\ln 2}\frac{\epsilon_{\mathrm{rms}}}{\mathcal{D}}\,. \tag{2.5.8}$$

Following the paper by Di Domenico *et al.* [127] the laser linewidth can also be approximated by a simple geometrical analysis using the frequency-noise power spectral density (FN-PSD), which is the fundamental parameter in the frequency domain. It is measured in units of $\mathrm{Hz}^2/\mathrm{Hz}$ and, given the knowledge of the conversion of voltage to frequency, can be deduced via

$$S_\nu(f) = \frac{S_{\mathrm{V}}(f)}{\mathcal{D}^2}\,, \tag{2.5.9}$$

where $S_{\mathrm{V}}(f)$ is the measured FFT PSD in V^2/Hz. They showed that the sections of the FN-PSD lying below the so-called β-separation line

$$\beta(f) = \frac{8\ln 2}{\pi^2} f\,, \tag{2.5.10}$$

can be neglected as contribution to the laser linewidth. Then, the β-separation-line estimates for the laser linewidth $\delta\nu_{\mathrm{L}}$ (FWHM) can be calculated as follows::

$$\delta\nu_{\mathrm{L}} = \sqrt{8A\ln 2}\,. \tag{2.5.11}$$

Here, A is the area under the frequency-noise curve, calculated in the intervals where $S_\nu(f) > \beta(f)$ holds.

2.5.2 Residual Amplitude Modulation (RAM)

Besides parasitic etalon effects and temperature dependencies of electronic components in the servo circuit, RAM generated by electro-optic modulators is a predominant issue for high precision cavity locking. It has been extensively characterized [128, 129] and many active suppression methods have been developed ([120] e. g.).

RAM occurs due to imperfections during phase modulation, which manifest themselves in the form of unequal magnitudes of the sidebands and time varying relatives phases between them. The origin of such imperfections lies mainly in the electro-optical crystal. Temperature dependent birefringence, optical scattering and etalon effects in the optical path all reduce the amount of phase modulation and can add parasitic amplitude modulation at the same driving frequency. This amplitude modulation alters the lock point of the PDH system, leading to instabilities of the servo loop or slow frequency drifts of the laser. Following to the derivation in [125, 130], the purely phase modulated PDH signal from equation 2.5.1 can be extended to include RAM as follows:

$$E^{\mathrm{AM}} = E_0 \left(1 + \mu \sin(\Omega t) + \nu \cos(\Omega t)\right) e^{i(\omega_{\mathrm{L}} t + \beta \cos \Omega t)}\,, \tag{2.5.12}$$

where μ and ν are the in-phase and quadrature components of the parasitic AM. Since RAM is usually a small perturbation, i.e. $\mu, \nu \ll 1$, the approximation

$$1 + \mu \sin(\omega_{\mathrm{m}} t) + \nu \cos(\omega_{\mathrm{m}} t) \approx e^{\mu \sin \omega_{\mathrm{m}} t + \mu \cos \omega_{\mathrm{m}} t}$$

holds. Further Fourier expansion of the frequency modulated signal leads to

$$\begin{aligned} E^{\mathrm{AM}} &= E_0 e^{\mu \sin \omega_{\mathrm{m}} t + \mu \cos \omega_{\mathrm{m}} t} e^{i(\omega_{\mathrm{L}} t + \beta \cos \omega_{\mathrm{m}} t)} \\ &= E_0 \sum_{k=-\infty}^{\infty} \sum_{l=-\infty}^{\infty} i^l J_k(\overline{\beta}) J_l(-i\nu) e^{i[\omega_{\mathrm{L}} + (k+l)\omega_{\mathrm{m}}]t} \\ &= E_0 \sum_{m=-\infty}^{\infty} \left\{ \sum_{l=-\infty}^{\infty} i^l J_{m-l}(\overline{\beta}) J_l(-i\nu) \right\} e^{i(\omega_{\mathrm{L}} + m\omega_{\mathrm{m}})t}. \end{aligned} \tag{2.5.13}$$

with $\overline{\beta} = \beta - i\mu$. As $\nu \ll 1$, the Bessel functions simplified to $J_0(-i\nu) = 1$ and $J_{\pm 1}(-i\nu) = \mp i\nu/2$ and $J_n(-i\nu) = 0$ for $|n| > 1$. equation 2.5.13 reads now as

$$E^{\mathrm{AM}} = E_0 \sum_{m=-\infty}^{\infty} \left\{ -i J_{m+1}(\overline{\beta}) \frac{i\nu}{2} + J_m(\overline{\beta}) + i J_{m-1}(\overline{\beta}) \frac{-i\nu}{2} \right\} e^{i(\omega_{\mathrm{L}} + m\omega_{\mathrm{m}})t}\,, \tag{2.5.14}$$

Because $2J'_m(z) = J_{m-1}(z) - J_{m+1}(z)$[29],

$$J_m(\overline{\beta}) \approx J_m(\beta) - \frac{i\mu}{2}[J_{m-1}(\beta) - J_{m+1}(\beta)]\,, \tag{2.5.15}$$

and therefore

$$E^{\mathrm{AM}} = E_0 \sum_{m=-\infty}^{\infty} J_m^a e^{i(\omega_\mathrm{L}+m\omega_\mathrm{m})t}\,, \tag{2.5.16}$$

with

$$J_m^a := J_m(\beta) + a^* J_{m-1}(\beta) + a J_{m+1}(\beta)\,, \tag{2.5.17}$$

and $a = (\nu + i\mu)/2$. The equation 2.5.17 replaces $J_m(\beta)$ in equation 2.5.1 and the error signal in presence of residual AM can be calculated by inserting $J_m^a(\beta)$ into equation 2.5.4.

Following [120, 131], the in-phase RAM originates from polarization alignments and from phase shifts due to the temperature- and stress-dependent birefringence of the elctro-optical crystal. The quadrature component is potentially created by several source: first, the piezo-electric response of the crystal, leading to a spatial position dither. Second, from the spatial inhomogeneity of crystal's modulation field in crystal and third, from the temperature dependence of the beam optical path.

2.5.3 Third-harmonic demodulation technique

To the knowledge of the author, this technique had been first evaluated by Koji Arai in 2001 [132] in the context of gravitational wave detectors and further investigated by Holger Müller for linear cavities [125]. Also, a first commercial EOM driver by QUBIG supports natively $3f$ demodulation.

A more extensive discussion of this kind of error-signal extraction is given in [132]. As previously described, a typical PDH error signal is generated by using $1\omega_\mathrm{m}$ as the local oscillator frequency. By using the third harmonic of the LO frequency ($3\omega_\mathrm{m}$), however, the effect of RAM on the error signal can be reduced. The generated signal, as computed from equation 2.5.6 with $p = 3$ with the cavity specifications as presented in section 2.4.2 and a modulation index of $\beta_\mathrm{m} \simeq 3.83$ is shown in figure 2.5.1b. This specific choice of $\beta_\mathrm{m} \simeq 3.83$ is motivated by the fact that the first order sidebands vanish exactly at this value. The peak-to-peak amplitude of the error signal discriminator is only half as high as for the $1\omega_\mathrm{m}$ technique, which could be confirmed experimentally.

In figure 2.5.2a the theoretical impact of both techniques on the RAM suppression is shown for cavity specifications that are close to the ULE cavity presented

[29] the prime denotes the derivative of the argument

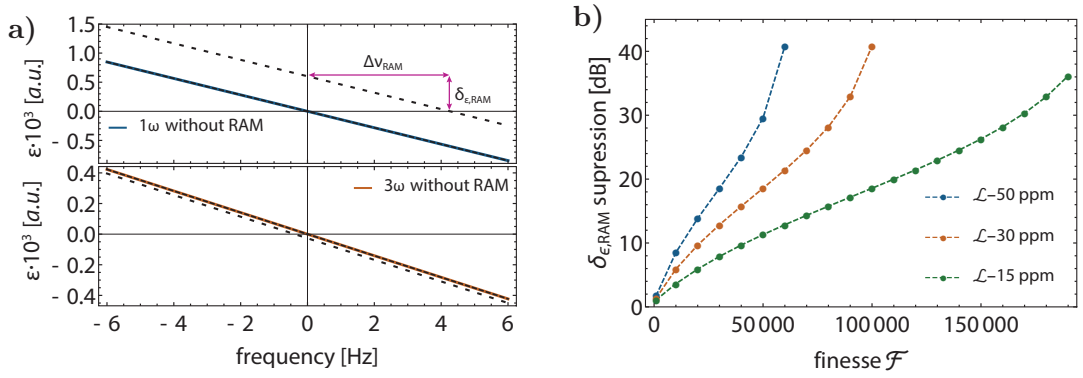

Figure 2.5.2: a) shows the offset-effect of the RAM on the error signal for 1ω (top) and 3ω (bottom) demodulation for a cavity with $\mathcal{T} = 50\,\text{ppm}$ and $\mathcal{L} = 50\,\text{ppm}$. The dashed lines indicate the in-phase (μ) contribution and the dotted lines the out-of-phase (ν) contribution. b) Suppression of the RAM-induced error signal offset for different mirror losses.

in section 2.4.2. A RAM of 100 ppm was assumed. It can be seen from $\Delta\nu_{\text{RAM}}$ of the plotted signals that the 3ω technique suppresses the impact of out-of-phase RAM (the quadrature component) by a factor of ~ 10 while leaving the in-phase RAM nearly unaffected. Furthermore, the effect of this technique for different cavity finesse was evaluated. Three scenarios with $\mathcal{L} = 50\,\text{ppm}$, $\mathcal{L} = 30\,\text{ppm}$ and $\mathcal{L} = 15\,\text{ppm}$ are depicted in figure 2.5.2b, where $\mathcal{L}$ can also compromise losses due to improper spatial mode matching. It can be seen that the 3ω technique can suppress RAM more effectively for values of the cavity finesse as cavity losses increase.

An advantageous side-effect is that most of the carrier laser power is contained in the sidebands that do not enter the cavity, which reduces resonance frequency shifts due to heating caused by photon absorption.

Experimental setup

Both locking schemes were tested under the same conditions. The incident power on the cavity was set to 20 µW and the fiber-based EOM was modulated at $\omega_{\text{m}} = 2\pi \times 6.9\,\text{MHz}$. In order to extract the proper signal at 3ω, the photo diode signal is passed through by a combination of a low- and high-pass filters. The sharp filtering of a band-pass would be inappropriate as it causes frequency dependent phase shifts which can then cause frequency shifts of the locked laser. Afterwards, the signal is amplified and demodulated with the triple modulation frequency of the LO.

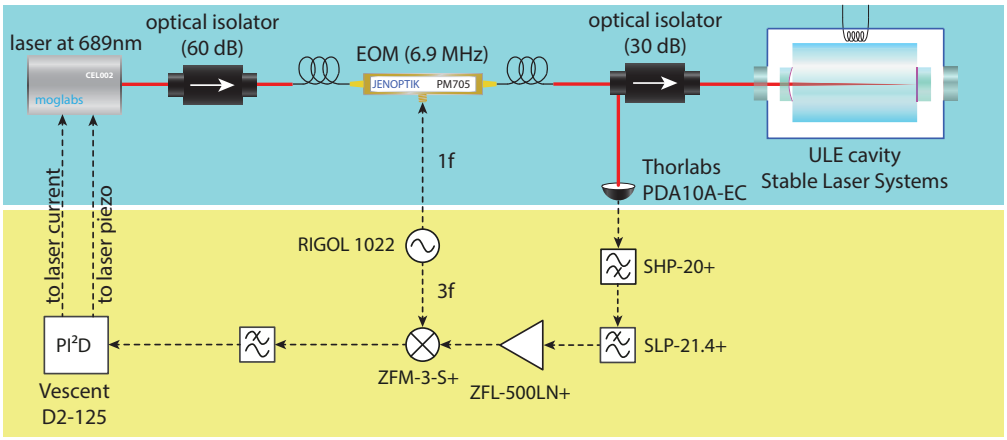

Figure 2.5.3: The 3ω locking scheme.

Unfortunately, the $3f$ demodulation technique could not be tested with the bulk EOM that generates the PDH sidebands on the actual experiment. Not only was the bandwidth of the dual-channel frequency generator too small to reach the triple resonance frequency, the maximum incident RF on this specific EOM is too small to reach a high modulation index. The risk of damaging the EOM by pushing it to its maximum ratings was too high. It could be however still worth to try at lower modulation depth.

Experimental results

In order to determine whether the 3ω demodulation technique could serve as an alternative to the classical PDH scheme, it is of importance that the linewidth values of the locked laser are comparable in both cases. Therefore, the linewidths were measured using the β-separation line method as described in section 2.5.1. The PSD was recorded with a spectrum analyzer[30] and the results are plotted in figure 2.5.4b. The laser linewidths (FWHM) are 260 Hz for the $1\omega_m$ method and 270 Hz for the $3\omega_m$ PDH method.

The figure 2.5.4a shows two time-traces from error signals for the $1\omega_m$ PDH and the $3\omega_m$ PDH. The error signal offsets were translated into frequencies by using the error signal discriminator. For $1\omega_m$ locking, the offset drift is on the order of 7 Hz peak-peak whereas the drift is reduced to 0.8 Hz peak-peak for $3\omega_m$. The resulting RAM suppression factor of ~ 9 is in a good agreement with the prediction in subsection 2.5.3. In order to gain further insights, it would be necessary to compare the error signal dc-drifts to those of the room or the EOM temperature.

However, another comparison of both techniques could be achieved by tracing

[30] SRS, SR760 FFT

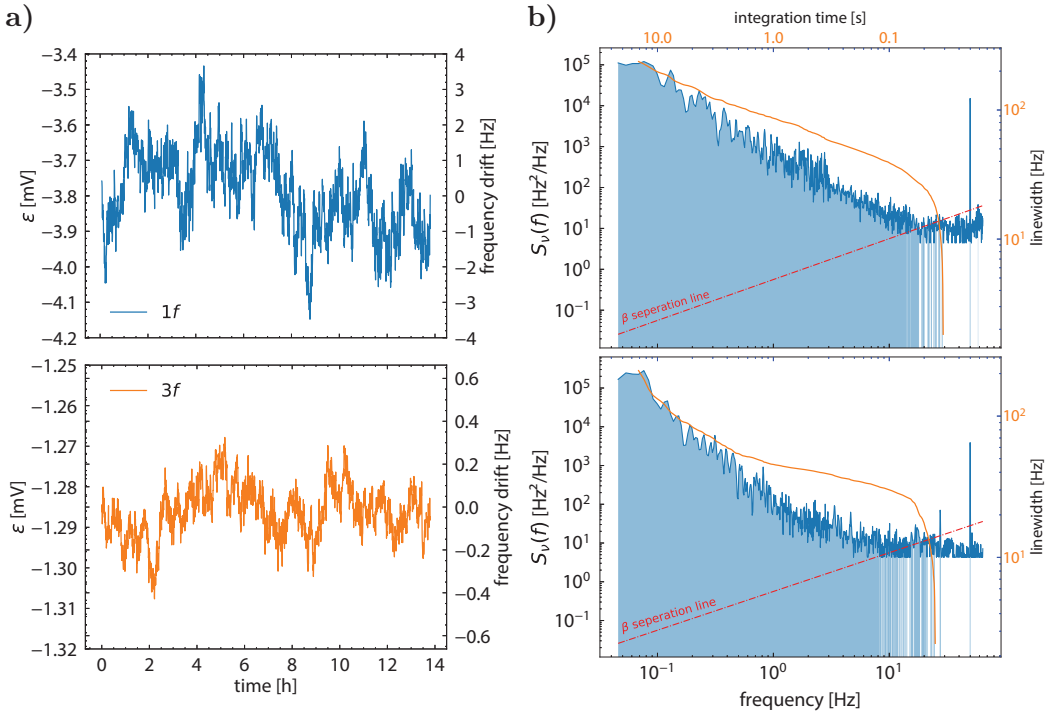

Figure 2.5.4: a) shows the recorded error signal of the $1f$ PDH (*top*) and the $3f$ PDH method (*bottom*) over 14 h, where each data point is an average over 30 s and b) shows the corresponding FN-PSD used for the linewidth measurement of both techniques.

the beat-signal of two identical locked lasers. Moreover, [133] suggests that "there still exists a potential for $3f$ RAM (generated by the initial modulation signal) to alter the lock point of the system". Therefore, the results of the measurement presented here can been only seen as a proof-of-principle and more tests need to be done to conclude on the net benefit of this technique.

2.6 Conclusion

In this chapter, the realization of a low footprint vacuum system with pressures around 10^{-10} mbar was presented. Besides, a robust and reliable strontium oven has been developed, which allows to produce a collimated strontium beam. Its operational temperature of 450° can be reached with only 13 W of electrical power consumption, being therefore almost three times more efficient than comparable

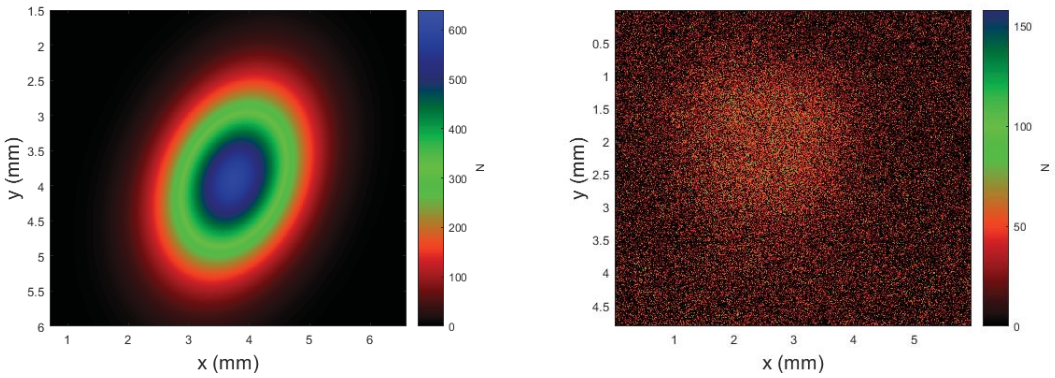

Figure 2.6.1: Shown are absorption imaging pictures of strontium atoms in a) the blue MOT and b) a early-stage red MOT.

designs [112]. The magnetic quadrupole coils have been installed and provide also the ability the slow down the hot atomic beam by means of Zeeman slowing.

Furthermore, data has been taken from the Zeeman slower and MOT assembly showing MOT atom numbers as a function of various Zeeman slowing parameters. This allowed to find the optimum parameters for MOT loading and to work out the MOT capture velocity. This work is not presented here as the author was not directly involved in these measurements. However, all design principles have been experimentally confirmed, allowing to cool and trap strontium in the blue and also red MOT (see figure 2.6.1[31]).

The construction and optimization of the apparatus is still an ongoing process. Decision need to be taken on the optical transport from the position of the MOT to the ring cavity and how to to tackle the problem of the insufficient MOT laser power. The power issue will become even worse with the ongoing natural degradation of laser diodes over their lifetime. An established approach is be to replace the untreated vacuum glass cell by an anti-reflection coated cell[32]. Eventually, a reliable technique needs to found for refilling the oven. As this design lacks of a valve in between the oven and the main chamber, air will get into the main cell an oxidize all of the strontium deposits, when the oven gets refilled. This could also strike the ring cavity, which will be glued into the glass cell, and may lead to its potential loss.

[31] Data were taken by Mathieu Bertrand. More details will be presented in his upcoming thesis.
[32] Modern liquid anti-reflection coatings can be a versatile and less expensive alternative to sputtering techniques. Their vacuum compatibility, however, needs to be confirmed.

Chapter

Fabrication of CO_2 machined cavities for cold atom experiments

3

Due to the ongoing research in the field of laser material processing, this field constantly exploits new scopes of application, beginning from the micro-optics industry to the preparation of metallic injection molds for applications in medical engineering (protection against bacterial contamination). The laser beam as a tool has some significant advantages: it is a massless and contactless tool which reduces significantly the mechanical stress or damage on the workpiece. Furthermore, it is a wear-free as well as easily and quickly controllable tool.

Especially the far-infrared CO_2 laser has become one of the most popular lasers since its development in 1964 by Patel [134]. It is a highly reliable, high power beam source that meets many industrial and scientific needs. Owing its emission wavelengths, the CO_2 laser is prevalent in the (micro-)optics industry as it coincides with a maximum in the absorption spectrum of fused silica. This leads to a large scope of applications, ranging from polishing of macroscopic optics to micromachining of optical waveguides. In the cold atoms community, the CO_2 laser is mainly used for producing *quasi-electrostatic traps* (QUEST) for neutral atoms [135] and for the fabrication of micro structures on fiber tips, as most recently published in [136]. These fiber structures opened a new scope of applications where the integration of Fabry-Perot resonators in optical fibers is advantageous, as it leads to a reduction of the apparatus size, an increased stability and the advantage of being directly fiber coupled.

In the present work, the fabrication of a mirror structure on a fiber tip is required to realize the high-finesse ring cavity as motivated and presented in the subsequent chapter. This cavity requires an elliptical mirror of 90 µm diameter and two laser-polished plane fused silica substrates – both viable on an existing CO_2 dot milling setup.

This chapter summarizes the basic knowledge about the CO_2 laser used in our experiment, the interaction of the laser radiation with quartz glass, the discussion of laser machining large structures on optical fibers and of the laser polishing process.

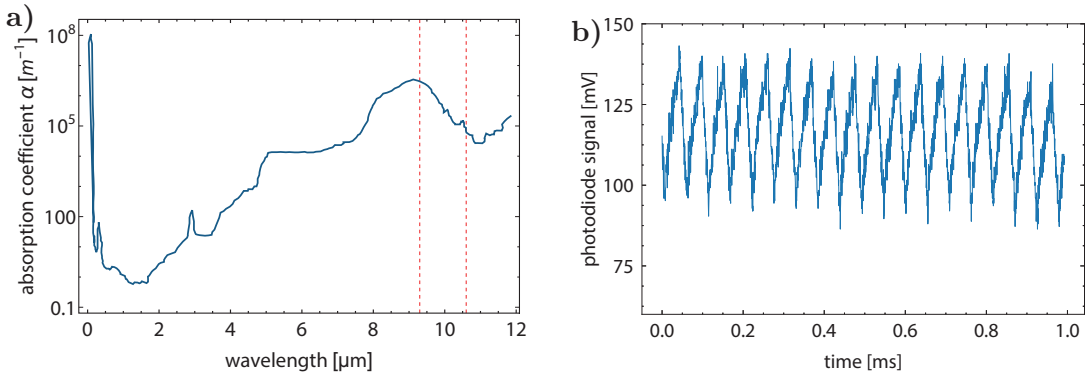

Figure 3.1.1: a) Absorption coefficient of fused silica (reproduced from [137]). The red dashed lines indicate the common CO_2 laser wavelength at 9.3 µm and 10.6 µm. b) Photodiode signal of the SYNRAD *firestar v20* output power at 70 % duty cycle. The observed power modulation has a frequency of 20 kHz.

3.1 Interaction principles of CO_2 lasers with fused silica

The CO_2 laser is a molecular gas laser based on a gas mixture as gain medium. It emits light at numerous infrared wavelengths between 9 µm and 11 µm with most common wavelengths are at 9.3 µm and 10.6 µm. This is realized by a transition between two vibrational states of the linear CO_2 molecule. The excitation of the molecule into the upper laser level occurs by electron impact or, more often, by collisions with vibrationally excited N_2 molecules added to increase pumping efficiency. Helium is also added for cooling and efficient drainage of the lower pumping level. This gaseous gain medium is enclosed in a tube that is usually at pressures below the normal pressure and placed between resonator mirrors.

These lasers combine high efficiency and versatility as they allow to obtain high peak powers in the pulsed mode or large laser energies in continuous or almost continuous operation. The large scope of industrial and scientific applications can be explained by the fact that there are several distinct types of CO_2 lasers that share the same active medium but differ in their internal structure.

For the CO_2 laser[1] used in the setup presented in the following, the population inversion required for lasing is achieved by electrically exciting the first vibrational level of the nitrogen via a radio frequency source (RF) at 81.36 MHz, which is close to the target CO_2 level. To adjust the laser power, the pumping is modulated with

[1] SYNRAD *firestar v20*

a frequency of 20 kHz by the laser controller (*duty cycle*). Even though the manufacturer claims that the output power remains unaffected by the modulation at 20 kHz, a clear modulation can been seen on a fast photodiode[2] (see figure 3.1.1b). A new laser[3] at 9.3 µm with duty cycles up to 100 kHz has been purchased, which should reduce any possible impact of the modulation on a single pulse.

When a sample of fused silica sample is exposed to a CO_2 laser beam, it can undergo phase transitions between solid, liquid and gaseous depending on the temperature and pressure generated by the incident beam. This transformation of the glass state can lead to changes in its structure and physical properties. According to Lambert-Beer's law, the attenuation of the light intensity $I(z)$ in a medium along the propagation axis z is given by

$$\frac{I(z)}{I_0} = e^{-\alpha z}, \tag{3.1.1}$$

where I_0 is the incident intensity and α is the absorption coefficient, which can be expressed in terms of the imaginary part of refractive index, n_i, as

$$\alpha = \frac{4\pi}{\lambda} n_i(\lambda, T)\,. \tag{3.1.2}$$

The absorption coefficient is often related to the so-called '*penetration depth*', which is the inverse of α. Not only depends the absorption coefficient strongly on the wavelength, but also on the temperature of the medium via $n_i(T)$.

Given the absorption coefficient for fused silica at room temperature (see figure 3.1.1a), the penetration depth of a wavelength of 10.6 µm is equal to 20 µm and decreases to 4 µm close the evaporation temperature. As the medium heats up, the absorption of power from the irradiating laser shifts towards the entry surface, leading to a increasingly localized transfer of energy into the medium.

The fused silica surface is affected by this process in several ways, leading to a modification of the physical and chemical properties of the material. More precisely, an increase in density [138], refractive index [139] and Young's modulus [140] is observed with increasing substrate temperature. Furthermore, the absorbed energy is locally transferred into heat in the surface layer and results in a decrease of the viscosity.

If the laser irradiation is sufficiently intense, the material will reach its evaporation temperature and pass directly from the solid state to the gaseous state. This effect is called laser ablation, leading to permanent deformations of the surface in the form of approximately Gaußian-shaped craters. For temperatures below the evaporation temperature however, the combined effect of surface melting and

[2] VIGO PVM-10.6
[3] SYNRAD *firestar v30*

tension of the glass results in an outflow of any surface roughness and thus smoothing. After cooling, the fictive glass temperature[4] changes and densities as well as thermo-mechanical stresses are alsopresent in the material.

For the sake of brevity, a detailed discussion of the corresponding thermo-mechanical model is not given here. The interested reader is referred to [141] and references therein for additional information.

3.2 Experimental setup for laser beam machining

3.2.1 Single-shot dot milling on fused silica

Many techniques have been developed to fabricate precise spherical mirror structures on glass substrates. For example, superpolishing of fused-silica is a powerful techniques which allows to produce spherical mirrors with sub-Ångström surface roughness. The trade-offs, however, are that it can be only applied to macroscopic substrates and that achievable radii of curvatures (ROC) are constrained by $R > 20\,\mathrm{mm}$. Another example for precise mirror fabrication is focused ion beam milling [142, 143]. Even though this method allows to produce structures as small as 10 µm in diameter, its achievable surface roughness of $\approx 3\,\text{Å}$ is still worse than a CO_2 machined structure [144]. Furthermore does this method only work under vacuum, what reduces its versatility.

CO_2 machining represents an excellent alternative as it overcomes the limitations mentioned so far. Single or multiple CO_2 pulses are applied to the center of a fiber tip, which are then coated with a precision dieletric coating. The resulting spherical micro-structures feature a low surface roughness of $\approx 2\,\text{Å}$, enabling the fabrication of fiber-based optical cavities with finesse of up to 190 000 [145].

Limitations of the single pulse fabrication: The profile of a depression generated by a single CO_2 laser pulse has a Gaußian rather than a spherical shape [146]. The effective mirror diameter is therefore only a fraction of the actual structure diameter on the substrate. It is therefore nearly impossible to fabricate mirror structures that extent over an entire fiber tip, even with large laser CO_2 beam diameters [145]. As a consequence, the length of fiber-based cavities is limited to a few hundreds of micrometers as the transverse beam diameter reaches the effective beam diameters and clipping losses lead to a drastic decrease of the cavity finesse.

Furthermore, a CO_2 laser beam does not allow to tailor the aspect ratio of the structure. A astigmatic CO_2 laser beam might lead to a structure with two

[4] The fictive temperature describes at which temperature the structure of (super)cooled liquid glass is 'frozen in'. Depending on the cooling rate, glass can have different fictive temperature values: a fast-cooled glass has a fictive temperature greater than the same glass cooled slowly.

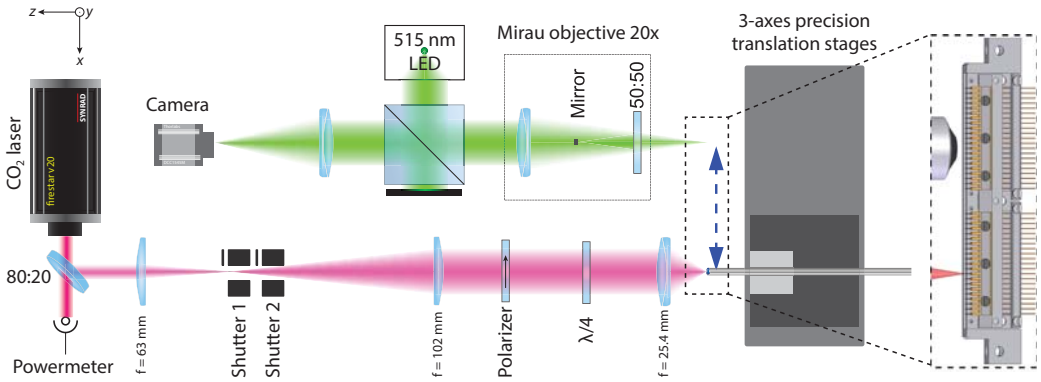

Figure 3.2.1: The CO_2-laser machining setup as described in section 3.2.

different radius of curvature along its principle axes, which then results in an undesired cavity birefringence. However, in certain situations it may be of interest to engineer structure for even larger birefringece [147].

In order to overcome these problems, multi-shot schemes can be employed whereby a larger number of weak CO_2 laser pulses is applied on a single fiber tip. By optimizing the pattern of target points on the substrate surface, a wide range of shapes can be created with this technique while maintaining the good surface quality characteristic of CO_2 machining.

3.2.2 Multi-shot fabrication

The multi-shot setup and the corresponding control software have been developed by Sébastien Garcia, Konstantin Ott and Klemens Schüppert (see [148, 149] for more details) and is depicted in figure 3.2.1. It is comprised of a CO_2 laser with external pulsing, focusing optics, high-precision translation stages and an optical profilometer. Several changes of the software and optical setup have been implemented over the course of this thesis to improve overall performance. For sake of completeness, the main components and their current state will be explained in the following.

Mechanical and beam shaping hardware: As described in section 3.1, the temperature of the surface depends strongly on both the power and the size of the incident CO_2 beam. It is therefore essential to have a precise control over the laser parameters in order to obtain consistent results.

The laser is water-cooled and placed under a temperature-stabilized flow-box to ensure stable operation. The output power fluctuates under optimal conditions by is less than 0.5 % over approximately an hour, which is crucial in order to obtain reproducible structures during mass-production of micro-structures.

Pulses are generated by a combination of pulse-width modulation (PWM) of the laser's duty cycle and by two mechanical shutters. This arrangement allows to keep the switch-off time of the laser below 200 µs in order to maintain stable operation.

The beam spot size at the target position is controlled by the combination of three lenses on the target position. The beam is then going through a polarizer and a $\lambda/4$ waveplate to get a circular polarization for avoiding elliptical structures[5]. The last lens is a $f = 25.4$ mm asphere which focuses the optical power on the fiber.

Besides controlling the laser, a precise positioning of the fiber with respect to the optical beam is required. The setup therefore features three high-precision translation stages along the x[6]-, y[7]- and z[8]-axis. The latter stage has a specified resolution of 1 nm and a repeatibility of 50 nm and allow to adjust the spot size of the laser beam on the fiber tip but also to perform a high-resolution profilometry. In addition, a goniometer stage is about to be implemented soon, allowing to compensate for any angle-misalignment of substrates.

***In-situ* profilometry with a Mirau objective:** The optical profilometer is a non-intrusive (non-contact) characterization instrument that measures the roughness of a surface. It is an interferometric technique that is based on the reflection of light on the Mirau-mirror as the reference plane in order to establish the topography of the structure of interest. The general idea of the optical profilometry is to take several images with different phase shifts by moving the substrate along the optical axis. Combining six (or eight) interferograms separated by $\lambda_P/6$ (or $\lambda_P/8$,) where $\lambda_P = 512 \pm 15$ nm is the wavelength of the profilometer's LED light, the phase information of the surface of interest can be unwrapped and transformed into a path difference. This method allows to extract the profile height z at each point.

The optical microscope of the setup is composed of a Mirau-type[9] objective with a numerical aperture of 0.4 and a lens doublet which focuses the images on a monochrome CMOS camera[10]. The nominal transverse resolution is 0.8 µm and the published noise for a plane reference mirror is $\sigma_{\text{mean}} = 1.4$ nm in the case of a single profilometry [148].

[5] A linear polarization leads to an asymmetric absorption of the laser power in the material. which increases the eccentricity of the resulting structure.
[6] Newport GTS150
[7] Newport GTS30V
[8] Attocube ECS5050/NUM
[9] Nikon CF IC Epi Plan DI 20X
[10] Thorlabs DCU223M

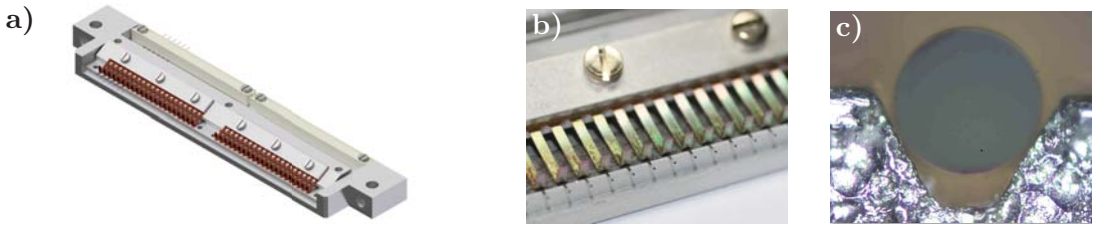

Figure 3.2.2: a) shows a CAD drawing of the fiber holder assembly. b) Photo of the fiber clambs pushing a fiber array into the grooves (after coating) and c) a close-up view of a single v-groove supporting an optical fiber substrate (taken from [149]).

3.2.3 The substrate holders

The handling of high-precision micro optics is a very critical task due to their fragility, small size and the need to maintain surfaces free from dust. Therefore, the development of a proper mechanical mount is an important task considering these crucial requirements and in order to ensure compatibility with the CO_2 setup and the commercial coating machine. Furthermore, a proper substrate holder enables mass fabrication of micro-structures on fibers or other glass materials, which allows to exploit the full performance capability of the CO_2 fabrication station.

Fiber duraluminum v-grooves with spring fixation

The fiber holder has been developed by Konstantin Ott during his Ph.D. [149] and his design has been reused for this project. The design is sketched in figure 3.2.2a. Its main feature are metal strips that act as springs and press the fibers into V-grooves. The grooves are machined with a CNC milling machine that provides the required precision to meet the narrow tolerances required for precise alignment of the fiber substrate. The springs are milled as a comb made of 0.13 mm thick sheets of *Chrysocale*[11].

This support can hold up to 42 fibers allows for mass production while not interfering with the stabilized environment of the CO_2 fabrication setup.

The plane substrate holder

The principal function of the substrate holder is to maintain fused silica substrates of $2.5 \times 2 \times 1$ mm (H × W × D) in a safe position during handling and shipping. Furthermore, the wedge which holds the substrates need to be turned after the

[11] CuSn3Zn9

high-reflective (HR) coating run in order to add an anti-reflective (AR) coating to the backside of the substrates. Therefore, the design shown in figure 3.2.3b has been developed over the course of this thesis.

The design of the front wedge[12] consists of a duraluminum stripe of 1.2 mm thickness. On the front side, 18 squares of 2.1 × 2.6 × 0.9 mm (H × W × D) are milled into the wedge and are thus tight enough to avoid any contamination of the back(front) side of the substrates with high-(anti-)reflective coating due to migration of sputtered material during the coating process. The back side of the wedge is covered with holes that have slightly smaller diameters (2.7 mm) than the diagonals of the front-squares. The remaining material on the edges of the squares serves as support for the glass substrates.

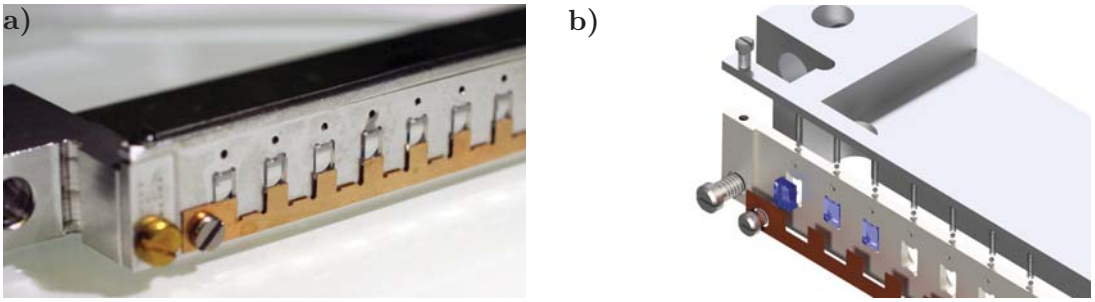

Figure 3.2.3: The substrate holder. a) shows a photo of the assembled mirror holder with the substrates before sending it for coating. b) is a CAD illustration of the holder assembly.

For the sake of safety and convenience, two redundant fixation methods have been integrated. Small holes are drilled into the top of the wedge, which contain compression springs (0.6 mm in diameter) and steel balls (0.5 mm in diameter) for a single contact point. A front spring made of Chrysocale further avoids any sliding of the substrates inside the notches by pushing on their lower ends.

The entire design of the wedge is compatible with the CO_2 machining setup and thus was used for the polishing procedure described in section 3.3. The fibers and substrates to be coated are all aligned to same height of the support disc for the coating process. In order to reduce the creation of dust during handling after the coating process, all mechanical parts have been either sandblasted or roughened in a stirring oil bath filled with an iron splinters.

[12]Manufactured by the mechanical workshop of Ulm University (Germany)

3.3 Laser polishing of fused silica surfaces

To realize the ring cavity as described in section 4.4, two plane substrates of dimension $2.5 \times 2 \times 1\,\text{mm}$ (H × W × D) are needed as plane mirrors. Due to the limited availability of super-polished ($\text{Rq} \leq 0.2\,\text{nm}$) substrates of 1 mm thickness, a highly-polished fused silica wafer[13] has been selected as starting material for the plane mirrors. As its is surface $\text{Rq} < 0.5\,\text{nm}$ does not meet requirements for the ring-cavity, a laser polishing technique has been implemented, which is fully compatible with the CO_2 multi-shoot setup.

Laser polishing is in principle a relatively simple technique and therefore a well studied and established fabrication method in the micro-optics industry. Already in 1982 it had been shown that CO_2 laser radiation can be used to reduce the surface roughness of mechanically polished fused silica [150]. Recent studies investigated the optical properties of different laser polished glass types and combined it with further laser-based processing steps to allow for additional shape corrections (*Laser Beam Figuring*) [151]. Typical industrial applications are lens polishing [152] and scratch removal on fused silica optics [153].

The difference of laser polishing compared to classical mechanical polishing lies in its fundamentally different way of interacting with the material: It smooths by remelting and relocating instead of removing surface material. In particular, in a meandering scanning strategy, the substrate to be polished is exposed to defocused *cw* CO_2 laser radiation which heats up a thin surface layer of the glass just below the evaporation temperature. With increasing temperature, the viscosity in the surface layer is sufficiently reduced to allow for a lateral flow by surface tension of the molten material which leads to the reduction of the surface roughness. Therefore, contactless polishing can be performed while almost no material is lost in the process.

However, one of the inherent difficulties created by this technique is the presence of thermal gradients and thus the induced thermal stresses in the glass substrate, which might lead to birefringence or the creation of cracks particularly in the case of glasses with high thermal expansion coefficient.

3.3.1 Substrate preparation

The wafer was cut with an automatic diamond saw[14] to get substrates of correct dimensions. To protect the surface from any damage during the cutting procedure, the wafer was covered with a thin layer of PMMA[15]. From figure 3.3.1a it can be

[13] Edmund Optics: Fused Silica Wafer 88545; 100 mm in diameter.
[14] Disco DAD-321
[15] Polymethyl methacrylate resist

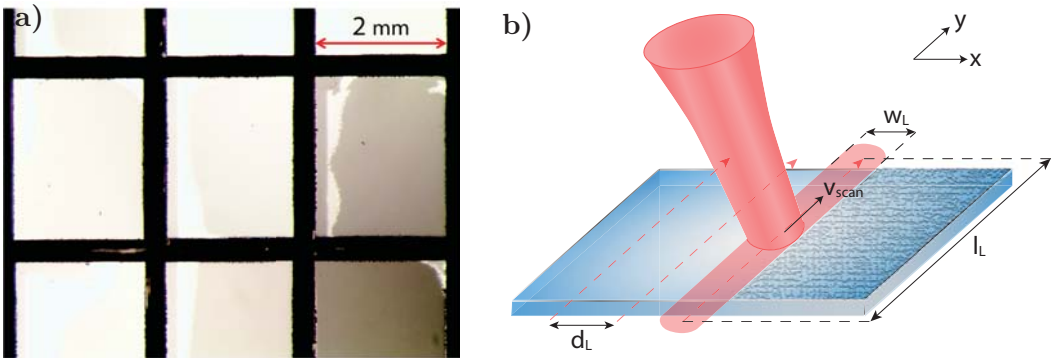

Figure 3.3.1: a) Photo of the cut wafer covered with PMMA, taken under an optical microscope. b) Illustration of the basic operational principle of laser polishing. w_L is the beam spot diameter, v_{scan} the scan speed, l_{L} the length and d_{L} the line separation.

seen that the edges of the substrates look relatively smooth and that no major defects are visible that might interfere with the cavity mode.

The substrates were then cleaned in warm acetone (75 °C) before being placed in a UV-Ozone chamber.The latter cleaning method relies on illuminating the samples from a very short distance ($\approx 5\,\text{mm}$) with UV light of about 250 nm wavelength, which removes any organic residue via photochemical reactions. From the AFM[16] analysis, however, it could been seen that there were still some PMMA residue left on the surface with a thickness on the order of 5 nm. Therefore, the samples were immersed in a Piranha solution which removed the remaining PMMA.

3.3.2 Polishing procedure

To achieve low levels of surface roughness, a processing temperature just below the evaporation point at 2220 °C is required. This temperature must be homogeneous over the whole surface and therefore, a meandering polishing strategy was chosen here, whereby a defocused *cw* CO_2 laser beam scans over the sample surface. As the setup presented in section 3.2 does not feature a galvanometric beam scanner, the samples were moved instead, with a scan speed v_{scan} vertically along the surface plane. When reaching the end of a given line, the substrate was moved sideways by a distance d_{L}. This procedure is shown in figure 3.3.1b.

For the following results, the substrates were illuminated with a CO_2 laser beam of power 2100 mW and a spot $1/e^2$ radius of $w_L/2 \approx 600\,\mu\text{m}$. The line separation was set to $d_{\text{L}} = 250\,\mu\text{m}$ and the scan length was $l_{\text{L}} = 2000\,\mu\text{m}$.

[16] Atomic Force Microscope

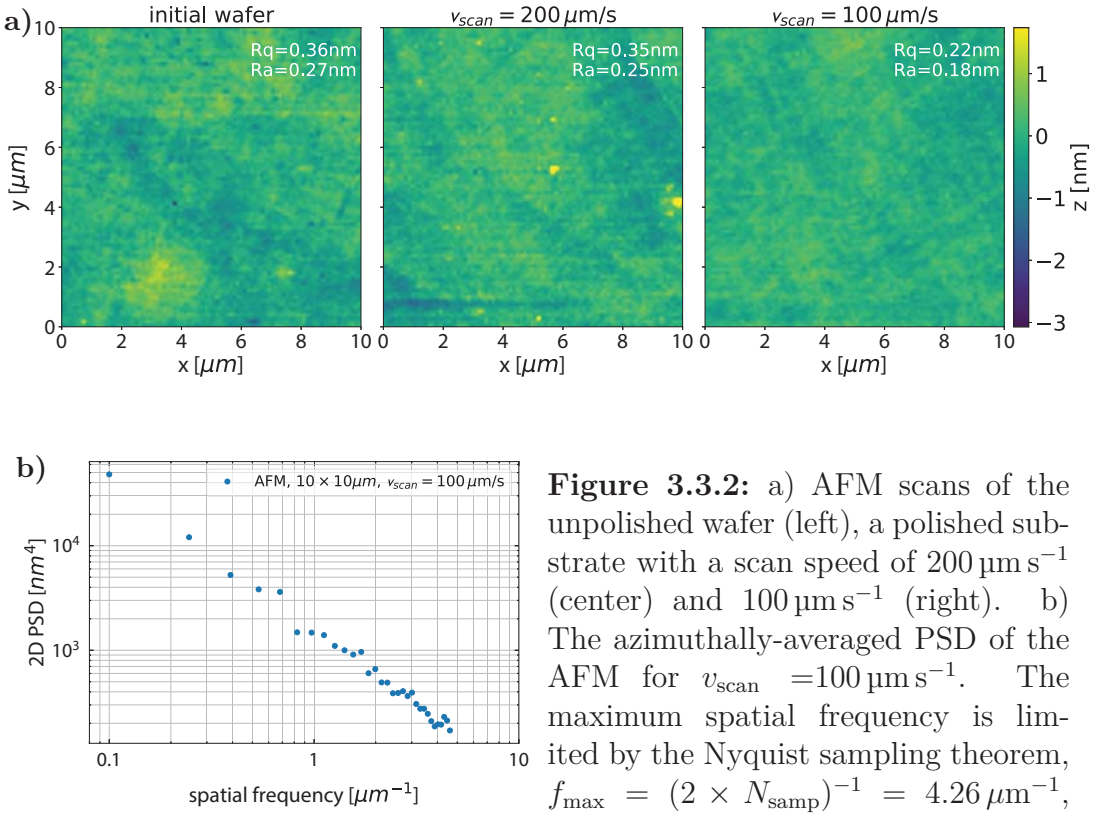

Figure 3.3.2: a) AFM scans of the unpolished wafer (left), a polished substrate with a scan speed of 200 µm s^{-1} (center) and 100 µm s^{-1} (right). b) The azimuthally-averaged PSD of the AFM for v_{scan} =100 µm s^{-1}. The maximum spatial frequency is limited by the Nyquist sampling theorem, $f_{\mathrm{max}} = (2 \times N_{\mathrm{samp}})^{-1} = 4.26\,\mu\mathrm{m}^{-1}$, where $N_{\mathrm{samp}} = 30\,\mu\mathrm{m}/256$ is the spatial resolution of the AFM.

Surface quality diagnostics: To study the polished surfaces, an atomic force microscope (AFM)[17] was used. The surfaces were scanned over a window of 30×30 µm at the approximate position of the cavity mode on the plane mirror (2 mm height, 100 µm from the side). However, due to some faulty measurement fragments in each scan, only areas of 10 × 10 µm could be analyzed, which is smaller than the $1/e^2$ cavity mode diameter on the plane mirrors (≈14 µm).

The raw data were fitted to a 2D-plane and the fit residuals $z(x)$ are used. The surface roughness is expressed through Ra and Rq, corresponding to Ra to the arithmetic average of the absolute values of the fit residuals $z(x)$ over the sampling length l and Rq to the root mean square average of the profile heights

[17] Bruker Dimension Edge Atomic Force Microscope

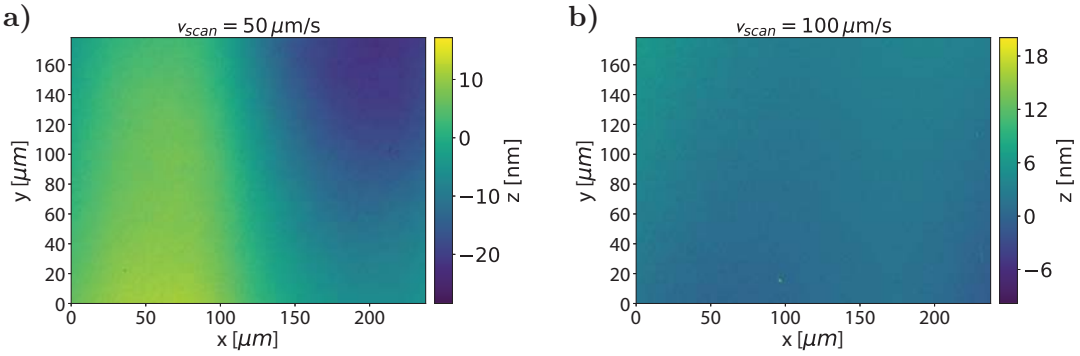

Figure 3.3.3: Shown are the subtracted profiles of the substrates before and after polishing, a) at too low speed and b) at the optimum speed. The global waviness does not occur anymore.

respectively. They are calculated as follows:

$$\mathrm{Ra} = \frac{1}{l}\int_0^l |z(x)|\,\mathrm{d}x\,, \tag{3.3.1}$$

$$\mathrm{Rq} = \sqrt{\frac{1}{l}\int_0^l z^2(x)\,\mathrm{d}x}\,. \tag{3.3.2}$$

In order to properly analyze the measured data, a calibration of the AFM with a scotch-cleaved mica sheet of grade V-1 was done, revealing a height resolution of $\Delta\mathrm{Rq} = 0.09\,\mathrm{nm}$ and $\Delta\mathrm{Ra} = 0.07\,\mathrm{nm}$. The results of the AFM of the CO_2 polished subtrates are shown in figure 3.3.2a. The measured surface roughness of the initial, unpolished fused silica wafer is $\mathrm{Rq} = 0.37\,\mathrm{nm}$ and $\mathrm{Ra} = 0.28\,\mathrm{nm}$. Comparing different scan speeds showed that the best surface quality could be reached for $v_{\mathrm{scan}} = 100\,\mu\mathrm{m/s}$. The measurement shows that the corresponding surface roughness decreased to $\mathrm{Rq} = 0.24\,\mathrm{nm}$ and $\mathrm{Ra} = 0.19\,\mathrm{nm}$, implying the calibration-corrected values $\mathrm{Rq} = 0.22\,\mathrm{nm}$ and $\mathrm{Ra} = 0.18\,\mathrm{nm}$. These results are still higher than the published surface roughness of $\mathrm{Ra} = 0.1\,\mathrm{nm}$ in [151], showing that there is room for improvement. A smaller scan rate lead to a wavy surface, as can be seen from figure 3.3.3a which shows the subtracted profilometer profiles before and after polishing. Naturally, when scanning the beam at a comparatively slow speed, the irradiated section of the material receives much more heat per unit time. As a result, surface tensions lead to a slight drop formation in the process, which ultimately gives rise to the waviness of the surface.

Due to insufficient time, the polishing procedure has not been studied in greater detail over the course of this thesis. Possible improvements of the realizable surface

roughness figures may be achieved by alternating the scan sense or by using the alternate wavelength of the CO2 laser. Furthermore, the effect of high-temperature annealing on the waviness and roughness of the substrates can be investigated. Another possible polishing strategy is to work with a pattern of single, overlapping pulses instead of *cw* lines. In addition to the AFM, SEM measurements could be realized by applying a thin gold coating onto the substrates.

3.4 Machining large spherical structures via laser dot milling

3.4.1 Technical challenges of the dot milling technique

Material volume to be removed: Challenges compared to previous large multi-shot structures come from the volume to be removed from the fiber tip. The structure published in [136] required $\approx 3000\,\mu m^3$ of material to be removed whereas the structure derived in chapter 4 sums up to $\approx 11\,000\,\mu m^3$.

The obvious strategy would be to simply increase the number of shots per structure while working with the experimental parameters as in [136] which already lead to decent results. The trade-off is the increased fabrication time per structure. Not only does a large number of shots slow down pattern optimization procedure, but

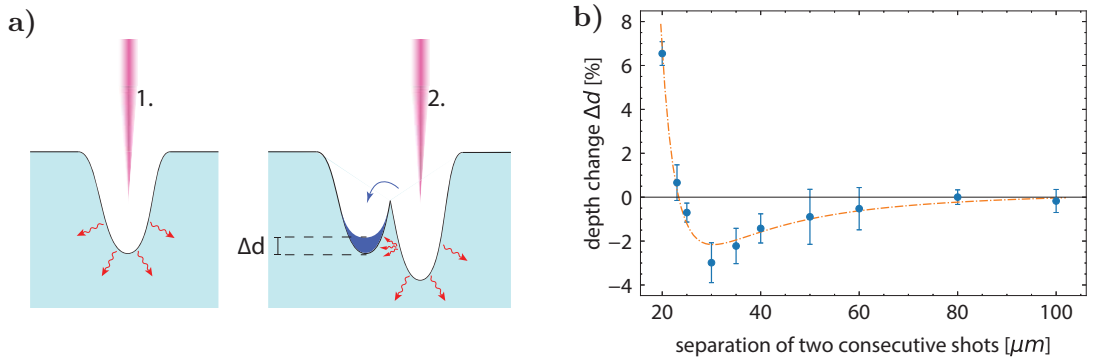

Figure 3.4.1: a) The rose-colored arrows represent the pulses of the CO_2 dot milling setup, which deposit heat into the substrate (cyan). The head dissipation (illustrated by the red arrows) is disturbed by presence of first depression which leads to a deeper second structure. If the two consecutive shots are close enough, melted glass flows into the first structure (blue region), which decreases its structure depth by Δd. b) The blue dots are experimental data averaged over five measurement and the dashed line is a $a/x^2 + b/x^6$ fit for visualization purposes.

does it also imposes even more strict stability requirements on the experiment, such as on temperature, vibration isolation and humidity.

Interacting shots: As described in section 3.1, a single CO_2 pulse is absorbed at the surface of a plane fused silica substrate and the heat dissipates homogeneously into the bulk material. When now a second pulse hits the surface close to the location of the previous one, the depression caused by the first laser pulse leads to an inhomogeneous heat dissipation. As a consequence, the depression of the second pulse is much deeper than the first one (as depicted in figure 3.4.1a).

Another observable effect when studying the interaction of two consecutive shots is that the second shot tends to fill up the previous depression with melted material. The figure 3.4.1b shows the depth change Δd of the first structure in percent. A single shot lead to a depression of 0.6 µm depth and a $1/e^2$ structure diameter of 23 µm. The CO_2 laser beam had a $1/e^2$ spot radius of $w \approx 100\,\mu$m on the substrate surface. When the separation of two consecutive shots approaches the $1/e^2$ structure diameter of 23 µm, the fill-up effect increases before both structures overlap. An depth reduction of up to 3 % was observed.

Re-deposition of ablated material: Besides, the occurrence of a convex depression around the principal Gaußian depression ('*crater halo*'), which can be related to the increased silica density for higher fictive temperatures at higher laser intensities [154], a re-deposition of ablated material around the impact region can be observed as well. This contamination can lead to a reduction of surface quality and has an impact on the finesse of CO_2 machined micro-cavities [155]. For visualization purposes, a ring (100 μm in radius) of twelve shots with a depth of 1.5 µm has been shot around a central depression. As can be seen from figure 3.4.2, ablation debris deposits at higher CO_2 laser intensity in the central region even though the depth of the ring was kept constant compared a ring shot at lower intensity. It is therefore advisable to work with lower laser intensities and longer pulse lengths.

This phenomena might occur from the reflow fraction in the Knudsen layer [156] and from the diffusive vapour where the higher gas density leads to elastic collisions which also slows down the expansion of the cloud [157]. Besides reducing the CO_2 laser intensity, a vacuum nozzle could be placed in the proximity of the target in order to reduce the redeposition of debris on the target surface.

Optimizing shoot pattern: The CO_2 dot milling technique is a eminently nonlinear process. The lack of an analytical model predicting the machined structure of overlapping pulses requires a lot empirical optimization of shoot pattern. An exemplary shoot pattern is shown in figure 3.4.3a. A typical shoot pattern consists of six rings and the parameter space of possible combinations can easily exceed

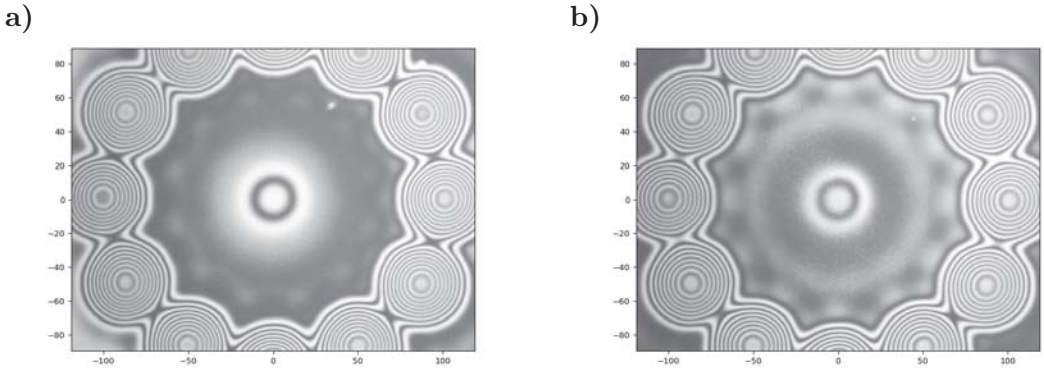

Figure 3.4.2: Profilometry pictures for a) low power/long pulse length (1480 mW/25 ms) and b) high power/short pulse length (1830 mW/8 ms).

10^{20}. The fact tht no analytic model exists that predicts the ablation results in all scenarios, espeicially in the particular case of the modified heat dissipation in proximity of the fiber edge, finding an appropriate shoot pattern for machining large mirror structures remains a mayor challenge.

A recent publication about a thermo-mechanical numerical simulation shows promising results for the case of a single pulse and a moving beam [141]. How these simulations can extended to overlapping pulses in the vicinity of close borders as for the case of fibers, remains an open question.

A crucial paramter is obviously the number of shots per structure, which depends on the CO_2 laser power and its pulse length. By averaging over a large number of weak shots, the impact of a single shot on the entire structure can be drastically reduced but it increases the fabrication time and the impact of long-term drifts of the experiment. A small number of shots, however, is more sensitive to short-term fluctuations of the experiment and can also lead to debris on the target structure. Besides the actual shoot pattern, an additional '*annealing pulse*' can be applied to the structure (see figure 3.4.3b). For this purpose, the substrate is moved far away from the CO_2 laser waist and due to the small intensity of the beam with a large diameter, the pulse length is increases. The idea of this annealing pulse is that it melts slowly the structure surface without evaporating material and reduces thus the height of any remaining defect.

3.4.2 Fiber results

As discussed in more detail in section 4.4, the fabrication goal was to obtain spherical mirror profiles with ROCs of 360/270 μm over a mirror diameter of 90 µm

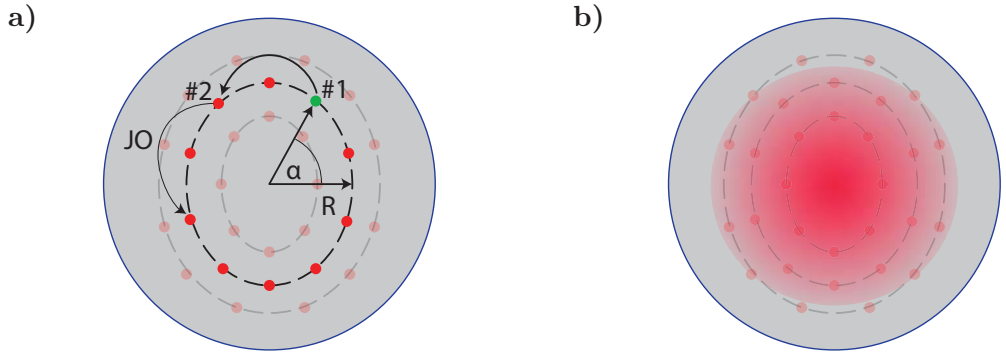

Figure 3.4.3: a) The grey circle illustrates the surface of a cleaved fiber and the red dots illustrate the positions of each laser pulse. R is the radius of the ring, α is the angle of the first pulse (green dot) of the ring and JO stands for the jump-over. b) Illustration of the large-diameter annealing shot.

on a cleaved fiber tip[18]. The fiber is a multi-mode fiber with a large core diameter (200 µm) to provide a homogeneous target for the laser machining as the core-cladding interface leads to systematic defects on the machined structure.

The results presented in the following were obtained for the following setup parameters. The laser power was set to $P = 1700\,\mathrm{mW}$ on the fiber tip and the laser beam $1/e^2$ radius was $w \approx 100\,\mu\mathrm{m}$. The impact of single pulse in the fiber center lead to a structure depth of 0.2 µm and a structure diameter of $2\sigma = 20\,\mu\mathrm{m}$ (obtained from a Gaußian fit). The resulting ROC of a single shot is thus close to the desired large structure [148]. The pulse length was in the range of $12\,\mathrm{ms} \leq \tau \leq 15\,\mathrm{ms}$.

The optimized pattern is presented in figure 3.4.4b. It consists of six rings which are shot successively starting with the outermost one. A single structure needs in total 189 single shots. The circular shoot pattern was then scaled in x/y-direction by a factor of 0.91/1 to obtain the ellipticity that is required to compensate for the astigmatism of the triangular ring cavity (see subsection 4.2.1).

The fiber presented in figure 3.4.5a has ROCs of $R_{\mathrm{x/y}} = 269/344\,\mu\mathrm{m}$, which deviates slightly from the ideal ratio of 0.75. The residuals from a 2D spherical fit over a circular region of interest (ROI) of 45 µm are shown figure 3.4.5b and amount to $\sigma_{\mathrm{mean/RMS}} = 7.7/10.4\,\mathrm{nm}$. The rms noise of the profilometry is on the order of 3 nm. The noise orignates from two contributions: first from the interference fringes leading to artifacts of the profile reconstruction algorithm. Second, from the intial z-position of the profilometry, i. e. the position of the

[18] IVG Cu200/220

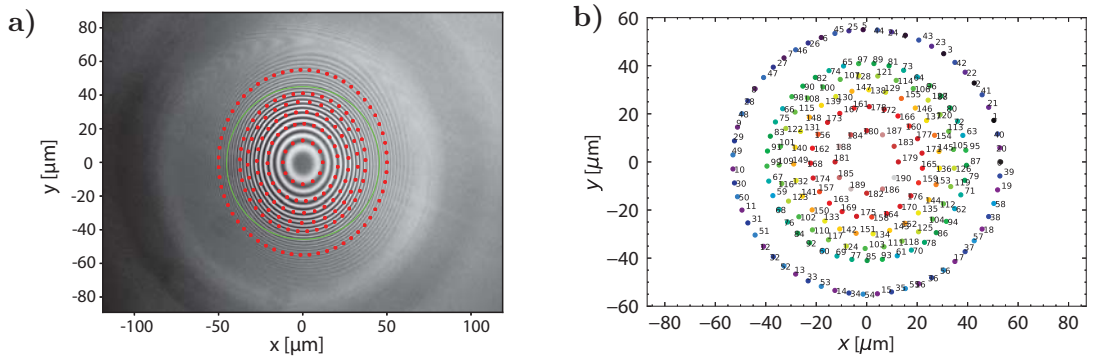

Figure 3.4.4: a) shows a machined fiber with the corresponding shoot pattern (red dots) and the effective mirror diameter (green circle) and b) depicts the final, optimized shoot pattern.

highest fringe contrast. As the presented structures are relatively deep, the initial position was set further to the wings of the structure in order to able reconstruct them. This misalignment of the optimal profilometry position leads to an increase of profilometry noise as investigated in [148]. This explains also the decrease of the fit residual towards ROI = 20 μm in figure 3.4.5c

3.5 Potential estimation of convolutional neural networks for a faster pattern optimization in the context of CO_2 mirror fabrication

Machine learning aims to generate 'knowledge' from 'experience', as learning algorithms develop a complex model from data. The model, and thus the automatically acquired data representation, can then be applied to new, potentially unknown datasets of the same kind. Whenever processes are too complicated to be described analytically, but enough sample data - such as sensor data, pictures or texts - is available, machine learning can be an appropriate tool. With the models learned, predictions can be made or recommendations and decisions can be generated - without pre-defined calculation rules.

These techniques are widely used in high-energy physics since almost two decades and became a popular tool in computer science in the context of computer vision, language processing and many others. Current uses of machine learning can be divided into three different classes: *classification*, *regression* and *data generation*.

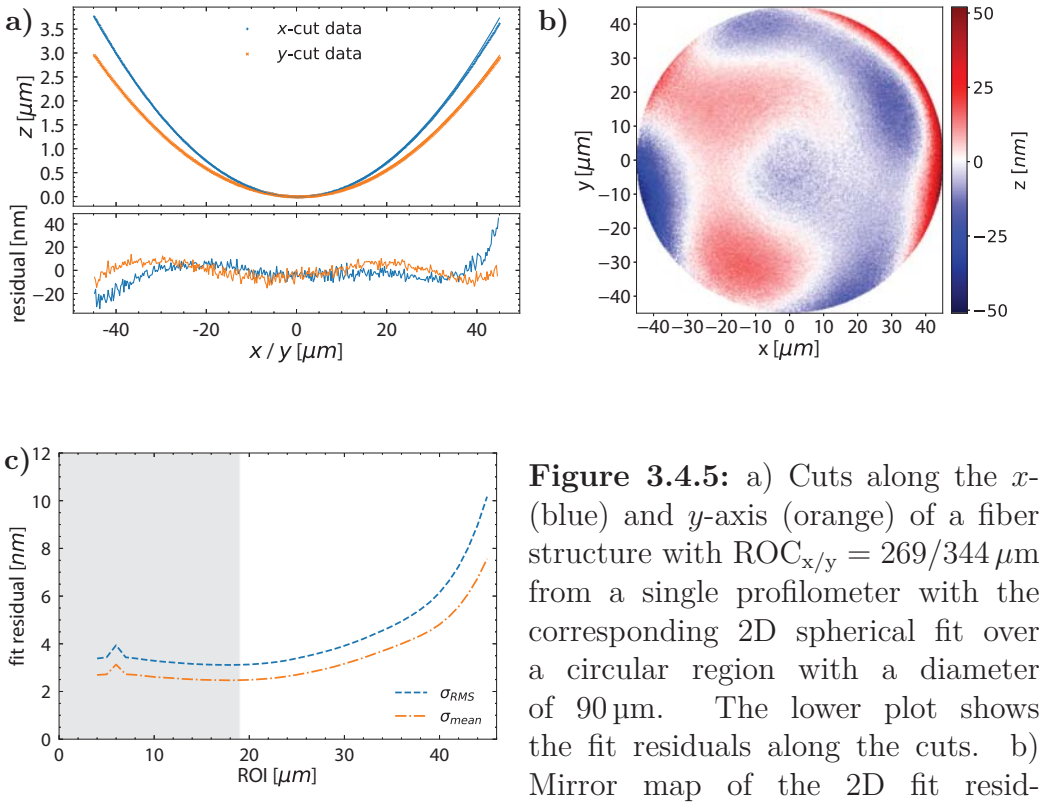

Figure 3.4.5: a) Cuts along the x- (blue) and y-axis (orange) of a fiber structure with $\mathrm{ROC_{x/y}} = 269/344\,\mu\mathrm{m}$ from a single profilometer with the corresponding 2D spherical fit over a circular region with a diameter of 90 µm. The lower plot shows the fit residuals along the cuts. b) Mirror map of the 2D fit residuals. The profile deviations are $\sigma_{\mathrm{mean/RMS}} = 7.7/10.4\,\mathrm{nm}$. c) Shown is the surface fit residual for different fit diameters. Grey region corresponds to the beam radius on the mirror.

The regression involves the prediction of a set of continuous numbers and was hence chosen for prediction of shoot patterns.

Also, many different machine learning architectures had been developed over the last years. Even though their working principle differ drastically from each other, they all have the same purpose: to learn a target function f that best maps some input variables x to an output variable y. This is often realized in a supervised learning strategy, where each sample in the dataset is a pair of an input and output vector. In this work, common *Convolutional Neural Network*s (CNN) were adapted to test its potential in the context of an improved pattern optimization for the CO_2 fabrication of large mirror structures.

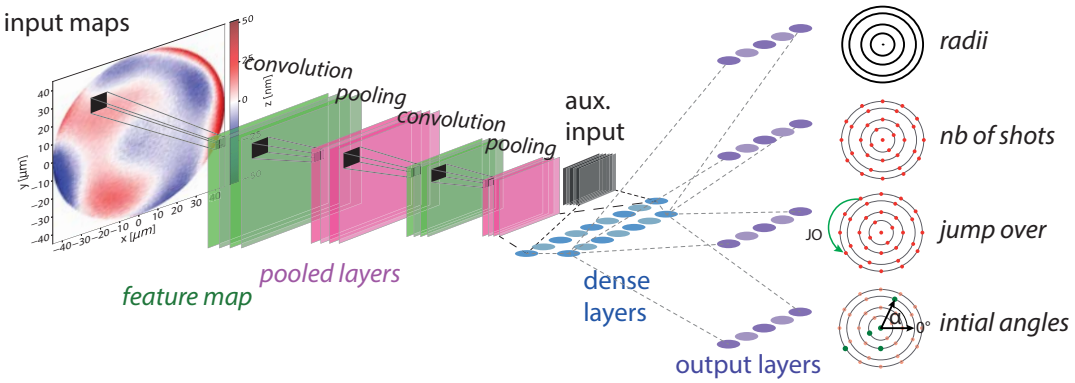

Figure 3.5.1: Working principle of a CNN algorithm.

3.5.1 Designing a convolutional neural network

The processing of high-dimensional natural data, such as photos or language, is of great interest in data science and has also led to many industrial applications. Popular examples are data processing algorithms for automatic speech recognition or real-time picture analysis for autonomous driving. A powerful approach for data processing are CNNs – a special type of artificial neural networks whose underlying ideas are discussed in this chapter.

Similar to an image recognition classifier algorithm, a neural network has been designed which, based on the 2D-residual mirror map, learns to predict the shoot pattern that is required to fabricate a given residual mirror map. The residual mirror map was chosen over the actual fabricated structure as the depth and thus the ROC of a machined structure has usually a non-negligible spread around their design values. The residual map, on the other hand, is relatively unaffected by these technical fluctuations.

Besides the mirror maps, some auxiliary structure information are fed to the network and concatenate with the CNN. The global parameters are the ROCs from fit, the CO_2 laser power and the x/y-deviation from the fiber center, which has no effect in the case of a large fused silica plate but is an even more important information for finite fiber surfaces. The output consists of four vectors, corresponding to the radii of the shoot pattern rings, the number of shots per ring, their jump-overs and the initial ring angles. An illustration of the CNN is shown in figure 3.5.1.

The choice of the CNN lies in the nature of the inputa data. A CNN is able to process input in the form of a matrix, such as the residual mirror map. A normal neural network would require a vector as input, so that the pixels of an image would need to be rolled out in in a long chain. On the following pages, the

essential components of a CNN are introduced.[19]

Convolutional layer: As its name already suggest, the main operation of a CNN consists of the convolution of data. The matrix input is first analyzed by a fixed number of so-called filters. That is why the convolution in figure 3.5.1 is not represented by a single rectangle but rather by a stack of rectangles. The third dimensions represents here different filters that were applied to the input matrix. Depending on the problem, i. e. if a big amount of pixels are required for the network to recognize the object you of interest, the kernel size of the applied filter is set (typically ranging from 2×2 to 11×11 pixels). The kernel acts like a window on the input matrix, which is then slide over the matrix with a constant step size. The filters move from left to right across the input matrix and jump to the next lower line after each run.

Let $A = (a_{ij}) \in K^{n\times n}$ be the input matrix and $F = (f_{ij}) \in K^{m\times m}$ with $m < n$ the filter or kernel matrix, then the 2D convolution is defined as

$$A * F := (a * f)_{xy} = \sum_{i=1}^{k}\sum_{j=1}^{k} a_{(x+i-1)(y+j-1)} \cdot f_{ij} \tag{3.5.1}$$

with $x, y \in \{1, \ldots, n-k+1\}$. Depending on the choice of the filter matrix, the convolution allows to process images in different ways. The probably most known matrix filters are picture sharpening or blurring. However, the goal of a CNN is not to work with a set of pre-defined filters but to let the CNN develop its own filters.

The convolution results in a new matrix, called feature map, whose size depends on the kernel size and the step size. For example, for a step size of 2 and a kernel size of 2×2, the size of the resulting matrix per filter is smaller compared to the input matrix. In this example, each input pixel is no longer necessarily connected to the filter individually, but in each case 4 pixels are simultaneously connected to the filter.

A CNN consist typically of many convolutional layers (depending on the complexity of the problem). The first layer, for example, has typically 8 or 16 filters, whose convoled output is then a new matrix. This first layer is usually followed by a second, equal built convolutional layer, which uses as input the new matrices from the convolution of the previous layer. This is followed by a pooling layer.

Spatial pooling: A pooling layer can be also referred to sub- or downsampling as it reduces ad-hoc the dimensionality of the feature maps while maintaining their information. The goal is to transfer only the most relevant information to

[19] The following summary of the principle CNN components is guided by [158].

the next layers in order to generate a more abstract representation of the input while reducing the number of parameters of the network. Spatial pooling can be subdivided into average, maximum and sum pooling. For example, a maximum pooling layer simply uses the highest value of a kernel matrix and discards all other values. The resulting matrix created by a 2×2 kernel is just one number.

Many CNNs consist of a stack of several convolutional layers each with the same number of filters, followed by a pooling layer, whose results is then again fed to another stack of convolutional layers. While the size of the input through the convolutions and the pooling is reduced further and further, the number of filters for detecting higher-level signals is successively increased. After the last pooling layer, one or more fully connected layers pursue.

Fully connected (dense) layers: Up to this point, the CNN has only done some 'deterministic' or algebraic computation. The only purpose of the convolutions is to generate data from 2D matrices, can be understood by the neural network. Or, in other words: after many convolutions, the output signal is cleaned up from spatial information of the very first matrix and contains only location-independent object information.

In order to be able to feed the matrix output of the convolutional and pooling layers into a dense layer, it is first flattened into a vector. Then, the dense layer is a standard neural network architecture in which all neurons are connected to all inputs and all outputs. The last layer in a neural network is the predicting output and has therefore the exact number of neurons corresponding to the number of different output variables.

Nonlinear activation functions: For an artificial neural network, the activation functions are of great importance as they help to learn and understand the non-linear complex functional mapping between the input data and the results. To understand what an activation is good for, it is important to understand what an artificial neuron does.

Each layer in a neural network consists of many neurons that act in parallel, where each neuron represents a vector-to-scalar function. In mathematical terms, a neuron is simply a mathematical function which provides an output by applying a function on the inputs provided. Each node calcualtes the affine transformation of its input vector $\mathbf{x}$

$$y = W^T \mathbf{x} + \mathbf{b}\,, \tag{3.5.2}$$

where the matrix W describes the mapping from $\mathbf{x}$ to y and b is a bias vector.

Afterwards, a non-linear function $g(y)$, called the activation function, is applied element-wise on y. This is necessary to obtain a non-linear functional mapping between the input and output. Otherwise, if no activation function would be applied

(equivalent to $g(y) = y$), all layers would simply stack one affine transformation after another. This, in the end, is equivalent to a single affine transformation.

In a CNN, the layers are mostly activated by a *rectified linear unit* (ReLU) function:

$$g(z) = z^+ = \max(0, z)\,. \tag{3.5.3}$$

The ReLU function assures that all negative values are filtered out. This is often called the *data sparsity* and ensures that not all neurons 'fire' every time they get an input. Instead, they have different roles and are activated by different signals. This increases the ability of the neural network to fit or train from the data more efficiently.

The activation function for the CNN of this work was a modified ReLU function, the 'swish' function [159]. The output layer, however, had linear activation functions as the CNN shall build a regression of data.

Loss function: A learning algorithm needs a metric in order quantify the capacity of the network to approximate the training data. Such a metric is called the loss function. Typical loss functions in regression problems are the *Mean Squared Error* (MSE) or *Mean Absolute Error* (MAE).

Optimizer: Machine learning is an iterative process and has many parameters to tune. Based on the loss function, an optimizer adjusts the parameter of the CNN. It is therefore important find an optimizer that converges quickly in the parameter space towards a global minimum in order quickly complete the iterative cycle. The *YOGI* optimizer [160] was chosen here.

3.5.2 Learning with CO_2-machined structures

Dataset preparation As machine learning requires a dataset to learn, 120 structures have been fabricated automatically on a fused silica plate with semi-arbitrary shoot pattern. The intended ROC was about 1100 µm over a diameter of 90 µm. However, constraints were put on the parameter space to simulate a manual shoot pattern optimization. The shoot pattern had to be composed of five rings, the maximum number of shots per structure was 86 and minimum 46. The number of shots decreased from the outer to the inner rings. The maximum radius was 45 µm. On the angle and the jump over, no constraints were given.

After post-selecting from 120 structures, 86 structures remained. The post-selection is necessary as the performance of CNN suffers from outliers, which arise from failed profilometries or donut-shaped structures with negative ROC.

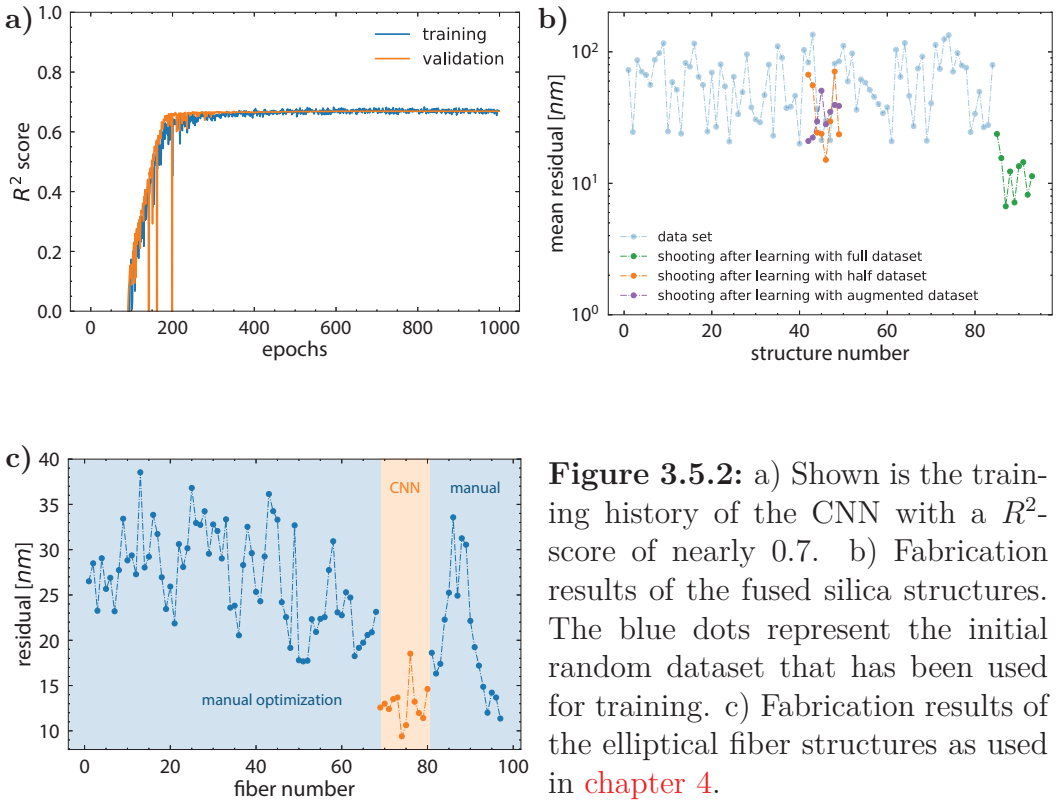

Figure 3.5.2: a) Shown is the training history of the CNN with a R^2-score of nearly 0.7. b) Fabrication results of the fused silica structures. The blue dots represent the initial random dataset that has been used for training. c) Fabrication results of the elliptical fiber structures as used in chapter 4.

Data preprocessing From each 2D residual mirror map, its mean pixel value was subtracted in order to standardize the input. Also, a *data augmentation* technique has been tested. The idea is to artificially increase the size of the dataset by readding the same data after rotating each 2D residual map by a given angle. This method doubles the amount of available data.

Eventually, the dataset was split into 80 % of training data and 20 % validation data. The validation data are excluded from the learning process and are used evaluate the prediction performance of the trained algorithm on 'unseen' data. The validation is applied after each iteration.

Results

The learning performance of the designed CNN is shown in figure 3.5.2a. After 1000 iterations (also called the *epochs*), the prediction performance of the algorithm on the unseen validation data reaches nearly 0.7 measured by means of the R^2-score. The R^2 is a statistical measure for the assessment of the fit quality of a

regression model. Another way to quantify the prediction performance is to look in the *root mean squared error* (RMSE) per ring. The RMSE of the validation data is $\sigma_R \approx 1\,\mu$m, $\sigma_{\text{NbShots}} \approx 1$, $\sigma_{\text{JO}} \approx 0.4$ and $\sigma_{\text{angle}} \approx 38°$.

After training the algorithm, the trained model was used to predict a shoot pattern for a perfect structure. For that purpose, the trained model was fed with a flat 2D residual array with 1 nm of Gaußian noise[20]. The resulting pattern was then fabricated and the result added to the dataset. The updated dataset was then used for another training cycle of the CNN.

The CNN working with the full dataset, i. e. 86 structures, achieved a three-fold improvement the 2D surface fit residual. The best structures from arbitrary shooting have a mean residual of $\sim$ 20 nm, whereas the structures from the predicted pattern reached a minimum of $\sim$ 6 nm after three training cycles. The reduced dataset did not bring any improvement. Same for the data augmentation technique. The remaining question is if a optimization of the CNN for the small dataset would lead to better results or if there is minimum amount of data required to improve the surface residual.

A more powerful approach would be not to optimize the meta-variables of the shoot pattern generation, but to use the x-y-positions coordinates of each individual shot. The reason is that an optimum shoot pattern does not necessarily need to be radially symmetric. Throughout this thesis, this approach has been tested but no CNN architecture was found that out-performed the CNN presented in this section.

Furthermore, this method had been adapted to the pattern optimization of the elliptical mirror structure presented in subsection 3.4.2. This machine learning optimization allowed to fabricate the fiber mirrors that will be utilized to build the miniaturized high-finesse ring cavity. For that purpose, the algorithm was fed with almost 70 fibers structures, whose best fit residual is $\sigma_{\text{mean}} \approx 18$ nm over a fit diameter of 60 µm. A fit diameter smaller than the actual mirror diameter was chosen in order to account for the strong influence of the fiber borders on the shoot result. The best predicted shoot patter of the algorithm with $\sim$ 9 nm is twice as good as the manually optimized fibers before (see figure 3.5.2c). Even trying to improve the shoot pattern afterwards by hand did not lead to any success.

Eventually, the best predicted shoot pattern was kept and the annealing shot was add to the fabrication. After optimizing the diameter and pulse length of the annealing shot, the fiber mirror results presented in this chapter were obtained and will be used to assemble the high-finesse ring cavity.

[20] The artificial Gaußian noise accounts for the profilometry noise.

Conclusion

This work shows that machine learning can improve the pattern optimization for the fabrication of large mirror structures by CO_2 dot milling to some extend. Nevertheless, it is important to state that this work is only a proof-of-principle and no ultimate conclusion about its full potential. The data science domain has developed many techniques and algorithms that show great performance and exceed the complexity of the basic algorithm presented here. Also, an alternative to the CNN of this work can be 'deep reinforced learning'. Usually, supervised learning requires a huge dataset to work properly. Reinforced learning algorithms however are a more dynamic way of learning and come into play where data-efficiency is critical [161], as it is in the case of CO_2 dot milling projects. Producing a dataset of more than 1000 fiber structures would require about two month of fabrication but is also the number of structures that is usually necessary to optimize a pattern by hand.

Even though the group disposes of a huge stock of data of fabricated structures as several CO_2 dot milling projects had been realized already, they all lack of one important information: the spot-size of the CO_2 laser beam on the fiber tip. This information however is crucial for fabricating these structures. But it might be interesting though if even without this information, a CNN could be trained with all of these data.

3.6 Integrated mode-matching for open fiber cavities

A very promising upgrade for the next generation of miniaturized cavities is the integration of mode matching optics onto an optical bench. This can potentially improve the compactness and stability of resonators. Besides GRIN rod lenses and CO_2 machined aspheric lenses on fused silica in miniaturized open cavity systems, the best candidates to adapt the singlemode (SM) fiber mode to a resonator's mode are graded index (GRIN) fibers.

Due to the high divergence angles of small optical beams and the limited availability of large *mode field diameter* (MFD) fibers, the optical coupling between optical fibers and fiber Fabry Pérot cavities decreases drastically if the length of the cavity increases. Micro-lenses allow to adjust the beam waist and increase the coupling between the coupling fiber and the cavity.

GRIN fiber lenses have been already reported in 1987 [162] and are widely used in optical components and devices as collimating, focusing and coupling lenses [163–166].

3.6.1 Graded index fibers

Optical fibers can be roughly divided into two categories: step index fibers that consist of a fiber core and a surrounding cladding with a slightly lower refractive index than the core, including multimode (MM) and SM fibers. The second group of fibers are graded index (GRIN) fibers, which have a core with a continuously changing refractive index. In a GRIN fiber, the law of refraction applies at every point, which causes the light in the fiber to be continuously deflected. According to Fermat's principle, light propagates in an inhomogeneous medium such that the optical path AB along a geometric path S_0 from adjacent paths takes the minimum:

$$\left(\frac{\delta \overline{AB}}{\delta S}\right)_{S_0} = \delta \int_A^B n(s)\,\mathrm{d}s = 0\,. \tag{3.6.1}$$

A typical GRIN lens has an index of refraction whose value varies with radial distance from the fiber axis, ideally a quadratic variation. The refraction index profile can be then approximated by [162]:

$$n(r)^2 = n_0^2\left(1 - g^2 r^2\right)\,, \tag{3.6.2}$$

where n_0 is the refractive index on the core axis, r is the radial distance from the core axis, and g is the focusing parameter that is defined as

$$g = \frac{NA}{a \cdot n_0}\,. \tag{3.6.3}$$

Here, $\mathrm{NA} = \sqrt{n_0^2 - n_{\mathrm{clad}}^2}$ is the numerical aperture of the GRIN fiber for a refractive index of the fiber cladding n_{clad} and a the fiber core radius.

As a consequence, rays that are coupled into a GRIN fiber within its NA are always refracted towards the fiber core and thus follow sinusoidal paths until they reach the back surface of the fiber (figure 3.6.1a). A characteristic property of GRIN fibers is the distance a light ray needs to traverse one cycle of the sinusoidal wave, the pitch length p. The pitch length is defined as

$$p = \frac{2\pi}{g}\,. \tag{3.6.4}$$

The ray-matrix formalism of Gaußian beam can be used to derive analytical expressions of the beam waist and the working distance of different SM-GRIN configurations. The corresponding transfer matrix M_{g} of a GRIN fiber of length

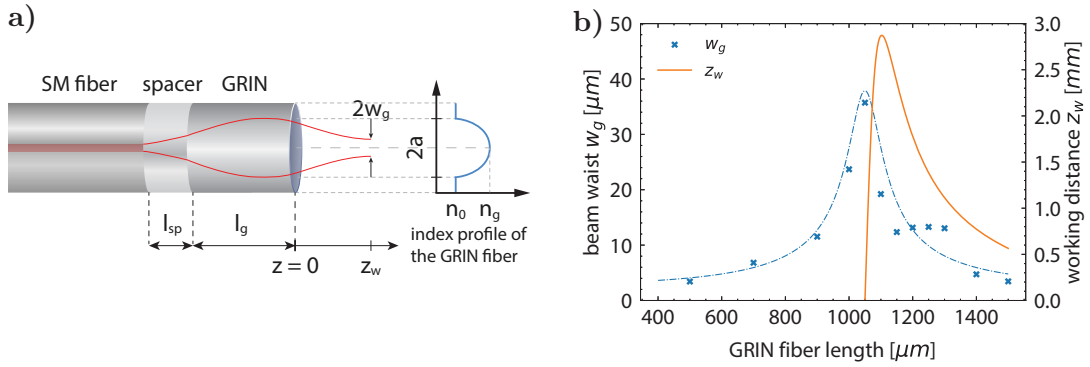

Figure 3.6.1: a) Trajectory of a ray and refractive index distribution of a GI fiber with parabolic index distribution. b) The dashed blue line shows the calculated waist for $p/4 = 1050\,\mu$m and MFD $= 6\,\mu$m of the SM fiber.

l_g is:

$$M_\mathrm{g} = \begin{pmatrix} A & B \\ C & D \end{pmatrix} = \begin{pmatrix} \cos(gl_\mathrm{g}) & \frac{1}{g}\sin(gl_\mathrm{g}) \\ -g\sin(gl_\mathrm{g}) & \cos(gl_\mathrm{g}) \end{pmatrix} . \tag{3.6.5}$$

Starting with a Gaußian beam at the end of a SM fiber, assuming that its beam waist has its minimum value w_0 at its output plane, the beam waist w_g and working distance z_w after the output plane of the GRIN fiber without concave interface for wavelength λ become

$$w_\mathrm{g} = \frac{2a_0 w_0}{n_0 g\sqrt{\sin(gl_\mathrm{g})^2 + \left(\frac{a_0}{n_0 g}\right)^2 \cos(gl_\mathrm{g})^2}} \quad \text{and} \tag{3.6.6}$$

$$z_\mathrm{w} = \frac{\left[1 - \left(\frac{a_0}{n_0 g}\right)^2\right]\sin(gl_\mathrm{g})\cos(gl_\mathrm{g})}{n_0 g\left[\sin(gl_\mathrm{g})^2 + \left(\frac{a_0}{n_0 g}\right)^2 \cos(gl_\mathrm{g})^2\right]} \tag{3.6.7}$$

with a_0 given by

$$a_0 = \frac{\lambda}{\pi w_0^2} . \tag{3.6.8}$$

Beside GRIN MM optical fibers, conventional bulk GRIN lenses are often used in fiber collimation setups. However, they give rise to a series of disadvantages, e. g. much bigger size than SM fibers, higher cost and UV glued fiber-lens interfaces instead of stable fused interfaces. Also, common GRIN lenses are made from borosilicate glass with an index gradient produced by ion exchange. Therefore,

GRIN lenses are not compatible with the CO_2 machining setup and the index gradient does not withstand the elevated temperatures that occur during the coating process.

Adding a coreless fiber

One remaining problem of a simple SM-GRIN assembly is the mismatch between their mode fields as the NA of SM fibers (typically 0.13) is much smaller than the NA of a GRIN fiber (typically 0.2 to 0.4). Considering a standard SM fiber with MFD = 6 μm and a GRIN fiber as used for the test in subsection 3.6.2, the beam expands to a diameter of ≈80 µm, whereas the GRIN core has a diameter of 200 µm. In order to allow the optical beam to expand to the entire core of the GRIN fiber, which results in an increased working distance of the optical assembly, a coreless fiber section[21] can be inserted between the SM and the GRIN fiber. By inserting e. g. a 1.6 mm long coreless fiber, the beam exploits the entire GRIN fiber cross-section and the working distance can be extended up to ≈15 mm.

3.6.2 Experimental test

For the following results, a GRIN fiber[22] with a large core diameter of 200 µm has been used as a large cross section is necessary for the large mirrors of long fiber cavities.

Determination of the pitch-length

Before being able to design a mode-matched GRIN fiber cavity, the pitch length p needs to be determined. For that purpose, GRIN fibers were spliced to a SM fiber[23] and then cut at the desired length with a fiber cleaver[24].

The beam waist was measured at the end facet of the GRIN fiber by use of a CMOS camera[25]. In the far field, the measured Gaußian beam width grows linearly as a function of distance from the GRIN collimator. The divergence angle of the output beam can then be calculated based on the derivative of the Gaußian beam width with respect to the distance that the collimator moves according to the following equation [167]:

$$\tan\theta_{\mathrm{div}} = \frac{w(d_2) - w(d_1)}{d_2 - d_1} \tag{3.6.9}$$

[21] for example Thorlabs FG200LEA
[22] LEONI Fiber Optics GmbH; I-V(ZN)Y(ZN)11Y 2GK200/230 GI-PCF
[23] IVG Cu800/200
[24] Nyfors AutoCleaver; $\Delta l_{\mathrm{g}} = \pm 10\,\mu$m
[25] Thorlabs, DCC1545M

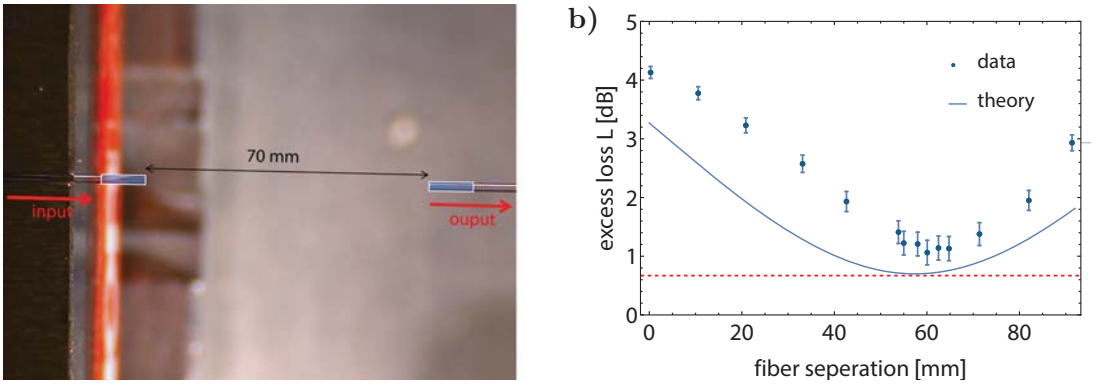

Figure 3.6.2: a) Photo of two CU800/200 SM fibers with a 1100 µm long GRIN pieces (blue squares). b) Corresponding measurement of the excess loss depending on the fiber separation. The red dashed line represents the maximally achievable fiber-to-fiber coupling considering 0.4 dB of reflection at the air-fiber interface and 0.3 dB of splice losses.

where $w(d_1)$ and $w(d_2)$ are the Gaußian beam widths at distance d_1 and d_2, respectively. The beam waist after the GRIN fiber can be then calculated as $w_g = \frac{\lambda}{\pi\theta_{\text{div}}}$.

The calculated beam waist is plotted against the GRIN length in figure 3.6.1b. It reaches it maximum at the quarter pitch length which is at $p/4 = 1050\,\mu$m. By using equation 3.6.6 the maximal working distance of 2.9 mm for this particular SM-GRIN fiber combination is reached at a GRIN length of $l_g = 1100\,\mu$m.

By choosing a SM fiber with different MFD or adding a coreless fiber between the SM and GRIN fiber (as depicted in figure 3.6.1a) or even after the GRIN fiber, the working distance and the beam waist after the lens can be adjusted. This allows for optimal beam shaping of the input beam to a potential cavity mode.

Coupling efficiency between two lensed single-mode fibers

In order to evaluate the potential of GRIN fibers for mode-matching, the ability of the SM–GRIN fiber probes to couple light back into another SM-GRIN probe has been measured. The optimal coupling is reached when the second GRIN fiber lens refocuses the beam to nearly its original diameter.

Theory High coupling efficiencies of beams into optical SM fibers are not only achieved by focusing the beam onto the fiber with a low amount of aberration, but the beam must match the fundamental mode of the fiber. The on-axis coupling

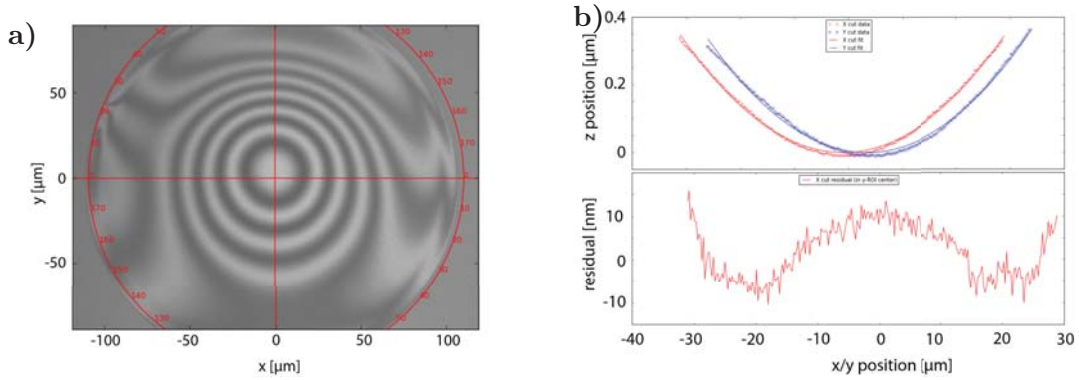

Figure 3.6.3: a) Profilometry picture of a machined GI fiber tip. b) Cuts through the machined structure and the corresponding residuals of a 2D spherical fit.

efficiency η is calculated by the so-called '*overlap integral*' as

$$\eta = \frac{\left| \int_{-\infty}^{\infty} \int_{-\infty}^{\infty} E_i(x,y) E_f^*(x,y)\, \mathrm{d}x\, \mathrm{d}y \right|^2}{\int_{-\infty}^{\infty} \int_{-\infty}^{\infty} |E_i(x,y)|^2\, \mathrm{d}x\, \mathrm{d}y \int_{-\infty}^{\infty} \int_{-\infty}^{\infty} |E_f(x,y)|^2\, \mathrm{d}x\, \mathrm{d}y}\,, \tag{3.6.10}$$

where η is the fraction of power from the incident beam that couples into the output fiber. $E_i(x,y)$ is the complex field distribution of the incident beam to be coupled and $E_f(x,y)$ is the complex field distribution of the receiver fiber mode. For two Gaußian modes, the fiber-to-fiber power coupling efficiency from equation 3.6.10 can be approximated for a non-astigmatic beam by [168]

$$\eta = \frac{4}{\left(\frac{w_i}{w_f} + \frac{w_f}{w_i}\right)^2 + \left(\frac{\lambda \cdot s_z}{\pi w_i w_f}\right)^2} \cdot (1 - R)\,, \tag{3.6.11}$$

where w_i is the waist radius of the in incident beam, w_f the waist radius of the receiving fiber, s_z is the distance between the two waist positions and R the fraction of power reflected and the end facets of the receiving fiber.

Measurement The figure 3.6.2a shows the essence of the test set used to measure the fiber-to-fiber coupling efficiency of GRIN fiber lenses. Based on the results from the pitch-length measurement, two 1100 µm long GRIN fiber pieces were spliced onto two SM fibers. Laser light at $\lambda = 780$ nm was coupled into one fiber and the optical power P_{in} after the first GRIN fiber was measured. Then, the second fiber

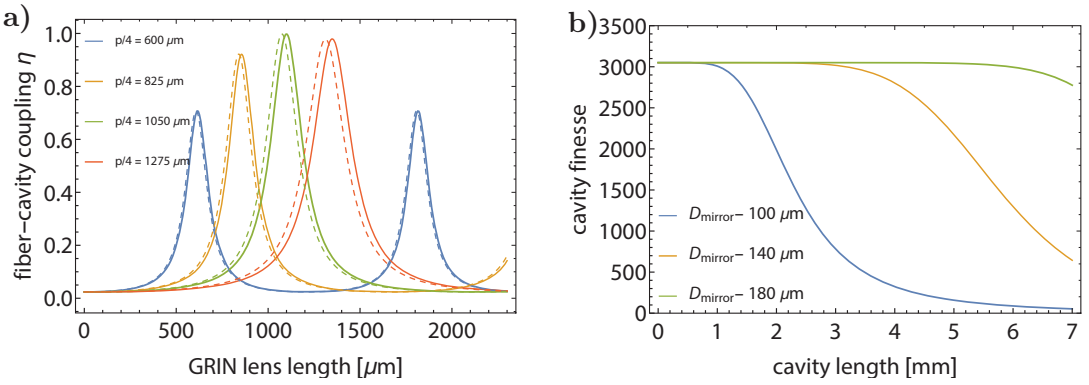

Figure 3.6.4: a) The plot shows the mode coupling for different GRIN lenses to a fiber cavity of length $L = 6\,\mathrm{mm}$. The lens with a pitch length of $p = 4 \cdot 1150\,\mu\mathrm{m}$ can realize couplings close to $\eta = 1$. The dashed lines show the same GRIN lenses but taking the lensing effect of the concave structure (ROC = 6 mm) into account. It can be seen that the structure lensing can be compensated by a different lens length. b) Clipping losses for a cavity with $L = R = 6\,\mathrm{mm}$ and a coating transmission of 1000 ppm. The losses are shown for different effective mirror diameters.

was carefully aligned to the first fiber in order to achieve maximal coupling of the light. The total light power P_{out} was measured at the output of the second fiber. The optical excess loss in decibels was computed as

$$L(\mathrm{dB}) = -10\log\left(\frac{P_{\mathrm{out}}}{P_{\mathrm{in}}}\right) = -10\log\left(\eta\right)\,. \tag{3.6.12}$$

From figure 3.6.2b it can be seen that an effective fiber-to-fiber coupling of 78 % was reached, what is close to the maximal possible coupling when considering 0.4 dB of losses by reflection at the air-fiber interface of the receiving fiber and furthermore 0.3 dB of losses due to splice imperfections. Further insertion losses might come from the axial misalignment of the spliced SM and GRIN fiber and their corresponding the cleave angles. Also, an inhomogeneous heat distribution inside the GIF during the splice procedure can lead to a disturbances of the index profile and thus to an astigmatic output beam.

3.6.3 CO_2 machining of large mirror structures on GRIN fibers

To evaluate the compatibility of GI fibers with the CO_2 machining setup presented in section 3.2, preliminary test has been performed. The same shoot pattern

as presented in [136] was used to evaluate if any influence of the graded index profile can be observed compared to results of MM or LMA fibers. The fabricated structure profile is shown in figure 3.6.3a. An effect of the higher refraction index at the fiber center is clearly visible from the structure cuts, but no major difficulties were encountered.

3.6.4 Conclusion

The work presented here shows that GRIN fibers are a rather promising candidate to push the state-of-the-art fiber Fabry-Pérot (FFP) cavities. They lead to a drastic increase in mode matching of a standard SM fiber to a (long) FFP cavity and are compatible with all required tools for fiber processing.

To the knowledge of the author, only one GRIN FFP cavity has been realized so far in a cold atom experiment [169], reaching up to 90 % of mode matching for a cavity length of 400 µm at a finesse of 50 000. Apart from cold atom experiments with elongated clouds, one of the most interesting applications of long FFP cavities could be filter cavities.

To meet the specifications of typical filter cavities (FSR = 25 GHz, $\mathcal{F} = 3000$), a confocal FFP cavity of $L = \mathrm{ROC} = 6\,\mathrm{mm}$ would be required. figure 3.6.4a shows the mode coupling of a standard SM fiber with a MFD of 6 µm and to a cavity of the length $L = 6\,\mathrm{mm}$ for different pitch length. By using the GRIN fiber characterized in this chapter, a coupling of more than 99 % can be reached. However, these FFP would require effective mirror diameters of 180 µm to not be limited by clipping losses (see figure 3.6.4b), which exceeds the 100 µm realized so far.

Chapter 4

An open, compact ring cavity

Optical resonators have numerous applications, probably most notably as the feedback mechanism in laser oscillators. In atomic physics laboratories, they are also used for optical spectrum analysis, a stable frequency reference for laser frequency stabilization and for enhancing 1D lattice traps.

Many of these applications benefit from an increased compactness of Fabry-Perot resonators, which leads to a smaller apparatus size and increased stability. If the application demands a high finesse or access to the resonator mode, like in spectroscopy, the use of an open resonator is favorable. The prerequisite for open high finesse resonators are high-quality mirrors meeting strict specifications regarding surface shape and roughness.

Despite the efforts towards miniaturized linear open cavities [146, 149, 169], the miniaturization aspect has not been extended to open ring cavities yet. Ring cavities differ from the commonly used Fabry-Perot design by its additional degree of freedom to switch between traveling and standing wave behavior and possess many other attributes that are exploited e. g. in laser and interferometer applications.

Despite the apparent greater simplicity of the two-mirror standing-wave cavity, there are several motivations behind the idea of compact ring cavity:

- A ring cavity features a traveling wave, which ensures *de facto* a spatially uniform coupling of the atomic ensemble to the light field. Nevertheless, a ring cavity can also be used in a standing-wave configuration by injecting a counter-propagating field.
- The CO_2 fabrication counters the intrinsic presence of an astigmatic mode field, arising from an off-axis mirror.
- The realization of a miniature ring cavity assembly can be seen as a proof of principle for the realization of more complex optical benches for cold atom experiments, moving away from linear fiber cavities.

Ring resonators are widely used for laser gyroscopes. By taking advantage of the Sagnac effect, rotation speeds can be measured. For this purpose, a ring resonator is pumped on both sides by a laser is rotated perpendicularly to the laser's propagation plane and due to the Doppler effect, the resonance frequencies and the phases of the opposite modes shift. The measured frequency shift is proportional to the rotational speed.

In the field of AMO physics, travelling wave ring cavities have been already used to realize spin squeezing [170]. Their homogenous atom-cavity coupling is also required to simplify the data analysis of squeezing experiments [171], as the thermal distribution of atoms in a 1D lattice leads to a large distrubtion of the coupling strength g. Therefore, the new strontium experiment presented in chapter 2 will host a ring cavity in its final stage.

This chapter examines the general resonator properties, which led to the development of a miniaturized open ring cavity for the new strontium cQED experiment. This will enable investigations of cavity-assisted multi-particle entanglement on the dipole forbidden transitions of strontium.

4.1 Linear optical resonators

The two-mirror, standing wave cavity is a Fabry-Perot interferometer with the spherical mirrors M_1 and M_2 with radii of curvatures (ROC) R_1 and R_2 (see figure 4.1.1a). A resonator is considered as stable if an electromagnetic field reproduces itself after one round trip inside the resonator. This leads to constructive interferences and a build-up of the field intensity. With the aid of the ray matrix representation (ABCD matrix) of the paraxial optics, a *stability criterion* for Fabry-Perot resonators can be derived [167]:

$$0 < \left(1 - \frac{L}{R_1}\right)\left(1 - \frac{L}{R_2}\right) < 1\,, \tag{4.1.1}$$

where L is the resonator length. This criterion is depicted in the stability diagram in figure 4.1.1b.

Besides the geometrical stability criterion, the *resonance condition*

$$kL = q\pi, \quad q \in \mathbb{N} \tag{4.1.2}$$

with the wave vector $k = 2\pi/L$, ensures that the phase of the electric field is the same after one round trip. From equation 4.1.2 the resonance frequencies for a given length L are given by

$$\nu_q = q\frac{c}{p}\,, \tag{4.1.3}$$

with the frequency distance between two axial modes $\nu_{q+1} - \nu_q$, called the *free spectral range* (FSR):

$$\nu_{FSR} = \frac{c}{p}. \tag{4.1.4}$$

p denotes the round-trip-length of a photon inside the cavity. In the case of a

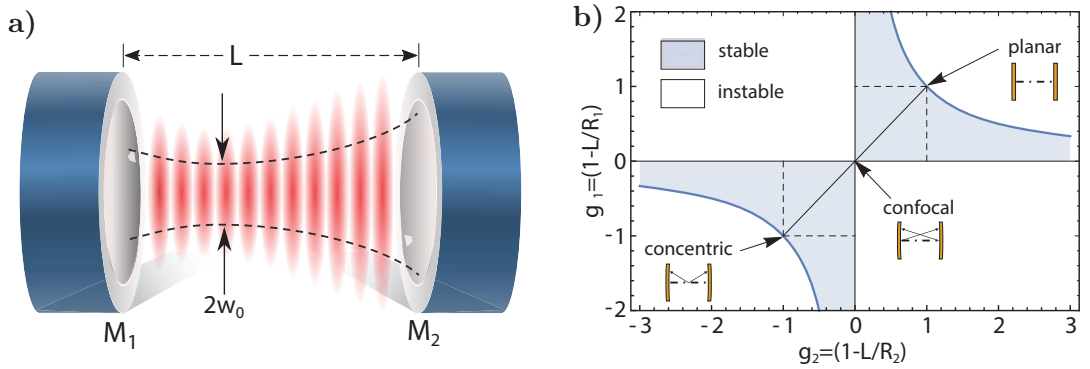

Figure 4.1.1: a) Schematic representation of a Fabry-Perot cavity. b) Stability diagram of optical resonators.

linear cavity, the round trip length is twice the cavity length ($p = 2L$) but only the single cavity length for ring cavity ($p = L$).

In order to evaluate the behavior of a cavity on resonance, all components of a incident beam need to be taken into account. Each mirror interface can be described by its intensity reflection $\mathcal{R}$, transmission $\mathcal{T}$ and losses $\mathcal{L}$, while the conservation rule $1 = \mathcal{R} + \mathcal{T} + \mathcal{L}$ holds. An important characteristic of a cavity is the number of round trips of a photon inside the cavity, called the *finesse*, which depends on the mirror losses and transmission and therefore reads

$$\mathcal{F} \simeq \frac{2\pi}{\sum_i (\mathcal{T}_i + \mathcal{L}_i)} \,. \tag{4.1.5}$$

Another representation of the finesse is

$$\mathcal{F} = \frac{\nu_{FSR}}{\delta\nu} \tag{4.1.6}$$

with the resonator's transmission linewidth $\delta\nu$ (FWHM). By calculating the interfering field inside cavity, the on-resonance reflectivity R_c can be calculated as the ratio of the reflected and the incident laser intensity and reads [172]

$$R_c = \left(\mathcal{L}_1 + \sum_{i>1} (\mathcal{T}_i + \mathcal{L}_i) - \frac{\mathcal{T}_1}{\sum_i (\mathcal{T}_i + \mathcal{L}_i)} \right)^2 , \tag{4.1.7}$$

leading to the cavity coupling efficiency

$$C = \frac{P_{\text{ref}}}{P_{\text{in}}} = 1 - R_c \,. \tag{4.1.8}$$

For the sake of completeness, the ratio of the transmitted and the incident laser intensity is given by

$$T_c = \left(\frac{\sum_i \mathcal{T}_i}{\sum_i (\mathcal{T}_i + \mathcal{L}_i)} \right)^2 . \tag{4.1.9}$$

Another important property of the cavity is the enhancement factor E_c, which denotes the ratio between the circulating and incident beam intensity. For perfect mode-matching and a resonant coupling, the enhancement factor calculates as [172]

$$E_c = 4 \frac{\mathcal{T}_1 (1 - n\mathcal{L} - \sum_{i>1} \mathcal{T}_i)}{\left[\sum_i (\mathcal{T}_i + \mathcal{L}_i) \right]^2} \,. \tag{4.1.10}$$

If the transmission coefficient $\mathcal{T}_1$ of the incoupling mirror is equal to the cavity losses $\mathcal{L}_{\text{tot}} = \sum_i (\mathcal{T}_i + \mathcal{L}_i)$, the enhancement factor reaches its maximum and the cavity is called impedance matched. Hence, a compromise between a high finesse and the impedance matching needs to found when designing a cavity.

The geometrical properties of the resonator, L, R_1, R_2, define the resonator's mode field $\psi(\boldsymbol{r})$ characterized by the mode waist radius[1] and the Rayleigh length z_R. The discussion can be found in Appendix A. Knowing the length L of a resonator and its mode waist w_0, the resonator's mode volume can be calculated by

$$V = \int |\psi(\boldsymbol{r})| \, \mathrm{d}V \simeq \frac{\pi w_0^2}{8} \cdot p \,. \tag{4.1.11}$$

For a linear two-mirror cavity, the mode volume approximates to $V_{\text{lin}} \simeq \pi/4 w_0^2 \cdot L$ and to $V_{\text{lin}} \simeq \pi/2 w_0^2 \cdot L$ for a ring cavity, respectively.

4.2 The traveling wave (ring) resonator

The following discussion considers only the case of a triangular configuration shown in figure 4.2.1a. This cavity consists of three mirrors – one curved (M_3) and two flat (M_1, M_2). The angle α denotes the angle between the incident and reflected ray.

[1] The $1/e$ field radius or $1/e^2$ intensity radius at the waist position.

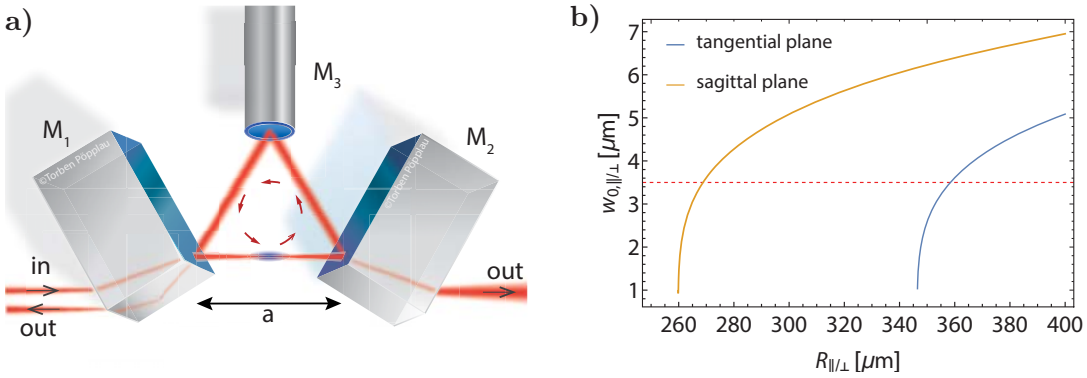

Figure 4.2.1: a) shows the schematic representation of a ring cavity with equilateral triangle optical path. M_1 is the incoupling mirror. b) Cavity mode waist for a equilateral ring cavity with a branch length $a = 200\,\mu$m. The red dashed line indicates the design cavity waist of 3.5 µm.

4.2.1 Compensation of astigmatism

In many cases, the beam parameters of a ring cavity can be calculated equivalently to a linear cavity by unfolding the ring cavity around a symmetry point[2] [173]. However, a major difference occurs due is its non-normal angle of incidence on the curved mirror M_3. Considering a spherical off-axis mirror with a ROC of R, the beam effectively sees two different ROCs in the sagittal and tangential plane which leads to an elliptically shaped cavity mode waist. For an angle of incidence of $\alpha/2$, the effective radius of curvature is $R_\parallel = \mathrm{R} \cdot \cos(\alpha/2)$ along the tangential plane and $R_\perp = \mathrm{R}/\cos(\alpha/2)$ in the sagittal plane [174].

The optical system can be then described with the aid of ray matrices. The round trip ABCD matrix in the sagittal plane of a ring cavity as depicted in figure 4.2.1a is[3]:

$$M_{sag} = \begin{pmatrix} A_s & B_s \\ C_s & D_s \end{pmatrix} = \begin{pmatrix} 1 & a/2 \\ 0 & 1 \end{pmatrix} \begin{pmatrix} 1 & 0 \\ 0 & 1 \end{pmatrix} \begin{pmatrix} 1 & a \\ 0 & 1 \end{pmatrix} \cdot \begin{pmatrix} 1 & 0 \\ -\frac{2\cos\alpha/2}{\mathrm{R}} & 1 \end{pmatrix} \begin{pmatrix} 1 & a \\ 0 & 1 \end{pmatrix} \begin{pmatrix} 1 & 0 \\ 0 & 1 \end{pmatrix} \begin{pmatrix} 1 & a/2 \\ 0 & 1 \end{pmatrix} \tag{4.2.1}$$

[2] For example, the cavity waist position of the triangular ring cavity presented in the following.
[3] Starting point is the cavity waist between M_1 and M_2.

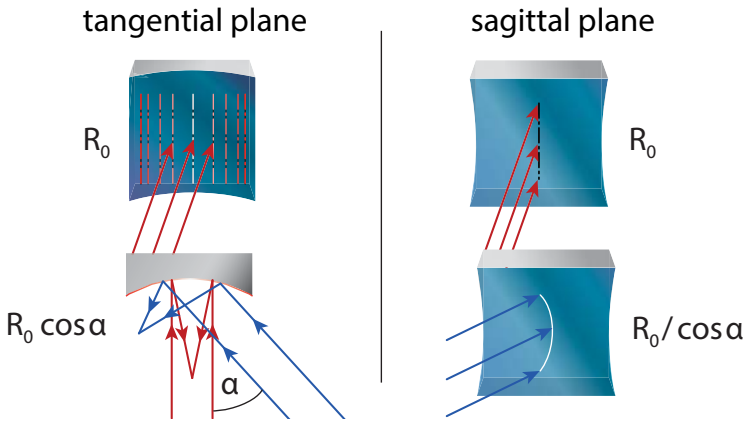

Figure 4.2.2: Illustration of the astigmatism caused by an off-axis mirror with the ROC R_0, decomposed into tangential and sagittal components represented by cylindrical mirrors. *Left:* The vertical lines represent the contour lines of the mirror's height profile seen by the tangential component of the incident beam. The contour lines of the same height profile are denser in the case of a smaller incident angle α, leading to a smaller ROC. *Right:* Shown is the mirror seen by the sagittal component of the incident beam. The effective area and thus the ROC seen by the beam increases under non-normal incidence.

and in the tangential plane

$$M_{tang} = \begin{pmatrix} A_t & B_t \\ C_t & D_t \end{pmatrix} = \begin{pmatrix} 1 & a/2 \\ 0 & 1 \end{pmatrix} \begin{pmatrix} 1 & 0 \\ 0 & 1 \end{pmatrix} \begin{pmatrix} 1 & a \\ 0 & 1 \end{pmatrix} \cdot \begin{pmatrix} 1 & 0 \\ -\frac{2}{R\cos\alpha/2} & 1 \end{pmatrix} \begin{pmatrix} 1 & a \\ 0 & 1 \end{pmatrix} \begin{pmatrix} 1 & 0 \\ 0 & 1 \end{pmatrix} \begin{pmatrix} 1 & a/2 \\ 0 & 1 \end{pmatrix} . \tag{4.2.2}$$

Based on these matrix elements, the waist and required ROCs of the ring cavity presented in following were derived from the complex Gaußian beam q-parameter. A more detailed explanation can be found in Appendix A.

Besides using a bow-tie ring resonator geometry, the cavity waist ellipticity is usually countered by decreasing the angle of incidence on the curved mirror, which eventually leads to a longer cavity. As this is not desirable in a CQED system where a small mode volume is required, another approach was chosen in order to circumvent the mode waist ellipticity.

The CO_2 fabrication setup described in the previous chapter allows to produce elliptically shaped mirrors with two different ROCs. For a ring cavity spanning a equilateral triangle (i. e. $\alpha = 60°$), the ratio between the two ROCs so that $R_\parallel = R_\perp$ is 0.75. A 600 µm long cavity with a cavity waist of 3.5 µm requires M_3

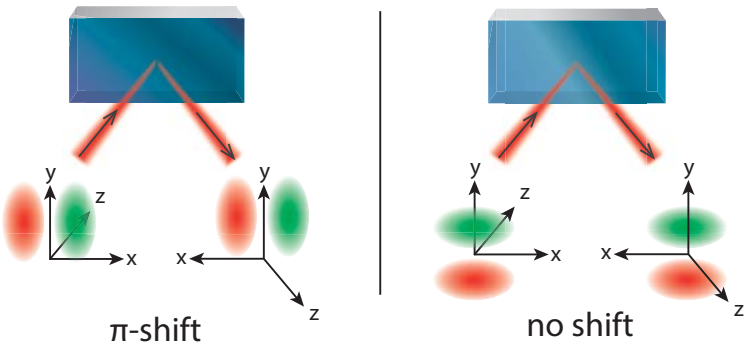

Figure 4.2.3: Illustration of the odd-parity phase shift of π.

to have the ROCs $R_{\mathrm{sag}} \approx 270\,\mu\mathrm{m}$ and $R_{\mathrm{tan}} \approx 360\,\mu\mathrm{m}$, as shown in figure 4.2.1b.

4.2.2 Frequency spectrum

Under the paraxial approximation, the frequency spectrum of the transversal modes of a resonator consists of several contributions and is described by [175]:

$$2\pi \cdot \frac{\nu^{\mathrm{q}}_{\mathrm{m,n}}}{\nu_{FSR}} = q + \zeta_{\mathrm{m,n}} + \phi_{\mathrm{op}} + \phi_{\mathrm{pola}}\,. \tag{4.2.3}$$

Here (q, m, n) are the longitudinal modes. The different contributions are discussed in the following.

Gouy phase $\zeta_{\mathrm{m,n}}$: Each transverse mode picks up a slightly different phase during one round trip inside the cavity. This phase is called Gouy phase and reads [167]

$$\zeta_{\mathrm{m,n}} = \left(m + \frac{1}{2}\right) \cdot \arccos\left(1 - \frac{L}{R_{\parallel}}\right) + \left(n + \frac{1}{2}\right) \cdot \arccos\left(1 - \frac{L}{R_{\perp}}\right)\,. \tag{4.2.4}$$

This description holds under the assumption that the cavity field can be described as a product of independent field distributions in two transverse directions, i. e. a simple astigmatic system. For cavities with more than three mirrors, coupling of the two transverse directions can occur if the resonator is non-planar [176–178], leading to a slight rotation of the polarization during each round-trip. As a consequence, close attention needs to be payed to the alignment of the plane mirrors in section 4.4.

The odd-parity phase shift ϕ_{op}: For an odd number of resonator mirrors, an additional phase shift occurs. Odd parity TEM spatial modes inside a cavity are phase shifted by half a FSR ([173] and references therein):

$$\phi_{\mathrm{op}} = \frac{\pi}{2}(1-(-1)^n) = \begin{cases} 0, & n \text{ even} \\ \pi, & n \text{ odd} \end{cases} \tag{4.2.5}$$

When, for example, the TEM_{10} experiences a reflection as shown in figure 4.2.3, the lobes change the side with respect to the x-y-propagation-plane, i. e. they accumulate a π-shift. The equivalent TEM_{01} mode, however, is not affected.

The polarization-dependent phase shift ϕ_{pola}: A ring cavity has also a polarization dependent resonance condition [175]. If a beam hits a mirror at non-normal angle, it collects a different phase depending on its polarization as the penetration depths into the dielectric layers differ. In a planar ring resonator, a circulating field with p-polarization collects a phase change of $\phi_p = 0$ whereas in s-polarization, the ideal phase change is $\phi_s = n\pi$ (n – number of mirrors), which leads to two different resonance conditions. Hence, when the triangular ring cavity is locked at resonance for s-polarization, it is anti-resonant for the p-polarized light. Due to this staggered resonance, the triangular ring cavity is also often referred to as *mode cleaner*.

4.3 Requirements on the mirror quality

As previously introduced, the finesse that characterizes the quality of the resonator is directly related to the total losses by reflection on a mirror $\mathcal{L}$ and the transmission $\mathcal{T}$ of the mirror (see equation 4.1.5). The total losses can be divided into three loss mechanisms:

$$\mathcal{L}_{\mathrm{tot}} = \mathcal{L}_{\mathrm{A}} + \mathcal{L}_{\mathrm{C}} + \mathcal{L}_{\mathrm{S}}\,. \tag{4.3.1}$$

In the following section, these different loss mechanisms will be discussed and applied to exemplary parameters for the envisioned high-finesse ring cavity.

Absorption loss $\mathcal{L}_{\mathrm{A}}$: Common mirror coatings for high-finesse cavities are made of highly-reflective Bragg layers of different dielectric materials. They are constructed by an alternation of thin films of high and low refractive index materials, e. g. Ta_2O_5 and SiO_2. Even though they are made to show low loss in the visible and the near-infrared spectrum, impurities of the raw material lead to additional absorption losses. Nevertheless, losses down to 1 ppm can be achieved by this technique [179].

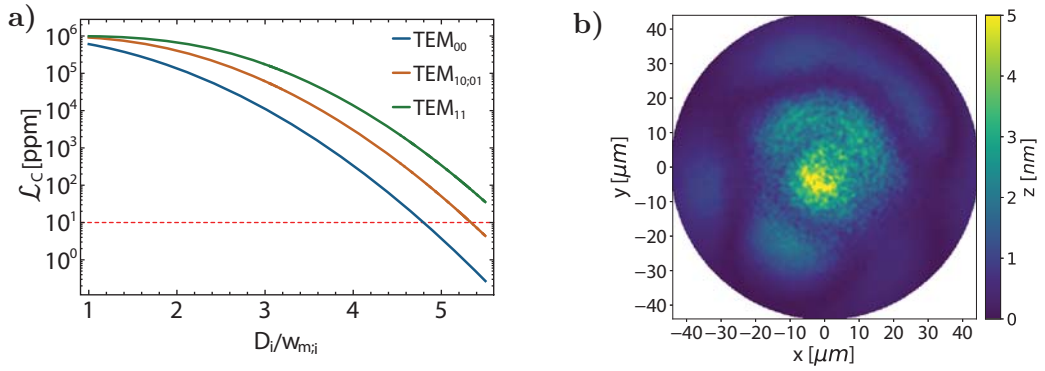

Figure 4.3.1: a) clipping losses. b) Local mirror map of the structure presented in subsection 3.4.2. The height residual is averaged over five pixel, corresponding to 1 µm in order to reduce the profilometry noise.

Due to a double-resonant mirror coating (see subsection 4.4.2), the estimated losses by absorption are elevated as the layer stack is less efficient than a single Bragg reflector. For the wavelengths of interest, these losses amount to approximately $\mathcal{L}_\mathrm{A} = 10\,\mathrm{ppm}$, estimated by the coating company[4].

Clipping loss $\mathcal{L}_\mathrm{C}$: When the mirror size is not several orders of magnitude larger than the size of the Gaußian cavity mode, another problem arises as the wings of the cavity mode are not reflected back into the mode. One can define a mirror cutoff radius r_{clip}, beyond which most of the energy of a mode of intensity $I(r)$ is lost. By integrating the intensity over the mirror surface, the clipping losses read as:

$$\mathcal{L}_C = 1 - \frac{\int_0^{r_{clip}} rI(r)^2\,\mathrm{d}r}{\int_0^{\infty} rI(r)^2\,\mathrm{d}r}\,. \tag{4.3.2}$$

For the Gaußian fundamental resonator mode with the mode radii $w_{m;i}$ on the resonator mirror and a mirror diameter D_i, equation 4.3.2 simplifies to:

$$\mathcal{L}_C(D_i, w_{m;i}) = \exp\left[-2\left(\frac{2}{D_i}\right)^2 w_{m;i}^2\right]\,. \tag{4.3.3}$$

From figure 4.3.1a it can be seen, that the mirror diameter should be around five times lager than the mode field radius on the mirror in order to achieve the same level of losses than $\mathcal{L}_A$

[4]LASEROPTIK GmbH, Garbsen, Germany

Scatter loss $\mathcal{L}_S$: Even though a mirror appears to be nearly perfect on a macroscopic scale, light scattering due to micro-roughness is still a present issue. These micro-roughness are small irregularities of the mirror surface from a perfect spherical form and can be described by the 2D mirror map, as shown in figure 4.3.1b. A mirror map can be associated to a RMS surface roughness, defined as

$$\sigma_{\mathrm{RMS}} = \sqrt{\frac{1}{n}\sum_{i=1}^{n}(z_i - \tilde{z})^2}\,, \tag{4.3.4}$$

where $\tilde{z}$ is the mean profile height and z the local profile height.

Considering a nearly smooth surface, i. e. $\sigma_{\mathrm{RMS}} \ll \lambda$, a simple model that relates the micro-roughness to scattering losses had been developed in the 1950s [180, 181]. It assumes that the solid radiation characteristics is similar to a single scatterer, which, in case of linearly polarized light, can be treated as a Hertzian dipole. The model links the RMS surface roughness to the scattering loss for non-normal incidence at angle θ_i, which is also often referred to '*Total Integrated Scatter*' (TIS) [182]:

$$\mathcal{L}_S \approx \left(\frac{4\pi\sigma}{\lambda}\cdot\cos\theta_i\right)^2. \tag{4.3.5}$$

However, this approximation does neither take into account the frequency spectrum of the surface roughness nor the Gaußian mode profile of the incident beam. Hence, it gives only a rough idea of the surface scattering loss to be expected.

Another useful tool determining the scatter losses is the 1D power spectral density (PSD) of a mirror map. It relates to the surface roughness σ as the integration over its spatial frequency range [183]:

$$\sigma^2 = \int_{f_{\mathrm{lim}}}^{\infty} \mathrm{PSD}(f)\,\mathrm{d}f\,. \tag{4.3.6}$$

The scattering angle θ_n of light of wavelength λ at normal incidence can be written as a function of the frequency f of spatial defects. The relation obeys the classical Bragg diffraction law, yielding

$$\sin\theta_n = n\cdot\lambda f\,, \tag{4.3.7}$$

where n is the diffraction order. For the sake of simplicity, only first order scattering will be considered in the following, i. e. $n = 1$. Furthermore, this description only holds if the amplitude of the surface defect is much smaller then the wavelength. From a geometrical view, the maximum diffraction angle until which

scattered light from mirror center stays in the cavity can be calculated to

$$\theta_{\text{lim}} = \arctan(\frac{D}{2L}) \approx \frac{D}{2L}\,, \tag{4.3.8}$$

where D denotes the mirror diameter and L the cavity length. Combining equation 4.3.7 and equation 4.3.8, the spatial frequency corresponding to the maximum diffraction angle θ_{max} reads

$$f_{\text{lim}} = \frac{D}{2L \cdot \lambda}\,. \tag{4.3.9}$$

In concrete terms this means that a surface imperfection at spatial frequency $f > f_{\text{lim}}$ will scatter a fraction of light at angles θ or larger. The amount of light reflected back at normal incidence will be thus reduced and this amount calculates in accordance to equation 4.3.5 as $(4\pi \cdot \sigma(f)/\lambda)^2$ where $\sigma(f)$ is the amplitude of the corresponding defect. For the cavity presented in this chapter, the maximum spatial frequency is on the order of $0.22\,\mu\text{m}^{-1}$ (or spatial periods below $4.6\,\mu\text{m}$).

In 1983, Elson *et al.* [184] figured out any spatial frequency higher than the inverse of the wavelength of the incident radiation does not contribute to the TIS. They defined this upper frequency limit by means of the *autocovariance* (ACV) length l, which is defined as the half-width of the ACV function. The ACV is basically Fourier transformation of the surface PSD function. Given a Gaußian PSD, the ACV and the PSD relates as follows (the reader is refered to [182] for more details):

$$\text{ACV}(r) = \sigma_{\text{tot}}^2 \cdot \exp\left(-\frac{\sigma_{\text{tot}}^2}{l^2}\right) \tag{4.3.10a}$$

$$\text{PSD}(f) = \pi l^2 \sigma_{\text{tot}}^2 \cdot \exp\left(-(\pi l f)^2\right)\,. \tag{4.3.10b}$$

Taking into account this uper frequency limit, the TIS can be rewritten as a modified version of equation 4.3.5 at normal incidence [182, 184]:

$$\mathcal{L}_S \approx \left(\frac{64}{3}\right) \cdot \left(\frac{\pi^4 \sigma^2 l^2}{\lambda^4}\right)\,. \tag{4.3.11}$$

Lower spatial frequency are rather considered as *waviness* and lead to a redistribution of the optical fundamental TEM_{00} to higher-order modes. In [183] the authors introduced the '*local mirror map*' which is the absolute surface residual weighted by the beam intensity profile. The local mirror map for the fiber strucutre presented in subsection 3.4.2 is shown in figure 4.3.1b. The authors further state that a local mirror map below $\approx 1\,\text{nm}$ resulted in losses less than $1\,\text{ppm}$. Even though this requirement is not fullfilled here, it is still comparable to the previous

fiber-based cavities [136]. However, the question if this hypothesis holds for the ring cavity presented in the following section, could be investigated by means of an optical FFT simulation [185].

Eventually, the dielectric coating deposits uniformly on the substrates and follows its surface shape and hence also the micro-roughness and waviness. This implies that the substrate's surface quality has to meet the cavity requirements *a priori* as no improvement of the surface by means of low-pass filtering of the spatial frequency via the coating can be expected. In [144] the surface roughness of a CO_2-machined fiber surface was measured to be $\sigma = 0.22\,\text{nm}$ (RMS)[5], which is in accordance with the CO_2 polished plane substrates in section 3.3. By fitting the surface PSD presented in section 3.3, the ACV length amounts to 123 nm, leading to an estimated scatter loss bsaed on equation 4.3.11 of $\mathcal{L}_S = 7\,\text{ppm}$ at 689 nm and $\mathcal{L}_S = 2\,\text{ppm}$ at 913 nm.

Spherical aberrations: When a beam hits a spherical mirror with a ROC of R, it collects a phase change of $\sim 2kz(x,y)$ due to the reflection, where $k = 2\pi/\lambda$ and z denotes the mirror surface equation $z(x,y) = R - \sqrt{R^2 - (x^2+y^2)}$. Using the second order approximation, $z(x,y)$ reads [186]

$$z(x,y) = \frac{x^2+y^2}{2R}\left(1 + \frac{x^2+y^2}{4R^2}\right). \tag{4.3.12}$$

The first fraction represents the usual paraboloidal approximation for the phase change while the second part is the correction due to the actual spherical shape of the mirror. It can be seen that this turns out to be negligible if the beam size $2w$ is much smaller than the mirror's ROC R ($(2w)^2 \ll R^2$). In the case of the cavity presented in section 4.4, $(2w)^2/R_{\text{eff}}^2 \simeq 0.009$ and spherical aberrations can be thus neglected.

4.3.1 Back-propagating scattered mode

Even though a ring cavity excels by its traveling-wave characteristics, a spurious standing wave can still build up in a high-finesse cavity. It arises from light that is coherently scattered by surface defects or emitters inside the cavity, such as atoms. This effect can be suppressed by counter-injecting a beam into the cavity, that is of opposite phase than the counter-propagating wave [187]. Nevertheless, it is important to evaluate its order of magnitude.

[5] The fiber surface roughness σ measured with an atomic force microscope relates to single-shoot structure. For the previously developed multi-shoot technique, an AFM analysis is still pending.

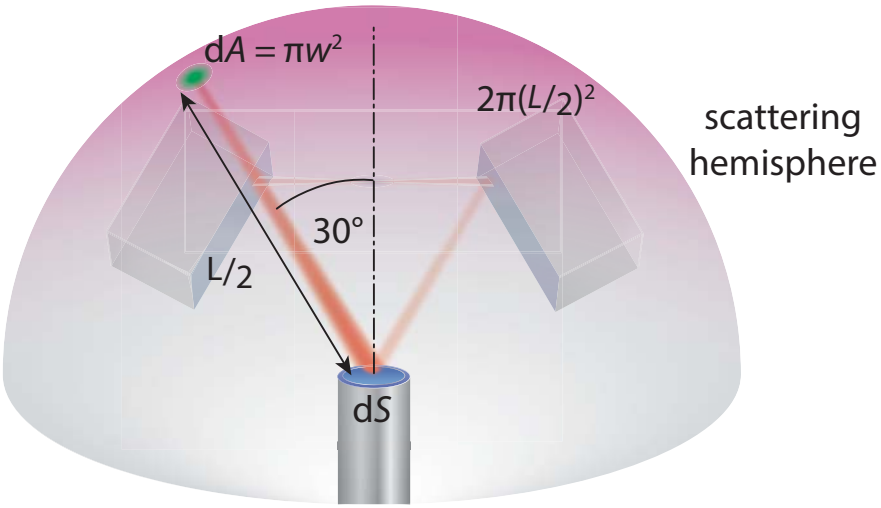

Figure 4.3.2: Illustration of the light scattering of the fiber mirror into the back-propagating mode. The scattering hemisphere has s radius of half the cavity length L and spans by unfolding the cavity around the left plane mirror. dA represents the mode waist cross-section on the scattering hemisphere and the color gradient illustrates the cosine scattering distribution.

Assuming that photon scattering on the surface can be treated as a Hertzian dipole, the power of the counter-propagating mode can be estimate by considering the cavity's geometry. A photon, that is scattered at the mirror center needs to stay within the solid angle that is spanned by the cavity. Following Lambert's cosine law[6], the fraction of the scattered light entering the back-propagating fundamental mode can be defined as

$$\Omega(\theta_i) = \frac{\cos(\theta_i) \cdot \mathrm{d}A}{2\pi r^2}\,, \tag{4.3.13}$$

where θ_i is the 30° angle of incidence of the ring cavity, $\mathrm{d}A = \pi w_0^2$ the illuminated cavity waist cross-section and $r = {}^{L}/_{2}$ the half the cavity length.

Following the argumentation in [175, 188], the intensity enhancement factor E_{back} of the back-propagating wave can be defined similar to equation 4.1.10 as

$$E_{\mathrm{c,back}} = \frac{4\mathcal{T}_{\mathrm{back}}}{(\mathcal{L}_{\mathrm{tot}} + \mathcal{T}_{\mathrm{tot}})^2}\,. \tag{4.3.14}$$

Here, $\mathcal{T}_{\mathrm{back}}$ defines the transmission coefficient of an fictive input mirror for the counter-propagating cavity. However, the counter-propagating cavity is not build up by an external incident beam, but by the back-scattered light inside the cavity.

[6] Sometimes also referred to the *photometric law of distance*

Under the assumption that all photons from the surface scattering $\mathcal{L}_S$ inside the solid angle spanned by the cavity waist contribute to the buildup of a standing wave, the transmission coefficient can be approximated to

$$\mathcal{T}_{\text{back}} = 3 \times \mathcal{L}_S \Omega \,. \tag{4.3.15}$$

For the ring cavity presented in the following section, Ω calculates to 5.9×10^{-5} sr. Given the total transmission $\mathcal{T}_{\text{tot}} \approx 70$ ppm at 689 nm and losses $\mathcal{L}_{\text{tot}} \approx 61$ ppm, the intensity enhancement factor calculates to $E_{\text{c,back}} = \frac{I_{\text{back}}}{I_{\text{cavity}}} = 0.29$.

This is only a first-order approximation and can be seen only as an upper bound as the model considers only uniform diffuse scattering and neither directional diffuse nor specular scattering. Additonnaly, the buildup of a standing backpropagating wave requires coherent scattering on all three mirrors. It is there to be expected that power of the backpropagating mode shows non-neglible power fluctuations. Nonetheless, this problem can be tackled by counter-injecting a beam of opposite phase into the cavity [187].

4.4 Conception of the upcoming high-finesse ring cavity

4.4.1 Design

As explained in subsection 1.1.2, the single-atom-cooperativity C_0 scales with $C_0 \propto 1/w_0$ and it is therefore of special interest to reduce the size of the cavity in order to get a smaller cavity waist. Therefore, a new, compact ring cavity design has been developed. It takes advantage of the CO_2 machining method introduced in chapter 3, extending it to the situation of a ring cavity. The concept is presented in figure 4.2.1a. It consists of two plane mirrors $M_{1,2}$, made of CO_2-polished plane substrates, and a fiber which contains a spherical mirror M_3. The nominal length of the resonator is $L \simeq 600\,\mu$m.

The plane mirrors of dimension $2.5 \times 2 \times 1$ mm (H × W × D) are made from a fused silica wafer (see section 3.3) and the concave mirror is fabricated on a fiber tip[7]. The fiber does only serve as a perfect mirror and has no other purpose, i. e. no light is coupled into the fiber. The reasons for choosing a fiber were of geometrical nature: in a equilateral, triangular cavity of length $L = 3a = 600\,\mu$m, the remaining gap between the two plane mirrors at the position of the third mirror M_3 is $\sim 400\,\mu$m. Therefore, a typical multi-mode fiber with a diameter of 210 µm is appropriate and leaves still enough clearance for the alignment. Furthermore,

[7] IVG Cu200/220

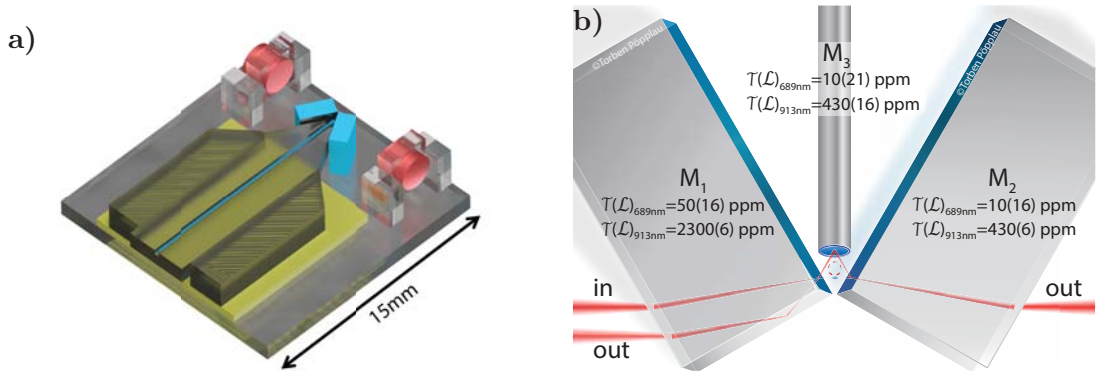

Figure 4.4.1: a) CAD draft of the high-finesse cavity assembly. The plane mirrors and the fiber are colored in cyan. Also shown are the piezo (yellow) and the mode-matching aspheric lenses (red). b) True to scale illustration of the ring cavity with the corresponding losses and transmissions of each mirror.

a fiber carries a long handle which simplifies its manipulation compared to micro-optics of the same lateral dimensions.

The effective ROC on the fiber (M_3) was chosen to be 310 µm. This yields to a near-concentric cavity ($L \lesssim 2R_3$) with a small cavity waist. By the purpose of astigmatic compensation, the radii of curvature in the tangential plane is $\mathrm{ROC}_{\parallel} \simeq 360\,\mu m$ and in the sagittal plane $\mathrm{ROC}_{\perp} \simeq 270\,\mu m$. The near-concentric cavity supports thus a fundamental mode with a circular cavity waist of 3.5 μm, leading to a mode volume of $\approx 3.7 \times 10^3 \lambda^3$.

The incoupling beam hits, after being reflected on the mirror coating, the side of the plane substrate. There, it experience a total reflection and runs parallel to the incident beam. After a collimation lens, the reflected beam has a diameter of approximately 600 µm. The spacing between both beams is 450 µm which is sufficient to separate them by a thin mirror. Another option would have been to use penta-prisms as plane mirrors so that the input and the reflected beam have separate facets on the prism. This idea was not further pursued as no company had been found to fabricate custom micro penta-prisms made of fused silica with an excellent surface quality.

The plane mirrors are glued[8] onto a 15 mm × 15 mm big fused silica plate, as it can be seen in figure 4.4.1a, which will be eventually glued into the vacuum glass cell. Furthermore, the CO_2-machined fiber is glued into the V-groove of a 1.2 cm long fused silica support[9]. The tip of this support has a V-shape with an angle of

[8] OPTOCAST, 3410 Gen2, EMIUV
[9] Precinet SARL

60° and thus matches the angle between the plane mirrors. Also is the bottom of the tip is chamfered in order to increase the optical access inside the cavity.

In order to retain all rotational degrees of freedom, the V-groove is not directly glued onto a piezoelectric shear plate[10], but first glued between two fused silica blocks which are then attached to the shear piezo. Besides the mirrors, two aspheric lenses[11] are glued right before(after) the cavity input(output). Their purpose is to maintain a stable mode matching.

4.4.2 Coating

The fiber and the plane mirrors are coated with an ion-beam sputtered (IBS), dual-wavelength high-reflectivity coating[12] for 689 nm to 698 nm and 813 nm to 913 nm. These coatings are optimized to an angle of incident of 30°. The nominal transmission $\mathcal{T}$ of the incoupling mirror M_1 at 689 nm(913 nm) is 50 ppm(2300 ppm), whereas M_2,M_2 have a transmission of 10 ppm(430 ppm) (see figure 4.4.1b). This choice is a compromise to increase the cavity incoupling while maintaining a high finesse.

The cavity losses by the coating absorption are estimated to approximately 10 ppm, 7 ppm(2 ppm) by surface scattering and additionally 10 ppm for the fiber mirror due to clipping losses. Overall, the estimation of the finesse leads to $\mathcal{F}_{689\,\mathrm{nm}} \approx 51\,000$ and $\mathcal{F}_{913\,\mathrm{nm}} \approx 2\,000$

An open question remains the need of a SiO_2 protection layer. As reported in [189], an additional SiO_2 film can reduce the long term degradation of the cavity finesse that arise from oxygen depletion of the coating. However, in [190] the authors also report a finesse degradation even though a protective SiO_2 layer was present. Therefore, this layer will not be added here as it introduces additional losses that potentially lower the nominal cavity finesse. Furthermore, in Appendix B no effect of the 461 nm blue MOT light could be seen on a fiber cavity finesse.

Eventually, the backsides of the plane mirrors feature an anti-reflective coating.

4.5 Estimating the *dc*-Stark shift induced by the piezo electric field

The shear plate actuator consists of two electrodes enclosing a piezo ceramic. By applying a electric tension to the electrodes, the piezo ceramic contracts and allows thus to scan the cavity length precisely on a nanometer scale. Even though the

[10] Noliac CSAP02
[11] Edmund optics, 48-145, $f = 5\,\mathrm{mm}$
[12] LASEROPTIK GmbH

quantity	expression	ring cavity
round trip length	L	600 µm
radius of curvature	$R_{\parallel}/R_{\perp}$	360 µm/270 µm
effective radius of curvature	R_{eff}	310 µm
cavity waist	w_0	3.5 µm
mode volume at 689 nm	V	$3.7 \times 10^3 \lambda^3$
FSR	$\Delta\nu_{\text{FSR}} = \frac{c}{L}$	500 GHz
finesse at 689 nm	$\mathcal{F}_{689\text{nm}}$	48 000
finesse at 913 nm	$\mathcal{F}_{913\text{nm}}$	2 000
cavity linewidth (FWHM) at 689 nm	$\Gamma_{689\text{nm}} = \frac{\Delta\nu_{\text{FSR}}}{\mathcal{F}_{689\text{nm}}}$	11 MHz
coupling	$g_0/2\pi$	1.3 MHz
cavity decay rate	$\kappa/2\pi$	10 MHz
single atom cooperativity	C_0	~ 90

Table 4.1: Summary of the intended parameters of the ring cavity.

piezo is an essential and excellent tool to operate the ring cavity, its electric field also affects the atomic transition (*dc* Stark shift). Working with the narrow clock transition of strontium requires therefore to minimize these effects during locking or a measurement sequence. Therefore, a finite element simulation[13] has been performed in order to estimate the residual frequency shift induced by the shear piezo.

4.5.1 Calculation of the electric potential

The electric potential in a charge free space, i. e. outside the piezoelectric actuator, can be calculated via the Laplace equation. The scalar potential $\Phi(x, y)$ in two dimensions holds the following equations:

$$\Delta\Phi = \nabla\mathbf{E} = 0, \tag{4.5.1a}$$

$$\frac{\partial^2\Phi}{\partial x^2} + \frac{\partial^2\Phi}{\partial y^2} = 0. \tag{4.5.1b}$$

The two electrodes of the piezo were considered by the *Dirichlet*'s boundary

[13] Wolfram Mathematica 10.2

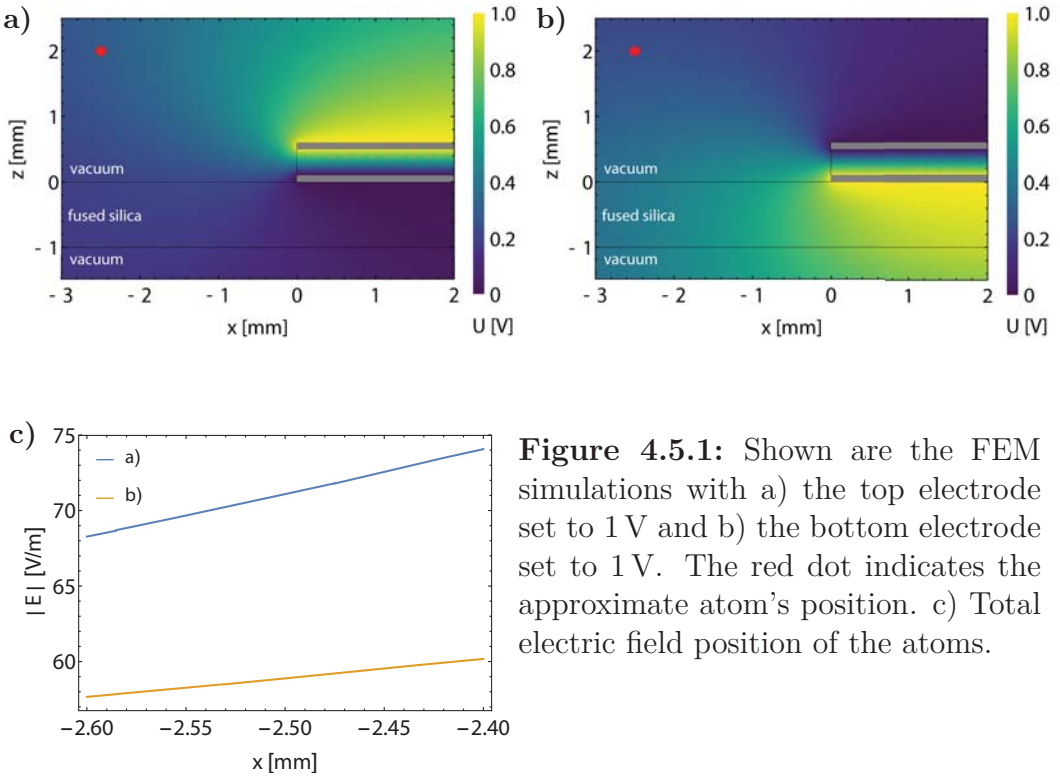

Figure 4.5.1: Shown are the FEM simulations with a) the top electrode set to 1 V and b) the bottom electrode set to 1 V. The red dot indicates the approximate atom's position. c) Total electric field position of the atoms.

condition and the piezoceramic and the fused silica base plate by the *Neumann*'s boundary condition. A relative permittivity of 1900 for the piecoceramic and 3.8 for the fused silica were assumed.

As finite element simulations require a window with an outer edge Γ, the piezo electrodes in the simulation are enclosed in a finite box. This artificially introduced finite window should be at least five times bigger the characteristic extent of the object of interest, i. e. the electrodes. The further the edges are away from the region of interest, the smaller is its effect on the solution. To reduce the required computational power, the windows Γ had a height and width of 30 mm each.

The electric field then relates to the electric potential by a gradient relationship as

$$\mathbf{E} = \nabla\Phi\,. \tag{4.5.2}$$

The simulation results are shown in figure 4.5.1. It can be clearly seen that the configuration where the anode is pointing downwards leads to a smaller electric field. At the position of the atoms, the total electric field amounts to $59\,\mathrm{V\,m^{-1}}$.

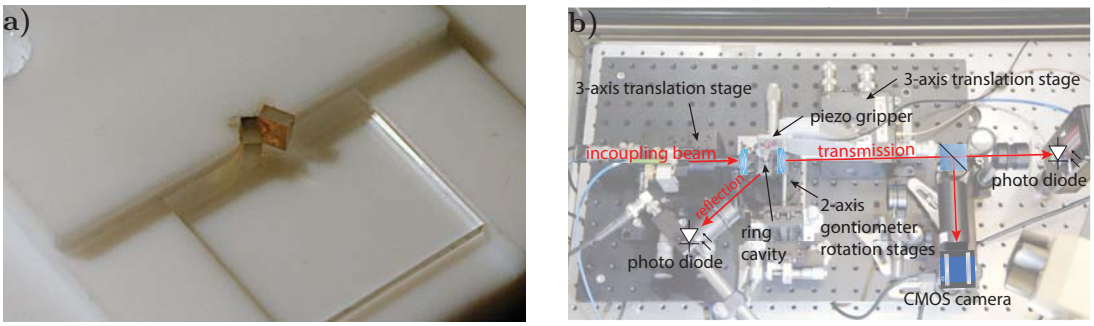

Figure 4.6.1: a) Gluing guide made from Teflon in order to precisely glue the plane mirrors under an angle of 60°. b) The Alignment setup used to acquire the results presented in this section.

4.5.2 The *dc*-Stark shift of Strontium

Given a uniform static electric field $\mathbf{E}$, the clock transition acquires a frequency shift $\delta\nu_{dc} = kE^2$, where $E = |\mathbf{E}|$ and k is specific to the clock transition.

The piezoelectric shear plate[14] has a nominal stroke of ∼2.4 nm/V, resulting in 190 V for scanning a FSR at a lattice wavelength of 914 nm. Assuming roughly 20 V for compensating for long term drifts during a day and the measured static differential prolarizability of $\Delta\alpha_{\mathrm{dc}} = 4.078 \times 10^{-39}\,\mathrm{Cm}^2/\mathrm{V}$ [191], the residual frequency shift calculates to

$$\delta\nu_{\mathrm{dc,drift}} = -\frac{\Delta\alpha_{\mathrm{dc}}}{2h}E^2 \simeq -4.4\,\mathrm{Hz} \tag{4.5.3}$$

or $\delta\nu_{\mathrm{dc,FSR}} = 400\,\mathrm{Hz}$ for scanning one cavity FSR. However, the more dominant shift will be likely to come from the proximity of the dielectric coatings [192]. However, this shift has probably a time constant of several days or even longer so that it less critical at the daily operation than the piezo induced shift.

4.6 Cavity assembly and alignment

From the size of the cavity and its number of degrees of freedom, it is obvious that the alignment procedure is challenging. Therefore, it is crucial to find an appropriate alignment algorithm.

The starting point are the plane mirrors. They are glued with the aid of a Teflon guide onto the fused silica base plate (figure 4.6.1a). The Teflon mask comprises a

[14] Noliac CSAP02

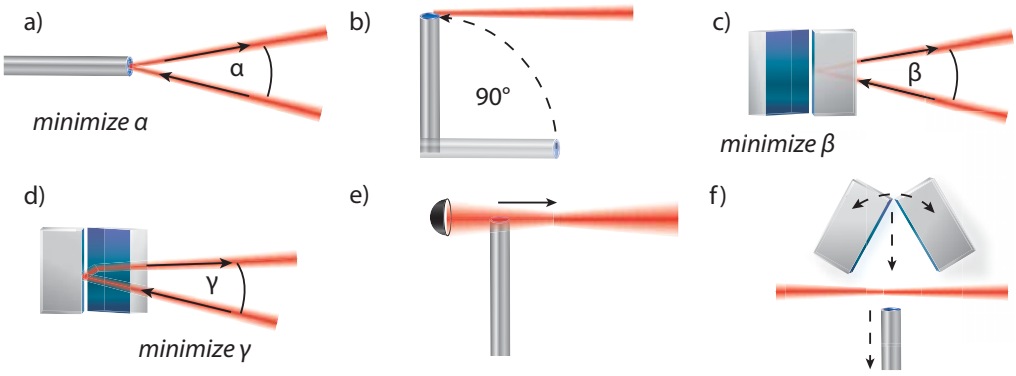

Figure 4.6.2: Illustration of the pre-alignment procedure as described in the text.

notch, which defines a 60° angle and a spacing of 100 µm between the two mirrors edges. Special care needs to be taken on choosing the appropriate glue: due to the small gap between the edges of the two plane mirrors, the capillary effect makes liquid glue climb the gap, which will then deposit on the coated surfaces. The two mirror normals span now a plane which needs to be aligned with the fiber mirror.

The assembling station is shown in figure 4.6.1b. It consists of two 3-axis translation stages[15], one for the laser beam alignment and the other is holding the fiber V-groove by means of a fiber gripper[16].

In order to facilitate the cavity alignment, the pre-alignment is crucial. Following procedure proves to be adequate (refer to figure 4.6.2):

a) After gluing the fiber into its V-groove, the laser beam is aligned on the fiber mirror structure so that the beam is retro-reflected.

b) The fiber is then turned by 90°. The laser beam serves now as a reference and its angle alignment is kept fix during the entire cavity assemblage. The fiber and the laser beam now span a plane which needs to be aligned with the plane of the mirrors' normal vectors.

c) Now, the plane mirrors are aligned on the laser beam. The base plate is placed on a 2-axis precision goniometer[17], a linear and rotational translation stage. First, by changing the goniometer angles, the normal-incident laser beam reflection of the incoupling mirror is algined onto itself.

[15]Thorlabs NanoMax™ Flexure Stage
[16]Piezosystem Jena GmbH, GRIPPY3
[17]OptoSigma, GOHT-40B20R

d) Second, the laser beam is incident onto the cavity mirrors via the substrates' 60° opening, where the fiber will be located afterwards. The beam is reflected on both mirrors and then aligned so that the reflection is parallel to the incident beam.

e) The laser beam waist is now moved to the fiber position, which coincides approximately with the cavity waist position. This is done adapting the knife-edge to find the position of the beam waist. For different positions of the collimation lens, the laser beam is progressively covered by the fiber tip and the transmitted signal is measured on a photodiode. The beam waist position is found when then the travel distance of the fiber to completely cover the laser beam reaches its minimum.

f) The fiber is translated perpendicularly to the laser beam by the approximate distance that corresponds to the desired cavity length. The plane mirrors are then adjusted towards the fiber until a transmission signal is seen on the CMOS camera.

From there on, the cavity alignment is an iterative process. By looking on the CMOS and photodiode signal, the cavity alignment is optimized on the TEM_{00} mode. Starting from a short cavity, the cavity length is then increased step-by-step and re-aligned after each length increase.

4.7 First prototype of the ring cavity

As to the time the substrates are not back from the high-reflective coating, the working principle of a miniaturized ring cavity and its alignment were tested with a preliminary low finesse cavity. The fiber structure is of the early stage of the fiber fabrication, i. e. the structure was not fully optimized. However, all geometrical parameters are the same as in the final high-finesse cavity. The fiber has the ROCs of $R_{\parallel}/R_{\perp} = 351\,\mu\mathrm{m}/260\,\mu\mathrm{m}$. The fiber and the two plane mirrors were coated with a 100 nm thick gold layer, leading to a theoretical reflectivity for an incident angle of 30° of $R_\mathrm{s} = 0.982$ and $R_\mathrm{p} = 0.978$ (refer to equation 4.7.2). The resulting finesse calculates as

$$\mathcal{F} = \frac{\pi \sqrt[4]{R^3}}{1 - \sqrt{R^3}}\,. \tag{4.7.1}$$

The finesse for s-polarized light is ≈ 123 and for p-polarized light ≈ 91. A picture of the cavity is shown in figure 4.7.1b. For the test cavity, a copper V-groove has been used to hold the fiber. The alignment procedure from section 4.6

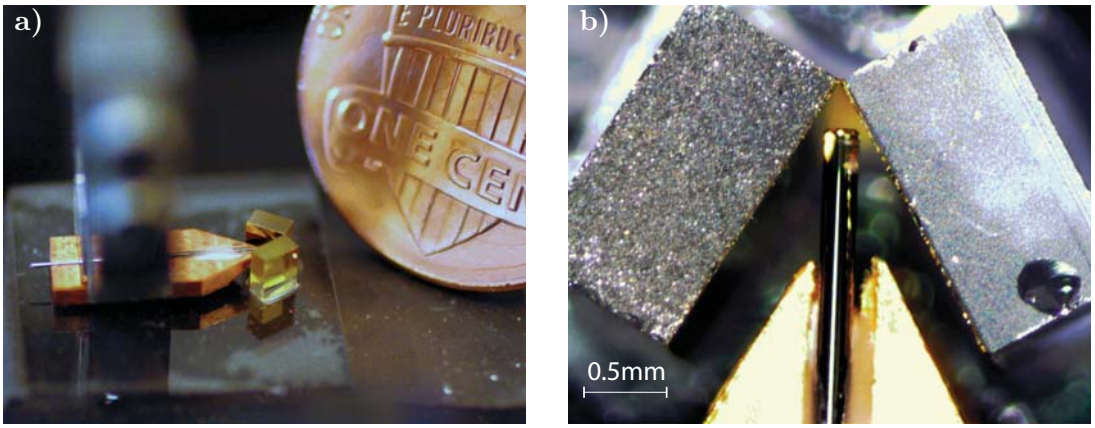

Figure 4.7.1: a) Photo of the preliminary gold cavity in comparison to a penny. The small, bright red reflection on the substrate is the incoupling beam. b) Zoom onto the cavity via a microscope.

has been applied and after a reasonable time, the transmission signal was observed first on the CMOS camera and could be optimized until a signal on photodiode appeared.

4.7.1 Results

Frequency spectrum: First of all, the mode spectrum of the low-finesse cavity was characterized. The results with pictures of the corresponding Hermite-Gaussian modes are shown in figure 4.7.2. It can be clearly seen that modes with an odd n are shifted by half a FSR and are degenerate for even n, as it is the case for the $\mathrm{TEM}_{02,20}$. Furthermore, from equation 4.2.4 the length of the cavity calculates to 573 µm and the ROCs to $R_{\parallel}/R_{\perp} = 348\,\mu\mathrm{m}/261\,\mu\mathrm{m}$

Astigmatism compensation: The proximity of the $\mathrm{TEM}_{02,20}$ to the fundamental mode is a useful aid to align the cavity towards the maximum astigmatic compensation. In contrast to the $\mathrm{TEM}_{01,10}$ modes, they are supposed to be degenerate if the cavity is well aligned and the effective ROCs of the fiber mirror seen by the intra-cavity beam are the same. This effect is shown in figure 4.7.3b, where a well and a misaligned cavity are compared. The alignment was optimized by rotating the plane mirror perpendicularly around the incoupling beam. Given the linewidth of the low-finesse cavity, the splitting between the two modes only allows a resolution of $\pm 5\,\mu$m of the ROCs, so that the deviation from the ideal ROCs $R_{\parallel}/R_{\perp} = 351\,\mu\mathrm{m}/262.5\,\mu\mathrm{m}$ for a perfect astigmatism is not resolvable. This, how-

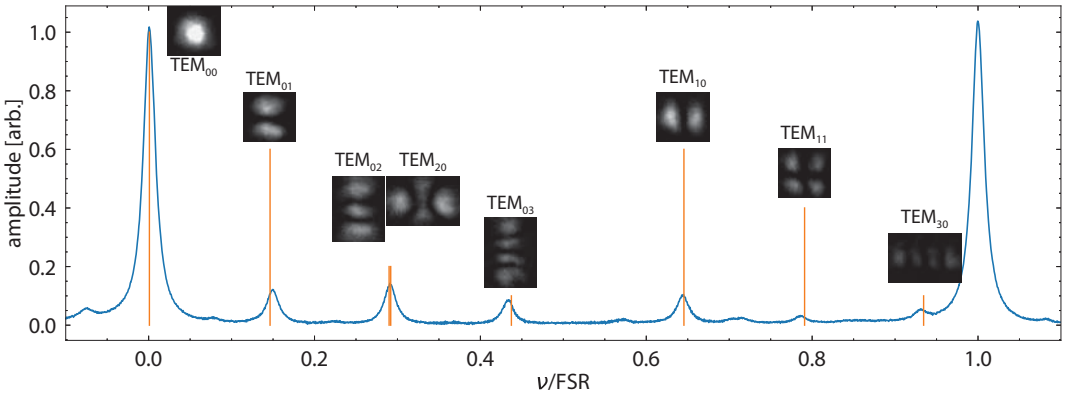

Figure 4.7.2: Mode spectrum measured of a 570 µm long cavity. The vertical orange lines correspond to the calculated mode spectrum. The cavity was intentionally misaligned to show the higher-order modes.

ever, will change for the high-finesse cavity and it will be also interesting to see to what extend slight deviations from the ideal ROCs of mirror can be compensated by the fiber rotation angles.

Furthermore, the cavity waist and its astigmatism was inferred by measuring the beam divergence of the cavity output beam. The transmitted mode of a cavity has the profile of the intracavity mode and therefore, the measurement of the transmitted mode waist and divergence gives information on the intra-cavity mode characteristics.

For that purpose, a CMOS camera was placed right behind the cavity and over a range of 1.5 cm, the expanding beam waist was measured. This measurement was repeated for several cavity lengths. The results are presented in figure 4.7.3a. The cavity waist drops with increasing cavity lengths and follows therefore the theoretical curve calculated from the fiber mirror's ROCs. It can be also seen that the cavity waist in the tangential plane is consistently higher than in the sagittal plane, as to be expected from the ROCs of the given fiber mirror. However, stray light in the setup affected the measurement even though a background picture was subtracted from the beam waist measurement photos. Therefore, it cannot be ultimately concluded on the extend of the remaining astigmatism and if it comes from the imperfect mirror shape or if a potential misalignment of the cavity has an impact on the astigmatism.

Polarization phase-shift and approaching concentricity: Another effect to be studied was the polarization-dependent phase shift. Based on the Fresnel equations, the polarization dependent phase shift for a metallic mirror with the complex refractive index $\tilde{n}_1 = n_1 + i\,k_1$ placed in air can be calculated. The reflection co-

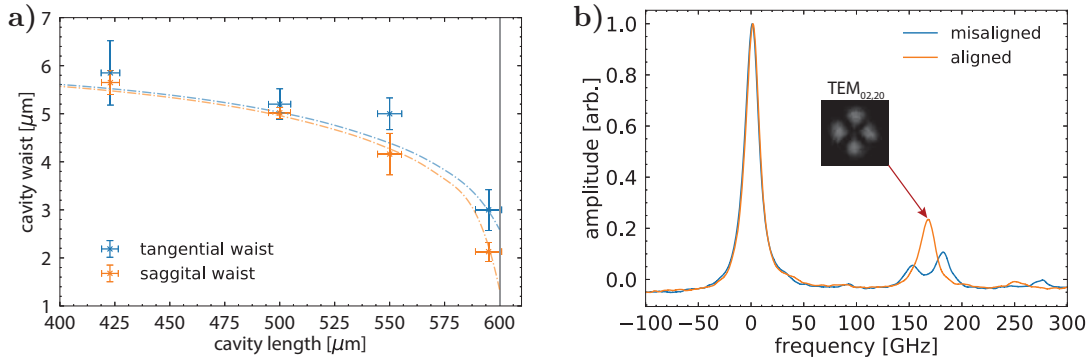

Figure 4.7.3: a) Shown are the reconstructed cavity waists in the tangential and sagittal plane based on the measured divergence angles of the output beam for different cavity lengths. The dashed lines indicate the theoretical waists based on the ROCs $R_{\parallel}/R_{\perp} = 351\,\mu\text{m}/260\,\mu\text{m}$. The gray vertical line indicates the concentric limit of the cavity. b) The difference of a well-aligned, non-astigmatic cavity and a misaligned cavity becomes apparent observing the degeneracy of the $\text{TEM}_{02,20}$ modes.

efficients for both polarizations read as follows:

$$\begin{aligned} r_s &= \frac{n_0 \cos\theta_i - \tilde{n}_1 \cos\theta_t}{n_0 \cos\theta_i + \tilde{n}_1 \cos\theta_t} \\ r_p &= \frac{\tilde{n}_1 \cos\theta_i - n_0 \cos\theta_t}{n_0 \cos\theta_t + \tilde{n}_1 \cos\theta_i}\,. \end{aligned} \tag{4.7.2}$$

Here, $n_0 = 1$ denotes the refraction index of air/vacuum. By converting r_s and r_p from complex to polar form, the phases ϕ_s and ϕ_p can be extracted. The polarization dependent phase shift is then simply the difference $\Delta\phi = \phi_s - \phi_p$.

In the case of the preliminary low-finesse cavity with an evaporated gold coating, the complex refractive index at 780 nm is $n_1 = 0.12383$ and $k_1 = 4.9228$ [193]. The polarization dephasing for one round trip calculates to $3 \times \Delta\phi \approx {}^{10}/_{9}\pi$ or 200°. This value is consistent with the measured phase shift shown in figure 4.7.4a, which amounts to 200°.

Eventually, the finesse was inferred for different cavity length. The cavity length was determined by means of scanning a Ti:sapphire laser[18], which itself was stabilized onto a wavemeter[19] with a 60 MHz resolution. The measured finesse for $s(p)$-polarization amounts to 135(101) and increases slightly towards a cavity length of

[18] M Squared Lasers, SolsTiS-2000
[19] HighFinesse, WS7-60

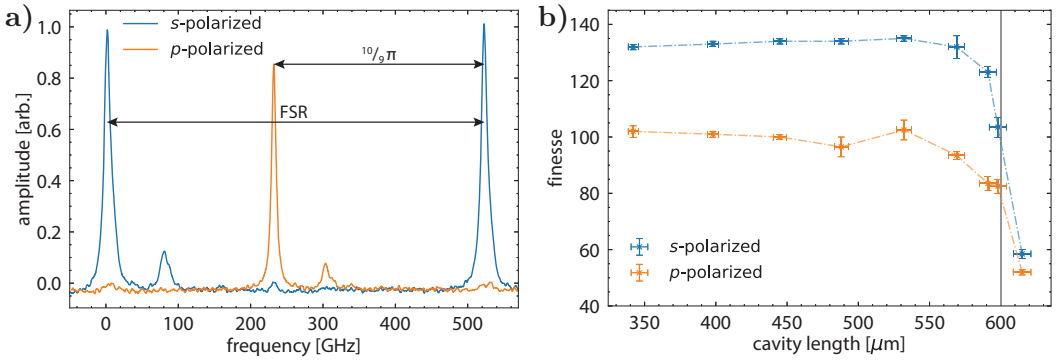

Figure 4.7.4: a) Polarization shift of a 575 µm long cavity. The polarization-dependent phase shift amounts to 200° and is in good agreement with the theory. b) Measurement of the finesse vs. cavity length for both polarizations. The gray vertical line indicates the concentric limit of the cavity.

550 µm, which is due to the non-ideal mode matching that was only designed for a long cavity. When the cavity length then approaches 600 µm, the finesse drops drastically as the cavity reaches an unstable region where $2R \sim L$.

4.8 Conclusion and outlook

In this chapter, the results of a prototype ring cavity of a length up to 600 µm have been reported. It could be shown, that the CO_2 cot milling technique allows to control and especially to compensate for the astigmatism present in triangular ring cavities. Within the measurement accuracy, it could be shown that the waist of the prototype cavity is nearly circular. The remaining astigmatism was expected from the shape of the fiber mirror. The polarization-dependent phase shift and finesse were measured and are in good agreement with the theoretical description of the ring cavity.

Overall, the results of this chapter are coherent to the design expectations and give reason to expect that the operation of a high-finesse ring cavity in a strontium experiment is feasible. An open question remains the parasitic standing wave, which is more likely to build up in a high- than in a low-finesse cavity.

Even though the high-finesse cavity is still under construction, it might be of interest to discuss the further potential of open micro-cavities outside the cold-atom community. figure 4.8.1a shows some ideas that could be added to a miniaturized ring cavity assembly. First of all, instead of working in free space, the incoupling

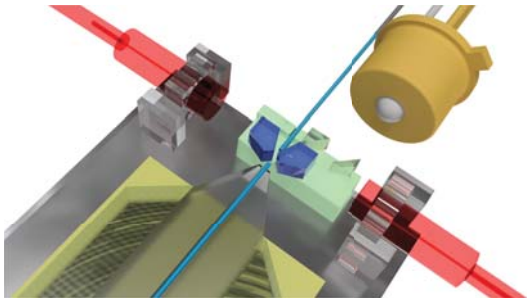

Figure 4.8.1: CAD-illustration of an advanced ring-cavity assembly. The fibers and the penta-prisms are shown in blue and the incoupling-fiber with GRIN-endcaps are colored in red. The photodiode depicted in top-right corner.

beam can be delivered by a pigtailed SM mode fiber which then guarantees stable cavity coupling over a long time period without the need of realignment. Furthermore, a second fiber could be glued onto the cavity substrate, facing the principle ring-cavity fiber. The resulting fiber cavity, which builds up through the gap between the plane substrates, can be used to lock the ring cavity, assuming that both cavities are strongly coupled through their proximity on the same substrate. Also, using penta prisms as plane mirror substrates allows to add more miniaturized beam analysis tools on the optical bench as the incoupling and reflected beam lie on different end-facets. An obvious add-on for a fully-integrated ring cavity assembly would be a small photodiode which picks up the reflection signal of the cavity at the second port of the penta prism.

Chapter

Conclusion

In this thesis, two complementary aspects of a new experiment have been described that opens the way for entanglement generation with alkaline-earth like atoms.

Chapter 2 described the conception and set-up of a new cold atom platform with strontium. It combines robustness and compactness and should ensure a high repetition rate of measurement, which is crucial for the acquisition of large datasets required for quantum state tomography. In contrast to other compact strontium platforms [63], this setup is designed to leave ample scope for the future implementation of experimental techniques in order to maintain a maximum of flexibility, such as intra-cavity imaging with transverse beams.

Incorporated into the design will be a high-finesse ring cavity. Chapters 3 and 4 detailed the progress towards the realization of this type of miniaturized cavity. It will be the core part of the new experiment, allowing to work with strontium in the strong-coupling regime. Owing to the immense effort from the predecessors, it has been possible to fabricate an elliptical mirror on a fiber tip, allowing to compensate for the astigmatism typically present in ring cavities. Despite the fact that only a low-finesse prototype has been assembled yet, the coherence of the experimental results with the design expectations allows to be rather optimistic that the high-finesse equivalent will hold the requirements for a cold experiments.

Outlook: entanglement for metrology and beyond

In the new experimental setup, the collective coupling between the atoms and the cavity can be used to generate many body entangled states. The principle design goal was to ensure a spatially uniform coupling of the atomic ensemble to the cavity mode so that the cavity interaction is *de facto* insensitive to the position of the atoms.

This new platform enters a very active experimental community, which works intensively on applying spin squeezing on atomic clocks. Nevertheless, a near-term goals for the experiment can be still to demonstrate spin squeezing on the intercombination lines of strontium [42]. Spin squeezing is a canonical example for metrologically useful entanglement and is first and foremost a prospective approach to improve the performance of optical clocks [194]. As atomic sensors are physically limited by the shot noise, squeezed spin states are the most straightforward route

to reach sub-SQL capabilities. Recently reported have been squeezing experiments approaching 20 dB beyond the SQL [85, 195].

In this context, a ring cavity opens even new opportunities. The possibility to inject two couterpropagating modes in the cavity gives rise to mutli-mode-type of squeezing as it has been proposed by Parkins *et al.* in 2006 [196].

A promising long-term avenue can be the generation of more complex entangled states. Quantum state carving [197, 198] is one of these promising approaches. In this scheme, a single photon illuminates the cavity and the dispersive atom-light coupling entangles every eigenstate of the collective atomic spin. By choosing the photon's frequency corresponding to one of the shifted cavity resonance frequencies, the atomic state will be deterministically projected into a Dicke state. This can be even further extended by spectrally shaping the photon. When the photon is in a superposition of different frequencies, the atomic state will be projected into the corresponding weighted superposition of atomic states. This method potentially allows to engineer complex entangled states of many atoms.

Appendix

Gaußian beams and transfer matrices

A

A.1 Gaußian beams

The fundamental Gaußian mode is a partial solution of the paraxial Helmholtz wave equation [199] and can be written in the normalized form as:

$$\psi(r,z) = u(r,z)\exp(-ikz) \tag{A.1.1}$$

$$= \sqrt{\frac{2}{\pi w(z)^2}}\exp\left[-\frac{r^2}{w(z)^2} - ikz - ik\frac{r^2}{2R(z)} + i\zeta(z)\right] \tag{A.1.2}$$

where $k = 2\pi/\lambda$ is the *wavenumber* and $u(r,z)$ is a scalar complex function that describes the nonplanar behaviour. A sketch of the intensity distribution is depicted in figure A.1.1a.

The geometric parameters are defined by the beam waist w_0 and evolve along the positive z-direction as follows:

- The spot size:

$$w(z) = w_0\sqrt{1 + \left(\frac{z}{z_R}\right)^2} \tag{A.1.3}$$

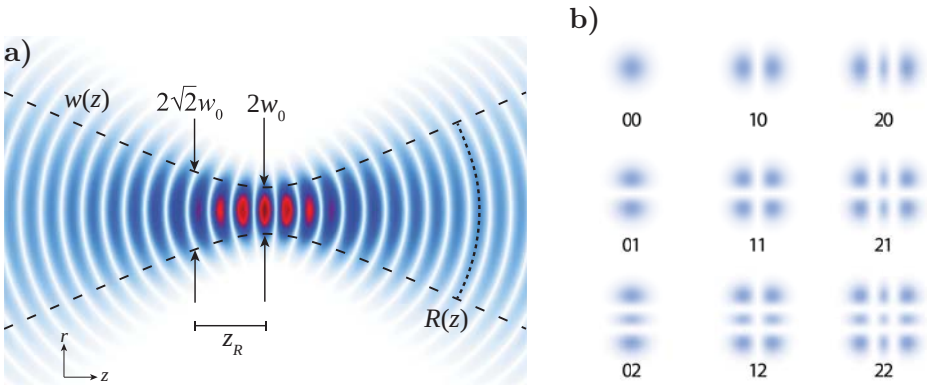

Figure A.1.1: a) Intensity profile of a Gaußian beam. b) Transverse modes.

- The radius of curvature of the wave front:

$$R(z) = z\left[1 + \left(\frac{z}{z_R}\right)^2\right] \tag{A.1.4}$$

- The Gouy phase is:

$$\zeta(z) = \arctan\left(\frac{z}{z_R}\right) \tag{A.1.5}$$

The Rayleigh length is defined as $z_R = \pi w_0^2/\lambda$ and is the distance from the beam waist w_0 to where the spot has increased by a factor $\sqrt{2}$. The Rayleigh length can be also seen as the distance that divides the near-field and mid-field of a Gaußian beam.

If one wants to consider the x and y direction independently, one could also write:

$$u(r, z) = u(x, z) \cdot u(y, z) \tag{A.1.6}$$

with

$$u(x, z) = \left(\frac{2}{\pi w_x(z)^2}\right)^{1/4} \exp\left[-\frac{x^2}{w_x(z)^2} - ik\frac{x^2}{2R_x(z)} + i\frac{\zeta(z)}{2}\right] \tag{A.1.7}$$

A.2 ABCD matrix formalism

Based on the Gaußian mode, we can now calculate the beam propagation in an optical element by means of the *ABCD matrix transformation* [167]. These matrices completely characterize the given optical element within the paraxial ray approximation, i.e. the angular displacements θ are assumed to be small enough to apply the small angle approximation. For this purpose we introduce the complex beam parameter $q(z)$ which subsumes the information about the spot size and the radius of curvature of its wave fronts:

$$\frac{1}{q(z)} = \frac{1}{R(z)} - i\frac{\lambda}{\pi w(z)^2} \tag{A.2.1}$$

This parameter changes as the beam propagates through a general optical element. The transformation can be described by a given $ABCD$ matrix:

$$q' = \frac{Aq + B}{Cq + D} \tag{A.2.2}$$

where q and q' correspond to the complex parameters at the input and output plane of the optical system.

equation A.1.2 can be then rewritten as a function of the complex parameter $q(z)$:

$$u(r,z) = \sqrt{\frac{2}{\pi w(z)^2}} \exp\left(-i\frac{kr^2}{2q(z)}\right) \tag{A.2.3}$$

The $ABCD$ for a propagation across a thin lens $M_l(f)$, through free space of distance l $M_p(l)$ and the reflection of a mirror plane M_r can be written as:

$$M_l(f) = \begin{pmatrix} 1 & 0 \\ -1/f & 1 \end{pmatrix} \quad M_p(l) = \begin{pmatrix} 1 & l \\ 0 & 1 \end{pmatrix} \quad M_r = \begin{pmatrix} 1 & 0 \\ 0 & 1 \end{pmatrix} \tag{A.2.4}$$

Appendix

Test on blue light induced finesse degradation

B

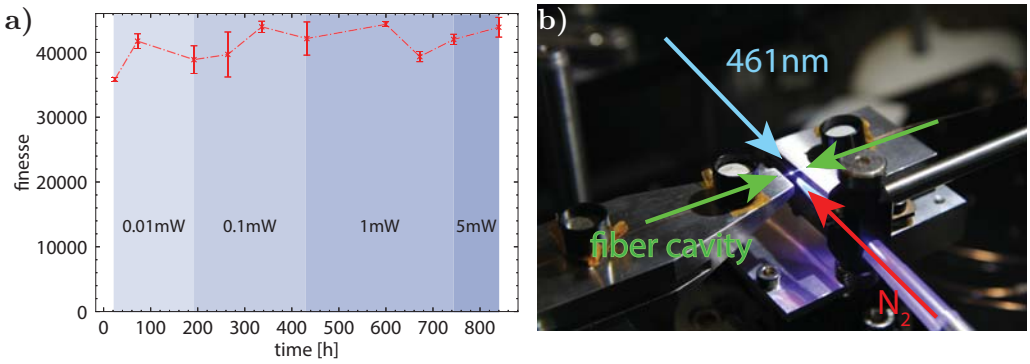

Figure B.0.1: a) shows the finesse evolving over time with different incident laser powers and b) shows the measurement setup.

In order to evaluate if stray light of the blue MOT beams will affect the coating of the high-finesse cavity, a simple test setup has build. It consisted in a 0.5 mm long fiber cavity of a finesse of $\mathcal{F} \approx 40\,000$. The fibers had the same coating then the fiber cavities of the TACC2 experiment [149]. The cavity was then exposed to a blue laser beam at 461 nm and the finesse was measured of the course of a month. Furthermore, the cavity was exposed to a constant flow of nitrogen to simulate a system under vacuum, i. e. the absence of oxygen.

As it can be seen in figure B.0.1a, the laser power at 461 nm was increased over time up to 5 mW. Nonetheless, no effect on the finesse could have been observed.

Personal statement: On the relevance of project management in academic research

Traditional project management is associated with a systematic approach and the application of numerous methodical tools. This allows to develop successful working strategies and is an indispensable component in industrial and political work environments. In academic research, however, project management is comparatively rare even though it fulfills all structural phases of a classical project: i) analysis and conception of ideas, ii) development of a research plan, iii) plan execution, iv) evaluation of the results and finally v) the project closure in form of publications. 'Projects fail because of a lack of project culture' – this motto holds true in industry, so the question is why project management is still an alien concept in fundamental research.

An essential reason is the difference in the definition of project goals in industrial and university working methods. While the former has a product or an end result as its goal, university research is much more agile. The final outcome is often elusive because projects can be completely redesigned based on the progress and findings to date and can go in a completely new direction. This high degree of uncertainty is desired in the scientific environment and represents an unacceptable risk in most companies. Other reasons why project management is unusual in research are: 1) Researchers see themselves, in a way, as artists and not as managers. Management and leadership are associated with unnecessary administration and are perceived as annoying, as they distract from the actual research topic and one feels restricted in one's freedom. 2) Researchers and scientists are individualists, ambitious and often focused on their own development and career. They therefore do not always fit unreservedly into a project organization and a team.

Nevertheless, project management is not only a narrative of guides, but it has some actual purpose. If one analyses problems and failures in research projects, they can be often traced back to the lack of project management: Objectives and milestones are formulated only roughly, if at all. Project structuring, scheduling and resource planning as well as risk assessment are considered dispensable as the research field and scientific approach are known from numerous previous projects. In the course of the project work, the research objectives are derived from the developed material, which in turn depends on the available time and resources. The research process is not target- but input-oriented. It is controlled

by chances and personal ambition. It is certainly not necessary to apply classical project management methods to the extent that is appropriate in the private sector. Nevertheless, many tools of classical and especially agile project management can be quickly and easily adapted for smaller research projects – without restricting creativity and academic freedom.

A well-defined roadmap with milestones and goals is essential and allows to anticipate possible bottlenecks or problems. Particularly in small teams, where manpower is a scarce resource, such structuring is important in order to prioritize a large number of issues and sub-projects. Although many aspects of a project can be of interest, they do not necessarily contribute to the global success of the research project. Separating these secondary sub-projects from the essential aspects of the research project is therefore all the more important in small teams. It can therefore sometimes be better to outsource technical work from the outset in order to avoid considerable delays in project times. Project management therefore helps to reduce effort, to track progress (or its absence) and to respond quickly to deviations from key goal.

Particularly in university research, which lives from Ph.D. students and thus young graduates, more effort has to be put into the macro management on the PI side. It is simply a question of fairness to create an attractive working environment in which (underpaid) Ph.D. students can execute their Ph.D. project rigorously. However, teams must also agree on the benefits of project management. Otherwise, the impression will quickly arise that it only serves the purpose of surveillance. The benefit lies in the process of constant self-observation and self-correction during the project lifecycle.

But this also requires a rethink in the education of scientists. Project management training has traditionally not been an integral part of the academic curriculum, even though it is an additional element of goal setting and organization. This way of thinking around the organization of experiments, the design of its outline and then the direct path to publication makes the scientist a more productive individual with not too much more effort.

If one also looks at academic research in a broader context, researchers also have a certain responsibility to the taxpayer. Since universities often depend on government subsidies, every scientist should show himself responsible that he uses its fund purposefully. The same standards that researchers apply to the handling of taxpayers' money in other domains should also be set for themselves. Otherwise one should not be surprised that research budgets are continuously reduced and that the reputation of fundamental research as a money burning machine cements.

Bibliography

[1] Claude N. Cohen-Tannoudji. "Nobel Lecture: Manipulating atoms with photons". In: *Reviews of Modern Physics* 70.3 (1998), pp. 707–719. ISSN: 0034-6861. DOI: 10.1103/RevModPhys.70.707 (cit. on p. I).

[2] William Daniel Phillips. "Nobel Lecture: Laser cooling and trapping of neutral atoms". In: *Reviews of Modern Physics* 70.3 (1998), pp. 721–741. ISSN: 0034-6861. DOI: 10.1103/RevModPhys.70.721 (cit. on p. I).

[3] A. Ashkin. "Trapping of Atoms by Resonance Radiation Pressure". In: *Physical Review Letters* 40.12 (1978), pp. 729–732. ISSN: 0031-9007. DOI: 10.1103/PhysRevLett.40.729 (cit. on p. I).

[4] T. W. Hänsch and A. L. Schawlow. "Cooling of gases by laser radiation". In: *Optics Communications* 13.1 (1975), pp. 68–69. ISSN: 00304018. DOI: 10.1016/0030-4018(75)90159-5 (cit. on p. I).

[5] D. J. Wineland and H. G. Dehmelt. "Principles of the stored ion calorimeter". In: *Journal of Applied Physics* 46.2 (1975), pp. 919–930. ISSN: 00218979. DOI: 10.1063/1.321602 (cit. on p. I).

[6] William Daniel Phillips and Harold Metcalf. "Laser Deceleration of an Atomic Beam". In: *Physical Review Letters* 48.9 (1982), pp. 596–599. ISSN: 0031-9007. DOI: 10.1103/PhysRevLett.48.596 (cit. on pp. I, 33).

[7] Steven Chu et al. "Experimental observation of optically trapped atoms". In: *Physical review letters* 57.3 (1986), pp. 314–317. ISSN: 1079-7114. DOI: 10.1103/PhysRevLett.57.314 (cit. on p. I).

[8] Raab et al. "Trapping of neutral sodium atoms with radiation pressure". In: *Physical review letters* 59.23 (1987), pp. 2631–2634. ISSN: 1079-7114. DOI: 10.1103/PhysRevLett.59.2631 (cit. on p. I).

[9] A. L. Migdall et al. "First observation of magnetically trapped neutral atoms". In: *Physical review letters* 54.24 (1985), pp. 2596–2599. ISSN: 1079-7114. DOI: 10.1103/PhysRevLett.54.2596 (cit. on p. I).

[10] M. H. Anderson et al. "Observation of bose-einstein condensation in a dilute atomic vapor". In: *Science* 269.5221 (1995), pp. 198–201. ISSN: 0036-8075. DOI: 10.1126/science.269.5221.198 (cit. on p. I).

[11] K. B. Davis et al. "Bose-Einstein condensation in a gas of sodium atoms". In: *Physical review letters* 75.22 (1995), pp. 3969–3973. ISSN: 1079-7114. DOI: 10.1103/PhysRevLett.75.3969 (cit. on p. I).

[12] James K. Thompson, Gerhard Rempe, and H. J. Kimble. "Observation of normal-mode splitting for an atom in an optical cavity". In: *Physical review letters* 68.8 (1992), pp. 1132–1135. ISSN: 1079-7114. DOI: 10.1103/PhysRevLett.68.1132 (cit. on p. I).

[13] A. Furusawa et al. "Unconditional quantum teleportation". In: *Science (New York, N.Y.)* 282.5389 (1998), pp. 706–709. ISSN: 0036-8075. DOI: 10.1126/science.282.5389.706 (cit. on p. I).

[14] D. Leibfried et al. "Quantum dynamics of single trapped ions". In: *Reviews of Modern Physics* 75.1 (2003), pp. 281–324. ISSN: 0034-6861. DOI: 10.1103/RevModPhys.75.281 (cit. on p. I).

[15] Y. Kaluzny et al. "Observation of Self-Induced Rabi Oscillations in Two-Level Atoms Excited Inside a Resonant Cavity: The Ringing Regime of Superradiance". In: *Physical Review Letters* 51.13 (1983), pp. 1175–1178. ISSN: 0031-9007. DOI: 10.1103/PhysRevLett.51.1175 (cit. on p. I).

[16] J. McKeever et al. "Deterministic generation of single photons from one atom trapped in a cavity". In: *Science (New York, N.Y.)* 303.5666 (2004), pp. 1992–1994. ISSN: 0036-8075. DOI: 10.1126/science.1095232 (cit. on p. I).

[17] A. Wallraff et al. "Strong coupling of a single photon to a superconducting qubit using circuit quantum electrodynamics". In: *Nature* 431.7005 (2004), pp. 162–167. ISSN: 0028-0836. DOI: 10.1038/nature02851 (cit. on p. I).

[18] T. Niemczyk et al. "Circuit quantum electrodynamics in the ultrastrong-coupling regime". In: *Nature Physics* 6.10 (2010), pp. 772–776. ISSN: 1745-2473. DOI: 10.1038/nphys1730 (cit. on p. I).

[19] J. Kelly et al. "State preservation by repetitive error detection in a superconducting quantum circuit". In: *Nature* 519.7541 (2015), pp. 66–69. ISSN: 0028-0836. DOI: 10.1038/nature14270 (cit. on p. I).

[20] J. R. Petta et al. "Coherent manipulation of coupled electron spins in semiconductor quantum dots". In: *Science (New York, N.Y.)* 309.5744 (2005), pp. 2180–2184. ISSN: 0036-8075. DOI: 10.1126/science.1116955 (cit. on p. I).

[21] K. D. Petersson et al. "Circuit quantum electrodynamics with a spin qubit". In: *Nature* 490.7420 (2012), pp. 380–383. ISSN: 0028-0836. DOI: 10.1038/nature11559 (cit. on p. I).

[22] J. J. Viennot et al. "QUANTUM INFORMATION. Coherent coupling of a single spin to microwave cavity photons". In: *Science (New York, N.Y.)* 349.6246 (2015), pp. 408–411. ISSN: 0036-8075. DOI: 10.1126/science.aaa3786 (cit. on p. I).

[23] C. Langer et al. “Long-lived qubit memory using atomic ions”. In: *Physical Review Letters* 95.6 (2005), p. 060502. ISSN: 0031-9007. DOI: 10.1103/PhysRevLett.95.060502 (cit. on p. II).

[24] E. Schrödinger. “Discussion of Probability Relations between Separated Systems”. In: *Mathematical Proceedings of the Cambridge Philosophical Society* 31.4 (1935), pp. 555–563. ISSN: 0305-0041. DOI: 10.1017/S0305004100013554 (cit. on p. II).

[25] Ryszard Horodecki et al. “Quantum entanglement”. In: *Reviews of Modern Physics* 81.2 (2009), pp. 865–942. ISSN: 0034-6861. DOI: 10.1103/RevModPhys.81.865 (cit. on p. II).

[26] Alain Aspect, Jean Dalibard, and Gérard Roger. “Experimental Test of Bell’s Inequalities Using Time- Varying Analyzers”. In: *Physical Review Letters* 49.25 (1982), pp. 1804–1807. ISSN: 0031-9007. DOI: 10.1103/PhysRevLett.49.1804 (cit. on p. II).

[27] B. Hensen et al. “Loophole-free Bell inequality violation using electron spins separated by 1.3 kilometres”. In: *Nature* 526.7575 (2015), pp. 682–686. ISSN: 0028-0836. DOI: 10.1038/nature15759 (cit. on p. II).

[28] Cirac and Zoller. “Quantum Computations with Cold Trapped Ions”. In: *Physical review letters* 74.20 (1995), pp. 4091–4094. ISSN: 1079-7114. DOI: 10.1103/PhysRevLett.74.4091 (cit. on pp. II, 8).

[29] Daniel Loss and David P. DiVincenzo. “Quantum computation with quantum dots”. In: *Physical Review A* 57.1 (1998), pp. 120–126. ISSN: 1050-2947. DOI: 10.1103/PhysRevA.57.120 (cit. on p. II).

[30] R. Gerritsma et al. “Quantum simulation of the Dirac equation”. In: *Nature* 463.7277 (2010), pp. 68–71. ISSN: 0028-0836. DOI: 10.1038/nature08688 (cit. on p. II).

[31] Immanuel Bloch, Jean Dalibard, and Sylvain Nascimbène. “Quantum simulations with ultracold quantum gases”. In: *Nature Physics* 8.4 (2012), pp. 267–276. ISSN: 1745-2473. DOI: 10.1038/nphys2259 (cit. on p. II).

[32] Dik Bouwmeester et al. “Experimental quantum teleportation”. In: *Nature* 390.6660 (1997), pp. 575–579. ISSN: 0028-0836. DOI: 10.1038/37539 (cit. on p. II).

[33] K. Stannigel et al. “Optomechanical transducers for long-distance quantum communication”. In: *Physical review letters* 105.22 (2010), p. 220501. ISSN: 1079-7114. DOI: 10.1103/PhysRevLett.105.220501 (cit. on p. II).

[34] Kitagawa and Ueda. "Squeezed spin states". In: *Physical Review A* 47.6 (1993), pp. 5138–5143. ISSN: 1050-2947. DOI: 10.1103/physreva.47.5138 (cit. on pp. III, 10).

[35] Florian Haas. "Création d'états intriqués d'un ensemble d'atomes dans une cavité optique". Dissertation. Paris: Université Pierre et Marie Curie - Paris VI, 2014 (cit. on pp. IV, 9).

[36] Giovanni Barontini et al. "Deterministic generation of multiparticle entanglement by quantum Zeno dynamics". In: *Science* 349.6254 (2015), pp. 1317–1321. ISSN: 0036-8075. DOI: 10.1126/science.aaa0754 (cit. on p. IV).

[37] Guilhem Dubois. "Preparation, manipulation and detection of single atoms on a chip". Dissertation. Paris: Université Pierre et Marie Curie - Paris VI, 2009 (cit. on p. 1).

[38] Claude Cohen-Tannoudji, Jacques Dupont-Roc, and Gilbert Grynberg. *Atom-photon interactions: Basic processes and applications*. Wiley science paperback series. New York, NY: Wiley, 2008. ISBN: 9780471293361. DOI: 10.1002/9783527617197. URL: http://www3.interscience.wiley.com/cgi-bin/homepage/?isbn=9783527617197 (cit. on pp. 1–3).

[39] Christopher Gerry and Peter Knight. *Introductory Quantum Optics*. Cambridge: Cambridge University Press, 2004. ISBN: 9780511791239. DOI: 10.1017/CBO9780511791239 (cit. on p. 2).

[40] E. T. Jaynes and F. W. Cummings. "Comparison of quantum and semiclassical radiation theories with application to the beam maser". In: *Proceedings of the IEEE* 51.1 (1963), pp. 89–109. ISSN: 0018-9219. DOI: 10.1109/PROC.1963.1664 (cit. on p. 2).

[41] Ian D. Leroux, Monika H. Schleier-Smith, and Vladan Vuletić. "Implementation of cavity squeezing of a collective atomic spin". In: *Physical review letters* 104.7 (2010), p. 073602. ISSN: 1079-7114. DOI: 10.1103/PhysRevLett.104.073602 (cit. on pp. 3, 4).

[42] Robert J. Lewis-Swan et al. "Robust Spin Squeezing via Photon-Mediated Interactions on an Optical Clock Transition". In: *Physical review letters* 121.7 (2018), p. 070403. ISSN: 1079-7114. DOI: 10.1103/PhysRevLett.121.070403 (cit. on pp. 3, 113).

[43] Haruka Tanji-Suzuki et al. "Interaction between Atomic Ensembles and Optical Resonators: Classical Description". In: (2011) (cit. on p. 4).

[44] E. M. Purcell. "Proceedings of the American Physical Society". In: *Physical Review* 69.11-12 (1946), p. 674. ISSN: 0031-899X. DOI: 10.1103/PhysRev.69.674 (cit. on p. 4).

[45] F. T. Arecchi et al. “Atomic Coherent States in Quantum Optics”. In: *Physical Review A* 6.6 (1972), pp. 2211–2237. ISSN: 1050-2947. DOI: 10.1103/PhysRevA.6.2211 (cit. on p. 5).

[46] Michael Tavis and Frederick W. Cummings. “Exact Solution for an N -Molecule—Radiation-Field Hamiltonian”. In: *Physical Review* 170.2 (1968), pp. 379–384. ISSN: 0031-899X. DOI: 10.1103/PhysRev.170.379 (cit. on p. 6).

[47] R. H. Dicke. “Coherence in Spontaneous Radiation Processes”. In: *Physical Review* 93.1 (1954), pp. 99–110. ISSN: 0031-899X. DOI: 10.1103/PhysRev.93.99 (cit. on p. 6).

[48] Markus Gangl and Helmut Ritsch. “Cold atoms in a high- Q ring cavity”. In: *Physical Review A* 61.4 (2000), p. 681. ISSN: 1050-2947. DOI: 10.1103/PhysRevA.61.043405 (cit. on p. 7).

[49] Hubert Stoop, Pawel Masiak, and Kazimierz Rzaz-dotewski. “Atomic wave packet in a ring cavity”. In: *Physical Review A* 55.3 (1997), pp. 2254–2266. ISSN: 1050-2947. DOI: 10.1103/PhysRevA.55.2254 (cit. on p. 7).

[50] R. M. Sandner, W. Niedenzu, and H. Ritsch. “Subrecoil cavity cooling towards degeneracy: A numerical study”. In: *EPL (Europhysics Letters)* 104.4 (2013), p. 43001. ISSN: 0295-5075. DOI: 10.1209/0295-5075/104/43001 (cit. on p. 7).

[51] A. Hemmerich. “Quantum entanglement in dilute optical lattices”. In: *Physical Review A* 60.2 (1999), pp. 943–946. ISSN: 1050-2947. DOI: 10.1103/PhysRevA.60.943 (cit. on p. 7).

[52] R. Bonifacio and L. de Salvo. “Collective atomic recoil laser (CARL) optical gain without inversion by collective atomic recoil and self-bunching of two-level atoms”. In: *Nuclear Instruments and Methods in Physics Research Section A: Accelerators, Spectrometers, Detectors and Associated Equipment* 341.1-3 (1994), pp. 360–362. ISSN: 01689002. DOI: 10.1016/0168-9002(94)90382-4 (cit. on p. 8).

[53] Dietmar Kruse et al. “Cold atoms in a high- Q ring cavity”. In: *Physical Review A* 67.5 (2003). ISSN: 1050-2947. DOI: 10.1103/PhysRevA.67.051802 (cit. on p. 8).

[54] J. Bochmann et al. “Lossless state detection of single neutral atoms”. In: *Physical review letters* 104.20 (2010), p. 203601. ISSN: 1079-7114. DOI: 10.1103/PhysRevLett.104.203601 (cit. on p. 8).

[55] Roger Gehr et al. “Cavity-based single atom preparation and high-fidelity hyperfine state readout”. In: *Physical review letters* 104.20 (2010), p. 203602. ISSN: 1079-7114. DOI: 10.1103/PhysRevLett.104.203602 (cit. on p. 8).

[56] Y. Takahashi et al. "Quantum nondemolition measurement of spin via the paramagnetic Faraday rotation". In: *Physical Review A* 60.6 (1999), pp. 4974–4979. ISSN: 1050-2947. DOI: 10.1103/PhysRevA.60.4974 (cit. on p. 10).

[57] Kuzmich, Mandel, and Bigelow. "Generation of spin squeezing via continuous quantum nondemolition measurement". In: *Physical review letters* 85.8 (2000), pp. 1594–1597. ISSN: 1079-7114. DOI: 10.1103/PhysRevLett.85.1594 (cit. on p. 10).

[58] Zilong Chen et al. "Cavity-aided nondemolition measurements for atom counting and spin squeezing". In: *Physical Review A* 89.4 (2014). ISSN: 1050-2947. DOI: 10.1103/PhysRevA.89.043837 (cit. on p. 11).

[59] N. Kostylev et al. "Sub-Doppler cooling of ytterbium with the ˆ1S_0–ˆ1P_1 transition including ˆ171Yb (I=1/2)". In: *Journal of the Optical Society of America B* 31.7 (2014), p. 1614. ISSN: 0740-3224. DOI: 10.1364/JOSAB.31.001614 (cit. on p. 12).

[60] Alexander Batär. "Erzeugung und Charakterisierung ultrakalter Rubidium- und Ytterbiumatome: Auf dem Weg zu einem gemischten Quantengas". Dissertation. Düsseldorf: Heinrich-Heine-Universität Düsseldorf, 2005 (cit. on p. 12).

[61] Alexandre Cooper et al. "Alkaline-Earth Atoms in Optical Tweezers". In: *Physical Review X* 8.4 (2018). ISSN: 2160-3308. DOI: 10.1103/PhysRevX.8.041055 (cit. on pp. 12, 35).

[62] Simon Stellmer and Florian Schreck. "Reservoir spectroscopy of 5s5p3P2 – 5snd3D1,2,3 transitions in strontium". In: *Physical Review A* 90.2 (2014). ISSN: 1050-2947. DOI: 10.1103/PhysRevA.90.022512 (cit. on p. 12).

[63] William Bowden et al. *A pyramid MOT with integrated optical cavities as a cold atom platform for an optical lattice clock*. URL: http://arxiv.org/pdf/1907.13429v1 (cit. on pp. 12, 113).

[64] Alexey V. Taichenachev et al. "Magnetic Field-Induced Spectroscopy of Forbidden Optical Transitions with Application to Lattice-Based Optical Atomic Clocks". In: *Physical Review Letters* 96.8 (2006). ISSN: 0031-9007. DOI: 10.1103/PhysRevLett.96.083001 (cit. on p. 12).

[65] Vitaly D. Ovsiannikov et al. "Magic-wave-induced S01−P03 transition in even isotopes of alkaline-earth-metal-like atoms". In: *Physical Review A* 75.2 (2007). ISSN: 1050-2947. DOI: 10.1103/PhysRevA.75.020501 (cit. on p. 12).

[66] Masami Yasuda et al. “Photoassociation spectroscopy of Sr88: Reconstruction of the wave function near the last node”. In: *Physical Review A* 73.1 (2006). ISSN: 1050-2947. DOI: 10.1103/PhysRevA.73.011403 (cit. on pp. 13, 15).

[67] R. Drozdowski et al. “Radiative lifetimes of the lowest 3P1 metastable states of Ca and Sr”. In: *Zeitschrift fr Physik D Atoms, Molecules and Clusters* 41.2 (1997), pp. 125–131. ISSN: 0178-7683. DOI: 10.1007/s004600050300 (cit. on p. 13).

[68] Brian H. Bransden and Charles Jean Joachain. *Physics of atoms and molecules*. 2. ed., [Nachdr.] Harlow: Prentice Hall, ca. 2010. ISBN: 978-0582356924 (cit. on p. 13).

[69] V. A. Dzuba and A. Derevianko. “Dynamic polarizabilities and related properties of clock states of the ytterbium atom”. In: *Journal of Physics B: Atomic, Molecular and Optical Physics* 43.7 (2010), p. 074011. ISSN: 0953-4075. DOI: 10.1088/0953-4075/43/7/074011 (cit. on p. 14).

[70] Martin M. Boyd. “High Precision Spectroscopy of Strontium in an Optical Lattice: Towards a New Standard for Frequency and Time”. Dissertation. Boulder: University of Colorado, 2007 (cit. on p. 14).

[71] H. J. Andrä et al. “Lifetimes of levels in neutral strontium (Sr i)*”. In: *Journal of the Optical Society of America* 65.12 (1975), p. 1410. ISSN: 0030-3941. DOI: 10.1364/JOSA.65.001410 (cit. on p. 15).

[72] W. H. Parkinson, E. M. Reeves, and F. S. Tomkins. “Neutral calcium, strontium and barium: Determination of f values of the principal series by the hook method”. In: *Journal of Physics B: Atomic and Molecular Physics* 9.2 (1976), pp. 157–165. ISSN: 0022-3700. DOI: 10.1088/0022-3700/9/2/006 (cit. on p. 15).

[73] W. R. S. Garton et al. “Measurement of oscillator strengths in the ultraviolet by magneto-optical rotation”. In: *Journal of Physics B: Atomic and Molecular Physics* 16.3 (1983), pp. 389–397. ISSN: 0022-3700. DOI: 10.1088/0022-3700/16/3/014 (cit. on p. 15).

[74] G. Jönsson et al. “Natural radiative lifetimes in the1 P 1 and1 F 3 sequences of Sr I”. In: *Zeitschrift fr Physik A Atoms and Nuclei* 316.3 (1984), pp. 255–258. ISSN: 0340-2193. DOI: 10.1007/BF01439897 (cit. on p. 15).

[75] N. Vaeck, M. Godefroid, and Jo/rgen E. Hansen. “Multiconfiguration Hartree-Fock calculations for singlet terms in neutral strontium”. In: *Physical Review A* 38.6 (1988), pp. 2830–2845. ISSN: 1050-2947. DOI: 10.1103/PhysRevA.38.2830 (cit. on p. 15).

[76] D. A. Miller et al. "Collisional energy transfer between excited-state strontium and noble-gas atoms". In: *Physical Review A* 46.3 (1992), pp. 1303–1309. ISSN: 1050-2947. DOI: 10.1103/PhysRevA.46.1303 (cit. on p. 15).

[77] J. P. Connerade et al. "Atomic f-value measurements of high Rydberg members by pulsed laser-based magneto-optical spectroscopy". In: *Journal of Physics B: Atomic, Molecular and Optical Physics* 25.7 (1992), pp. 1405–1426. ISSN: 0953-4075. DOI: 10.1088/0953-4075/25/7/012 (cit. on p. 15).

[78] H. G. C. Werij et al. "Oscillator strengths and radiative branching ratios in atomic Sr". In: *Physical Review A* (1992). ISSN: 1050-2947 (cit. on p. 15).

[79] Sergey G. Porsev et al. "Determination of Sr properties for a high-accuracy optical clock". In: *Physical Review A* 78.3 (2008). ISSN: 1050-2947. DOI: 10.1103/PhysRevA.78.032508 (cit. on p. 15).

[80] Xiaoji Zhou et al. "Magic wavelengths for terahertz clock transitions". In: *Physical Review A* 81.1 (2010). ISSN: 1050-2947. DOI: 10.1103/PhysRevA.81.012115 (cit. on p. 15).

[81] M. J. Martin et al. "A Quantum Many-Body Spin System in an Optical Lattice Clock". In: *Science* 341.6146 (2013), pp. 632–636. ISSN: 0036-8075. DOI: 10.1126/science.1236929 (cit. on p. 15).

[82] H. Uys et al. "Decoherence due to elastic Rayleigh scattering". In: *Physical review letters* 105.20 (2010), p. 200401. ISSN: 1079-7114. DOI: 10.1103/PhysRevLett.105.200401 (cit. on p. 15).

[83] R. Ozeri et al. "Hyperfine coherence in the presence of spontaneous photon scattering". In: *Physical Review Letters* 95.3 (2005), p. 030403. ISSN: 0031-9007. DOI: 10.1103/PhysRevLett.95.030403 (cit. on p. 15).

[84] M. Saffman et al. "Spin squeezing of atomic ensembles by multicolor quantum nondemolition measurements". In: *Physical Review A* 79.2 (2009), p. 81. ISSN: 1050-2947. DOI: 10.1103/PhysRevA.79.023831 (cit. on p. 15).

[85] Kevin C. Cox et al. "Deterministic Squeezed States with Collective Measurements and Feedback". In: *Physical review letters* 116.9 (2016), p. 093602. ISSN: 1079-7114. DOI: 10.1103/PhysRevLett.116.093602 (cit. on pp. 15, 114).

[86] Eugene S. Polzik and Jun Ye. "Entanglement and spin squeezing in a network of distant optical lattice clocks". In: *Physical Review A* 93.2 (2016). ISSN: 1050-2947. DOI: 10.1103/PhysRevA.93.021404 (cit. on p. 16).

[87] Matthew A. Norcia et al. "Superradiance on the millihertz linewidth strontium clock transition". In: *Science advances* 2.10 (2016), e1601231. DOI: 10.1126/sciadv.1601231 (cit. on p. 16).

[88] Boris Braverman et al. “Near-Unitary Spin Squeezing in ˆ171Yb”. In: *Physical review letters* 122.22 (2019), p. 223203. ISSN: 1079-7114. DOI: 10.1103/PhysRevLett.122.223203 (cit. on p. 16).

[89] S. Origlia et al. “Towards an optical clock for space: Compact, high-performance optical lattice clock based on bosonic atoms”. In: *Physical Review A* 98.5 (2018). ISSN: 1050-2947. DOI: 10.1103/PhysRevA.98.053443 (cit. on p. 19).

[90] G. L. Weissler, ed. *Vacuum physics and technology*. Vol. 14. Methods of experimental physics. New York: Acad. Press, 1979. ISBN: 0124759149. URL: http://www.sciencedirect.com/science/publication?issn=0076695X&volume=14 (cit. on p. 21).

[91] Md Abdullah A. Mamun et al. “Effect of heat treatments and coatings on the outgassing rate of stainless steel chambers”. In: *Journal of Vacuum Science & Technology A: Vacuum, Surfaces, and Films* 32.2 (2014), p. 021604. ISSN: 0734-2101. DOI: 10.1116/1.4853795 (cit. on p. 21).

[92] John F. O’Hanlon. *A User’s Guide to Vacuum Technology*. Hoboken, NJ, USA: John Wiley & Sons, Inc, 2003. ISBN: 9780471467168. DOI: 10.1002/0471467162 (cit. on p. 22).

[93] K. J. Ross and B. Sonntag. “High temperature metal atom beam sources”. In: *Review of Scientific Instruments* 66.9 (1995), pp. 4409–4433. ISSN: 1089-7623. DOI: 10.1063/1.1145337 (cit. on p. 22).

[94] Ole Kock et al. “Laser controlled atom source for optical clocks”. In: *Scientific Reports* 6 (2016), srep37321. ISSN: 2045-2322. DOI: 10.1038/srep37321. URL: https://www.nature.com/articles/srep37321.pdf (cit. on p. 23).

[95] William M. Haynes, David R. Lide, and Thomas J. Bruno. *CRC handbook of chemistry and physics: A ready-reference book of chemical and physical data*. 2015-2016, 96th Edition. Boca Raton, Florida: CRC Press, 2015. ISBN: 1482260964 (cit. on p. 23).

[96] Norman Ramsey. *Molecular beams*. Oxford science publications. Oxford and New York: Clarendon Press and Oxford University Press, 1985, ©1956. ISBN: 9780198520214 (cit. on p. 23).

[97] F. Sorrentino et al. “Laser cooling and trapping of atomic strontium for ultracold atom physics, high-precision spectroscopy and quantum sensors”. In: *Modern Physics Letters B* 20.21 (2006), pp. 1287–1320. ISSN: 0217-9849. DOI: 10.1142/S0217984906011682 (cit. on pp. 23, 28).

[98] Nathaniel Warren Alcock. *Bonding and structure: Structural principles in inorganic and organic chemistry*. Student ed. Ellis Horwood series in inorganic chemistry. New York: Ellis Horwood, 1990. ISBN: 0134652460 (cit. on p. 23).

[99] Donald R. Olander, R. H. Jones, and W. J. Siekhaus. "Molecular Beam Sources Fabricated from Multichannel Arrays. IV. Speed Distribution in the Centerline Beam". In: *Journal of Applied Physics* 41.11 (1970), pp. 4388–4391. ISSN: 00218979. DOI: 10.1063/1.1658472 (cit. on p. 24).

[100] Harold J. Metcalf and Peter van der Straten. *Laser Cooling and Trapping*. New York, NY: Springer New York, 1999. ISBN: 978-0-387-98728-6. DOI: 10.1007/978-1-4612-1470-0 (cit. on p. 24).

[101] G. R. Hanes. "Multiple Tube Collimator for Gas Beams". In: *Journal of Applied Physics* 31.12 (1960), pp. 2171–2175. ISSN: 00218979. DOI: 10.1063/1.1735519 (cit. on p. 25).

[102] H. C. W. Beijerinck and N. F. Verster. "Velocity distribution and angular distribution of molecular beams from multichannel arrays". In: *Journal of Applied Physics* 46.5 (1975), pp. 2083–2091. ISSN: 00218979. DOI: 10.1063/1.321845 (cit. on pp. 25, 26).

[103] Martin Knudsen. "Die Gesetze der Molekularströmung und der inneren Reibungsströmung der Gase durch Röhren". In: *Annalen der Physik* 333.1 (1909), pp. 75–130. ISSN: 00033804. DOI: 10.1002/andp.19093330106 (cit. on p. 25).

[104] Martin Knudsen. "Die Molekularströmung der Gase durch Öffnungen und die Effusion". In: *Annalen der Physik* 333.5 (1909), pp. 999–1016. ISSN: 00033804. DOI: 10.1002/andp.19093330505 (cit. on p. 25).

[105] P. Clausing. "Erratum: The Flow of Highly Rarefied Gases through Tubes of Arbitrary Length". In: *Journal of Vacuum Science and Technology* 8.6 (1971), p. 756. ISSN: 0022-5355. DOI: 10.1116/1.1315392 (cit. on p. 26).

[106] S. Adamson, C. O'Carroll, and J. F. McGilp. "The angular distribution of thermal molecular beams formed by single capillaries in the molecular flow regime". In: *Vacuum* 38.6 (1988), pp. 463–467. DOI: 10.1016/0042-207X(88)90589-1 (cit. on p. 26).

[107] V. V. Levdansky, J. Smolik, and P. Moravec. "Effect of surface diffusion on transfer processes in heterogeneous systems". In: *International Journal of Heat and Mass Transfer* 51.9-10 (2008), pp. 2471–2481. ISSN: 00179310. DOI: 10.1016/j.ijheatmasstransfer.2007.08.009 (cit. on p. 26).

[108] Nishanth Dongari, Ashutosh Sharma, and Franz Durst. "Pressure-driven diffusive gas flows in micro-channels: From the Knudsen to the continuum regimes". In: *Microfluidics and Nanofluidics* 6.5 (2009), pp. 679–692. ISSN: 1613-4982. DOI: 10.1007/s10404-008-0344-y (cit. on p. 26).

[109] J. Tabet et al. “Absolute molecular flux and angular distribution measurements to characterize DNA/RNA vapor jets”. In: *Nuclear Instruments and Methods in Physics Research Section B: Beam Interactions with Materials and Atoms* 268.15 (2010), pp. 2458–2466. DOI: 10.1016/j.nimb.2010.05.005 (cit. on p. 26).

[110] Jeffrey M. Guevremont, Stanley Sheldon, and Francisco Zaera. “Design and characterization of collimated effusive gas beam sources: Effect of source dimensions and backing pressure on total flow and beam profile”. In: *Review of Scientific Instruments* 71.10 (2000), p. 3869. ISSN: 0034-6748. DOI: 10.1063/1.1311939 (cit. on p. 26).

[111] C. A. Stan and Wolfgang Ketterle. “Multiple species atom source for laser-cooling experiments”. In: *Review of Scientific Instruments* 76.6 (2005), p. 063113. ISSN: 1089-7623. DOI: 10.1063/1.1935433 (cit. on p. 26).

[112] Marco Schioppo et al. “A compact and efficient strontium oven for laser-cooling experiments”. In: *Review of Scientific Instruments* 83.10 (2012), p. 103101. ISSN: 0034-6748. DOI: 10.1063/1.4756936 (cit. on pp. 26, 28, 48).

[113] M. Misakian. “Equations for the Magnetic Field Produced by One or More Rectangular Loops of Wire in the Same Plane”. In: *Journal of research of the National Institute of Standards and Technology* 105.4 (2000), pp. 557–564. DOI: 10.6028/jres.105.045 (cit. on p. 31).

[114] D. S. Barker et al. “Single-Beam Zeeman Slower and Magneto-Optical Trap Using a Nanofabricated Grating”. In: *Physical Review Applied* 11.6 (2019). ISSN: 2331-7019. DOI: 10.1103/PhysRevApplied.11.064023 (cit. on pp. 31, 34).

[115] Yannick Bidel. “Piégeage et refroidissement laser du strontium, Etude de l’effet des interférences en diffusion multiple”. Dissertation. Nizza: Université de Nice, 2002 (cit. on p. 35).

[116] C. J. H. Pagett et al. “Injection locking of a low cost high power laser diode at 461 nm”. In: *The Review of scientific instruments* 87.5 (2016), p. 053105. ISSN: 1089-7623. DOI: 10.1063/1.4947462 (cit. on p. 36).

[117] Xavier Baillard. “Horloge à réseau optique à atomes de Strontium”. Dissertation. Université Pierre et Marie Curie - Paris VI, 2008. URL: https://tel.archives-ouvertes.fr/tel-00267252/document (cit. on p. 36).

[118] Matthew A. Norcia and James K. Thompson. “Simple laser stabilization to the strontium 88Sr transition at 707 nm”. In: *Review of Scientific Instruments* 87.2 (2016), p. 023110. ISSN: 0034-6748. DOI: 10.1063/1.4942434 (cit. on p. 37).

[119] D. G. Matei et al. "1.5um Lasers with Sub-10 mHz Linewidth". In: *Physical review letters* 118.26 (2017), p. 263202. ISSN: 1079-7114. DOI: 10.1103/PhysRevLett.118.263202 (cit. on p. 37).

[120] W. Zhang et al. "Reduction of residual amplitude modulation to 1×10^{-6} for frequency modulation and laser stabilization". In: *Optics letters* 39.7 (2014), pp. 1980–1983. ISSN: 0146-9592. DOI: 10.1364/OL.39.001980 (cit. on pp. 38, 43, 44).

[121] Matthew A. Norcia et al. "Narrow-line laser cooling by adiabatic transfer". In: *New Journal of Physics* 20.2 (2018), p. 023021. ISSN: 1367-2630. DOI: 10.1088/1367-2630/aaa950 (cit. on p. 38).

[122] Rodolphe Le Targat, J.-J. Zondy, and Pierre Lemonde. "75%-Efficiency blue generation from an intracavity PPKTP frequency doubler". In: *Optics Communications* 247.4-6 (2005), pp. 471–481. ISSN: 00304018. DOI: 10.1016/j.optcom.2004.11.081 (cit. on p. 39).

[123] R. W. P. Drever et al. "Laser phase and frequency stabilization using an optical resonator". In: *Applied Physics B Photophysics and Laser Chemistry* 31.2 (1983), pp. 97–105. ISSN: 0721-7269. DOI: 10.1007/BF00702605 (cit. on p. 40).

[124] Eric D. Black. "An introduction to Pound–Drever–Hall laser frequency stabilization". In: *American Journal of Physics* 69.1 (2001), p. 79. ISSN: 0002-9505. DOI: 10.1119/1.1286663 (cit. on p. 40).

[125] Holger Müller. *Moderne optische Tests der Relativitätstheorie: Modern optical tests of relativity: Zugl.: Berlin, Humboldt-Univ., Diss., 2004*. Vol. 73. Schriftenreihe naturwissenschaftliche Forschungsergebnisse. Hamburg: Kovač, 2004. ISBN: 3830014945 (cit. on pp. 41, 43, 44).

[126] D. S. Elliott, Rajarshi Roy, and S. J. Smith. "Extracavity laser band-shape and bandwidth modification". In: *Physical Review A* 26.1 (1982), pp. 12–18. ISSN: 1050-2947. DOI: 10.1103/PhysRevA.26.12 (cit. on p. 42).

[127] Gianni Di Domenico, Stéphane Schilt, and Pierre Thomann. "Simple approach to the relation between laser frequency noise and laser line shape". In: *Applied optics* 49.25 (2010), pp. 4801–4807. ISSN: 0003-6935. DOI: 10.1364/AO.49.004801 (cit. on p. 42).

[128] Edward A. Whittaker, Manfred Gehrtz, and Gary C. Bjorklund. "Residual amplitude modulation in laser electro-optic phase modulation". In: *Journal of the Optical Society of America B* 2.8 (1985), p. 1320. ISSN: 0740-3224. DOI: 10.1364/JOSAB.2.001320 (cit. on p. 43).

[129] N. C. Wong and J. L. Hall. "Servo control of amplitude modulation in frequency-modulation spectroscopy: Demonstration of shot-noise-limited detection". In: *Journal of the Optical Society of America B* 2.9 (1985), p. 1527. ISSN: 0740-3224. DOI: 10.1364/JOSAB.2.001527 (cit. on p. 43).

[130] F. Du Burck and O. Lopez. "Correction of the distortion in frequency modulation spectroscopy". In: *Measurement Science and Technology* 15.7 (2004), pp. 1327–1336. ISSN: 0957-0233. DOI: 10.1088/0957-0233/15/7/015 (cit. on p. 43).

[131] C. Ishibashi, Jun Ye, and J. L. Hall. "Analysis/reduction of residual amplitude modulation in phase/frequency modulation by an EOM". In: *Technical digest*. Trends in optics and photonics series. Washington, D.C: Optical Society of America, 2002, pp. 91–92. ISBN: 1-55752-707-5. DOI: 10.1109/QELS.2002.1031144 (cit. on p. 44).

[132] Koji Arai. "Robust extraction of control signals for power-recycled interferometric gravitational-wavedetectors". Dissertation. Tokyo: University of Tokyo, 2001 (cit. on p. 44).

[133] Kyle W. Martin. "Compact Optical Frequency Standards for FutureApplications Beyond the Laboratory". Dissertation. Albuquerque: University of New Mexico, 2019 (cit. on p. 47).

[134] C. K. N. Patel. "Continuous-Wave Laser Action on Vibrational-Rotational Transitions of C O2". In: *Physical Review* 136.5A (1964), A1187–A1193. ISSN: 0031-899X. DOI: 10.1103/PhysRev.136.A1187 (cit. on p. 51).

[135] T. Takekoshi, B. M. Patterson, and R. J. Knize. "Observation of Optically Trapped Cold Cesium Molecules". In: *Physical Review Letters* 81.23 (1998), pp. 5105–5108. ISSN: 0031-9007. DOI: 10.1103/PhysRevLett.81.5105 (cit. on p. 51).

[136] Konstantin Ott et al. "Millimeter-long fiber Fabry-Perot cavities". In: *Optics express* 24.9 (2016), pp. 9839–9853. ISSN: 1094-4087. DOI: 10.1364/OE.24.009839 (cit. on pp. 51, 63, 82, 96).

[137] Steven T. Yang et al. "Comparing the use of mid-infrared versus far-infrared lasers for mitigating damage growth on fused silica". In: *Applied Optics* 49.14 (2010), p. 2606. ISSN: 0003-6935. DOI: 10.1364/AO.49.002606 (cit. on p. 52).

[138] James E. Shelby. "Density of vitreous silica". In: *Journal of Non-Crystalline Solids* 349 (2004), pp. 331–336. ISSN: 00223093. DOI: 10.1016/j.jnoncrysol.2004.08.206 (cit. on p. 53).

[139] U. Haken et al. “Refractive index of silica glass: Influence of fictive temperature”. In: *Journal of Non-Crystalline Solids* 265.1-2 (2000), pp. 9–18. ISSN: 00223093. DOI: 10.1016/S0022-3093(99)00697-3 (cit. on p. 53).

[140] David B. Fraser. “Factors Influencing the Acoustic Properties of Vitreous Silica”. In: *Journal of Applied Physics* 39.13 (1968), pp. 5868–5878. ISSN: 00218979. DOI: 10.1063/1.1656080 (cit. on p. 53).

[141] T. Doualle et al. “Thermo-mechanical simulations of CO 2 laser–fused silica interactions”. In: *Journal of Applied Physics* 119.11 (2016), p. 113106. ISSN: 0021-8979. DOI: 10.1063/1.4944435 (cit. on pp. 54, 65).

[142] Philip R. Dolan et al. “Femtoliter tunable optical cavity arrays”. In: *Optics letters* 35.21 (2010), pp. 3556–3558. ISSN: 0146-9592. DOI: 10.1364/OL.35.003556 (cit. on p. 54).

[143] Roland Albrecht et al. “Narrow-band single photon emission at room temperature based on a single nitrogen-vacancy center coupled to an all-fiber-cavity”. In: *Applied Physics Letters* 105.7 (2014), p. 073113. ISSN: 00036951. DOI: 10.1063/1.4893612 (cit. on p. 54).

[144] David Hunger et al. “Laser micro-fabrication of concave, low-roughness features in silica”. In: *AIP Advances* 2.1 (2012), p. 012119. ISSN: 21583226. DOI: 10.1063/1.3679721 (cit. on pp. 54, 96).

[145] Manuel Uphoff et al. “Frequency splitting of polarization eigenmodes in microscopic Fabry–Perot cavities”. In: *New Journal of Physics* 17.1 (2015), p. 013053. ISSN: 1367-2630. DOI: 10.1088/1367-2630/17/1/013053 (cit. on p. 54).

[146] David Hunger. “A Bose-Einstein condensate coupled to a micromechanical oscillator”. Dissertation. München: Ludwig-Maximilian-Universität, 2010 (cit. on pp. 54, 85).

[147] Sébastien Garcia et al. “Dual-wavelength fiber Fabry-Perot cavities with engineered birefringence”. In: *Optics express* 26.17 (2018), pp. 22249–22263. ISSN: 1094-4087. DOI: 10.1364/OE.26.022249 (cit. on p. 55).

[148] Sébastien Garcia. “Interfaces fibrées entre atomes uniques et photons uniques”. Dissertation. Paris: École Normale Supérieure de Paris, 2015 (cit. on pp. 55, 56, 66, 67).

[149] Konstantin Ott. “Towards a squeezing-enhanced atomic clock on a chip”. Dissertation. Paris: Université Pierre et Marie Curie - Paris VI, 2016 (cit. on pp. 55, 57, 85, 121).

[150] P. A. Temple, W. H. Lowdermilk, and D. Milam. "Carbon dioxide laser polishing of fused silica surfaces for increased laser-damage resistance at 1064 nm". In: *Applied optics* 21.18 (1982), pp. 3249–3255. ISSN: 0003-6935. DOI: 10.1364/AO.21.003249 (cit. on p. 59).

[151] Christian Weingarten et al. "Laser polishing and laser shape correction of optical glass". In: *Journal of Laser Applications* 29.1 (2017), p. 011702. ISSN: 1042-346X. DOI: 10.2351/1.4974905 (cit. on pp. 59, 62).

[152] Krzysztof M. Nowak, Howard J. Baker, and Denis R. Hall. "Efficient laser polishing of silica micro-optic components". In: *Applied optics* 45.1 (2006), pp. 162–171. ISSN: 0003-6935. DOI: 10.1364/AO.45.000162 (cit. on p. 59).

[153] Philippe Cormont et al. "Relevance of Carbon Dioxide Laser to Remove Scratches on Large Fused Silica Polished Optics". In: *Advanced Engineering Materials* 17.3 (2015), pp. 253–259. ISSN: 14381656. DOI: 10.1002/adem.201400383 (cit. on p. 59).

[154] James Sullivan, Jian Zhao, and Ted D. Bennett. "Measurement of thermally induced changes in the refractive index of glass caused by laser processing". In: *Applied optics* 44.33 (2005), pp. 7173–7180. ISSN: 0003-6935. DOI: 10.1364/ao.44.007173 (cit. on p. 64).

[155] Théo Claude. "Émission dans les bandes télécoms de nanotubes de carbone uniques couplés à une micro-cavité fibrée". Dissertation. Paris: Sorbonne Université, 2019 (cit. on p. 64).

[156] Charles R. Lilley and John E. Sader. "Velocity profile in the Knudsen layer according to the Boltzmann equation". In: *Proceedings of the Royal Society A: Mathematical, Physical and Engineering Sciences* 464.2096 (2008), pp. 2015–2035. ISSN: 1364-5021. DOI: 10.1098/rspa.2008.0071 (cit. on p. 64).

[157] Lucile Robin et al. "Infrared thermometry and interferential microscopy for analysis of crater formation at the surface of fused silica under CO2 laser irradiation". In: *Journal of Applied Physics* 111.6 (2012), p. 063106. ISSN: 0021-8979. DOI: 10.1063/1.3695375 (cit. on p. 64).

[158] Christopher M. Bishop. *Pattern recognition and machine learning*. Corrected at 8th printing 2009. Information science and statistics. New York, NY: Springer, 2009. ISBN: 9781493938438 (cit. on p. 70).

[159] Prajit Ramachandran, Barret Zoph, and Quoc Le V. *Searching for Activation Functions*. URL: http://arxiv.org/pdf/1710.05941v2 (cit. on p. 72).

[160] Manzil Zaheer et al. "Adaptive Methods for Nonconvex Optimization". In: *Advances in Neural Information Processing Systems 31*. Ed. by S. Bengio et al. Curran Associates, Inc, 2018, pp. 9793–9803. URL: http://papers.nips.cc/paper/8186-adaptive-methods-for-nonconvex-optimization.pdf (cit. on p. 72).

[161] Yal Gal. "Uncertainty in Deep Learning". Dissertation. University of Cambridge, 2016. URL: http://mlg.eng.cam.ac.uk/yarin/thesis/thesis.pdf (cit. on p. 75).

[162] W. Emkey and C. Jack. "Analysis and evaluation of graded-index fiber lenses". In: *Journal of Lightwave Technology* 5.9 (1987), pp. 1156–1164. ISSN: 0733-8724. DOI: 10.1109/JLT.1987.1075651 (cit. on pp. 75, 76).

[163] William A. Reed, Man F. Yan, and Mark J. Schnitzer. "Gradient-index fiber-optic microprobes for minimally invasive in vivo low-coherence interferometry". In: *Optics Letters* 27.20 (2002), p. 1794. ISSN: 0146-9592. DOI: 10.1364/OL.27.001794 (cit. on p. 75).

[164] Michael Zickar et al. "MEMS compatible micro-GRIN lenses for fiber to chip coupling of light". In: *Optics Express* 14.10 (2006), p. 4237. ISSN: 1094-4087. DOI: 10.1364/OE.14.004237 (cit. on p. 75).

[165] Robert P. J. Barretto, Bernhard Messerschmidt, and Mark J. Schnitzer. "In vivo fluorescence imaging with high-resolution microlenses". In: *Nature methods* 6.7 (2009), pp. 511–512. ISSN: 1548-7091. DOI: 10.1038/nmeth.1339 (cit. on p. 75).

[166] Jun Ki Kim et al. "Fabrication and operation of GRIN probes for in vivo fluorescence cellular imaging of internal organs in small animals". In: *Nature protocols* 7.8 (2012), pp. 1456–1469. DOI: 10.1038/nprot.2012.078 (cit. on p. 75).

[167] Orazio Svelto and D. C. Hanna. *Principles of Lasers*. 5th ed. New York: Springer, 2010. ISBN: 1441913025 (cit. on pp. 78, 86, 91, 118).

[168] W. B. Joyce and B. C. DeLoach. "Alignment of Gaussian beams". In: *Applied Optics* 23.23 (1984), p. 4187. ISSN: 0003-6935. DOI: 10.1364/AO.23.004187 (cit. on p. 80).

[169] Gurpreet Kaur Gulati et al. "Fiber cavities with integrated mode matching optics". In: *Scientific Reports* 7.1 (2017), p. 5556. ISSN: 2045-2322. DOI: 10.1038/s41598-017-05729-8 (cit. on pp. 82, 85).

[170] Simon Bernon et al. "Heterodyne non-demolition measurements on cold atomic samples: Towards the preparation of non-classical states for atom interferometry". In: *New Journal of Physics* 13.6 (2011), p. 065021. ISSN: 1367-2630. DOI: 10.1088/1367-2630/13/6/065021 (cit. on p. 86).

[171] Robert J. Lewis-Swan et al. *A cavity-QED protocol for precise field sensing in the optical domain*. 2019. URL: http://arxiv.org/pdf/1909.07524v1 (cit. on p. 86).

[172] Anthony E. Siegman. *Lasers*. Mill Valley, Calif.: University Science Books, 1986. ISBN: 0935702113 (cit. on pp. 87, 88).

[173] M. Möller et al. "Fabry-Pérot and ring cavity configurations and transverse optical patterns". In: *Journal of Modern Optics* 45.9 (1998), pp. 1913–1926. ISSN: 0950-0340. DOI: 10.1080/09500349808231710 (cit. on pp. 89, 92).

[174] H. Kogelnik et al. "Astigmatically compensated cavities for CW dye lasers". In: *IEEE Journal of Quantum Electronics* 8.3 (1972), pp. 373–379. ISSN: 0018-9197. DOI: 10.1109/JQE.1972.1076964 (cit. on p. 89).

[175] Fred Raab and Stan Whitcomb. "Estimation of Special Optical Properties of a Triangular Ring Cavity". In: LIGO-T920004-00-R (1992). URL: https://dcc.ligo.org/LIGO-T920004/public (cit. on pp. 91, 92, 97).

[176] Jie Yuan et al. "Nonplanar ring resonator modes: Generalized Gaussian beams". In: *Applied optics* 46.15 (2007), pp. 2980–2989. ISSN: 0003-6935. DOI: 10.1364/ao.46.002980 (cit. on p. 91).

[177] Dandan Wen, Dong Li, and Jianlin Zhao. "Analysis on the polarization property of the eigenmodes in a nonplanar ring resonator". In: *Applied optics* 50.18 (2011), pp. 3057–3063. ISSN: 0003-6935. DOI: 10.1364/AO.50.003057 (cit. on p. 91).

[178] Dong Li, Chao Bi, and Jianlin Zhao. "Characterization of the eigenmode frequency spectrum influenced by the polarization states and light field distribution in a nonplanar ring resonator". In: *Applied optics* 55.12 (2016), pp. 3287–3293. ISSN: 0003-6935. DOI: 10.1364/AO.55.003287 (cit. on p. 91).

[179] Philip Baumeister. *Optical coating technology*. Vol. PM137. SPIE Press monograph. Bellingham, Wash. (1000 20th St. Bellingham WA 98225-6705 USA): SPIE, 2004. ISBN: 9780819453136. URL: http://dx.doi.org/10.1117/3.548071 (cit. on p. 92).

[180] H. Davies. "The reflection of electromagnetic waves from a rough surface". In: *Proceedings of the IEE - Part III: Radio and Communication Engineering* 101.70 (1954), p. 118. ISSN: 2054-0442. DOI: 10.1049/pi-3.1954.0030 (cit. on p. 94).

[181] H. E. Bennett and J. O. Porteus. "Relation Between Surface Roughness and Specular Reflectance at Normal Incidence". In: *Journal of the Optical Society of America* 51.2 (1961), p. 123. ISSN: 0030-3941. DOI: 10.1364/JOSA.51.000123 (cit. on p. 94).

[182] James E. Harvey. "Total integrated scatter from surfaces with arbitrary roughness, correlation widths, and incident angles". In: *Optical Engineering* 51.1 (2012), p. 013402. ISSN: 1560-2303. DOI: 10.1117/1.OE.51.1.013402 (cit. on pp. 94, 95).

[183] Nicolas Straniero et al. "Realistic loss estimation due to the mirror surfaces in a 10 meters-long high finesse Fabry-Perot filter-cavity". In: *Optics express* 23.16 (2015), pp. 21455–21476. ISSN: 1094-4087. DOI: 10.1364/OE.23.021455 (cit. on pp. 94, 95).

[184] J. M. Elson, J. P. Rahn, and J. M. Bennett. "Relationship of the total integrated scattering from multilayer-coated optics to angle of incidence, polarization, correlation length, and roughness cross-correlation properties". In: *Applied optics* 22.20 (1983), p. 3207. ISSN: 0003-6935. DOI: 10.1364/ao.22.003207 (cit. on p. 95).

[185] Jérôme Degallaix. "OSCAR a Matlab based optical FFT code". In: *Journal of Physics: Conference Series* 228 (2010), p. 012021. ISSN: 1742-6588. DOI: 10.1088/1742-6596/228/1/012021 (cit. on p. 96).

[186] P. Hello and C. N. Man. "Design of a low-loss off-axis beam expander". In: *Applied optics* 35.15 (1996), pp. 2534–2536. ISSN: 0003-6935. DOI: 10.1364/AO.35.002534 (cit. on p. 96).

[187] G. Krenz et al. "Controlling mode locking in optical ring cavities". In: *Applied Physics B* 87.4 (2007), pp. 643–647. DOI: 10.1007/s00340-007-2632-8 (cit. on pp. 96, 98).

[188] Dietmar Kruse. "Selbstorganisation und Laseremission in kalten atomaren Ensembles". Dissertation. Tübingen: Eberhard-Karls-Universität zu Tübingen, 2005. URL: https://d-nb.info/97567837X/34 (cit. on p. 97).

[189] Dorian Gangloff et al. "Preventing and reversing vacuum-induced optical losses in high-finesse tantalum (V) oxide mirror coatings". In: *Optics express* 23.14 (2015), pp. 18014–18028. ISSN: 1094-4087. DOI: 10.1364/OE.23.018014 (cit. on p. 100).

[190] J. Gallego et al. "Strong Purcell Effect on a Neutral Atom Trapped in an Open Fiber Cavity". In: *Physical review letters* 121.17 (2018), p. 173603. ISSN: 1079-7114. DOI: 10.1103/PhysRevLett.121.173603 (cit. on p. 100).

[191] Thomas Middelmann et al. "High Accuracy Correction of Blackbody Radiation Shift in an Optical Lattice Clock". In: *Physical Review Letters* 109.26 (2012). ISSN: 0031-9007. DOI: 10.1103/PhysRevLett.109.263004 (cit. on p. 103).

[192] Jérôme Lodewyck et al. “Observation and cancellation of a perturbing dc stark shift in strontium optical lattice clocks”. In: *IEEE transactions on ultrasonics, ferroelectrics, and frequency control* 59.3 (2012), pp. 411–415. DOI: 10.1109/TUFFC.2012.2209 (cit. on p. 103).

[193] Dmitry I. Yakubovsky et al. “Optical constants and structural properties of thin gold films”. In: *Optics express* 25.21 (2017), pp. 25574–25587. ISSN: 1094-4087. DOI: 10.1364/OE.25.025574 (cit. on p. 108).

[194] Wineland et al. “Spin squeezing and reduced quantum noise in spectroscopy”. In: *Physical Review A* 46.11 (1992), R6797–R6800. ISSN: 1050-2947. DOI: 10.1103/physreva.46.r6797 (cit. on p. 113).

[195] Onur Hosten et al. “Measurement noise 100 times lower than the quantum-projection limit using entangled atoms”. In: *Nature* 529.7587 (2016), pp. 505–508. ISSN: 0028-0836. DOI: 10.1038/nature16176 (cit. on p. 114).

[196] A. S. Parkins, E. Solano, and J. I. Cirac. “Unconditional two-mode squeezing of separated atomic ensembles”. In: *Physical Review Letters* 96.5 (2006), p. 053602. ISSN: 0031-9007. DOI: 10.1103/PhysRevLett.96.053602 (cit. on p. 114).

[197] Wenlan Chen et al. “Carving Complex Many-Atom Entangled States by Single-Photon Detection”. In: *Physical review letters* 115.25 (2015), p. 250502. ISSN: 1079-7114. DOI: 10.1103/PhysRevLett.115.250502 (cit. on p. 114).

[198] Stephan Welte et al. “Cavity Carving of Atomic Bell States”. In: *Physical review letters* 118.21 (2017), p. 210503. ISSN: 1079-7114. DOI: 10.1103/PhysRevLett.118.210503 (cit. on p. 114).

[199] Paul F. Goldsmith. *Quasioptical systems: Gaussian beam quasioptical propagation and applications*. IEEE press/Chapman & Hall Publishers series on microwave technology and RF. Piscataway, New Jersey: IEEE Press, 1998. ISBN: 9780470546291 (cit. on p. 117).